2008-06-04

Material Flow Behavior in Friction Stir Welding

Brian C. Liechty
Brigham Young University - Provo

MATERIAL FLOW BEHAVIOR IN FRICTION STIR WELDING

by

Brian C. Liechty

A dissertation submitted to the faculty of

Brigham Young University

in partial fulfillment of the requirements for the degree of

Doctor of Philosophy

Department of Mechanical Engineering

Brigham Young University

August 2008

BRIGHAM YOUNG UNIVERSITY

GRADUATE COMMITTEE APPROVAL

of a dissertation submitted by

Brian C. Liechty

This dissertation has been read by each member of the following graduate committee and by majority vote has been found to be satisfactory.

Date	Brent W. Webb, Chair
Date	Carl D. Sorensen
Date	Tracy W. Nelson
Date	Brent L. Adams
Date	R. Daniel Maynes

BRIGHAM YOUNG UNIVERSITY

As chair of the candidate's graduate committee, I have read the dissertation of Brian C. Liechty in its final form and have found that (1) its format, citations, and bibliographical style are consistent and acceptable and fulfill university and department style requirements; (2) its illustrative materials including figures, tables, and charts are in place; and (3) the final manuscript is satisfactory to the graduate committee and is ready for submission to the university library.

Date

Brent W. Webb
Chair, Graduate Committee

Accepted for the Department

Matthew R. Jones
Graduate Coordinator

Accepted for the College

Alan R. Parkinson
Dean, Ira A. Fulton College of Engineering and Technology

ABSTRACT

MATERIAL FLOW BEHAVIOR IN FRICTION STIR WELDING

Brian C. Liechty

Department of Mechanical Engineering

Doctor of Philosophy

Material flow in friction stir welding is largely uncharacterized due to the difficulty in material flow measurement and visualization in metals. This study investigates plasticine for use as an analog for modeling material flow in friction stir welding (FSW) of metals. Qualitative comparisons between welded plasticine and metal sections exhibit many similarities. The transient temperature response of the plasticine also shows the same qualitative behavior as welds conducted in metal. To quantify its similarity to metal, the plasticine is further analyzed through compression tests to characterize its strain, strain-rate, and temperature sensitivities. A detailed analysis is presented which defines the criteria for rigorous mechanical and thermal similarity between metals and analog materials. The mechanical response of the plasticine is quantitatively similar to many aluminum and steel alloys. In addition to the mechanical properties of the plasticine, thermal properties are measured and thermal similarity is

investigated. Generally, complete thermal similarity cannot be achieved in FSW. However, given the similarities between other critical parameters, and observed qualitatively similarity, it is possible to satisfy similarity approximately, such that information can be obtained from the physical model and extrapolated to metals. Using plasticine, material flow behavior in FSW is investigated under various operating conditions. The physical model permits visualization and characterization of material flow around a suspended welding tool. Depending on operating conditions, several material flow regimes are observed, including simple extrusion with substantial tool/material slip, defect formation, a region of rotating material adjacent to the tool, and vertical deformation.

Material flow and frictional heating in FSW are also investigated using a three-dimensional numerical model. Two mechanical boundary conditions are investigated, including 1) a sticking constant velocity, and 2) a slipping variable shear stress model. The constant velocity model generally over-predicts the extent of material flow in the weld region. The variable shear model predicts simple extrusion of material around the tool, and substantial tool/material slip. Additionally, the variable shear model exhibits a region of diminishing shear stress, velocity, and pressure at the back advancing side of the pin, suggesting formation of an internal void. The limited deformation, low velocities, and indication of void formation agree well with flow visualization studies using plasticine under identical operating parameters.

ACKNOWLEDGMENTS

Above all, I have to thank my wife, Rebecca, who has and will continue to support me in all my work. I am also grateful for the dedication of my graduate advisor, Dr. Brent Webb, for his guidance and countless hours of involvement. The support and guidance from the remainder of my graduate committee is immensely appreciated. Finally, testing and research assistance from Katie Eckerson with the plasticine property measurements is also acknowledged.

Financial support for this work from the Office of Naval Research, contract No. N00014-05-1-0511, and Program Manager Dr. Julie Christodoulou.

TABLE OF CONTENTS

LIST OF TABLES

LIST OF FIGURES

1 Introduction

1.1 The Friction Stir Welding Process

Friction stir processing/welding (FSP/FSW) is a solid-state technique used for joining materials for general material processing (*i.e.*, surface machining). The technique is currently used to join materials from plastics to high-strength steels in industries including automotive, aircraft, and shipbuilding. FSW provides many benefits over other conventional joining methods. Since material is never melted during FSW, lower peak temperatures result and any pre-weld heat treatment of the alloy is less affected [1]. In addition, it is a safe, low-cost process that requires little operator training. Although the material is never heated to its melting point during FSW, the process is characterized by high temperatures and severe plastic deformation.

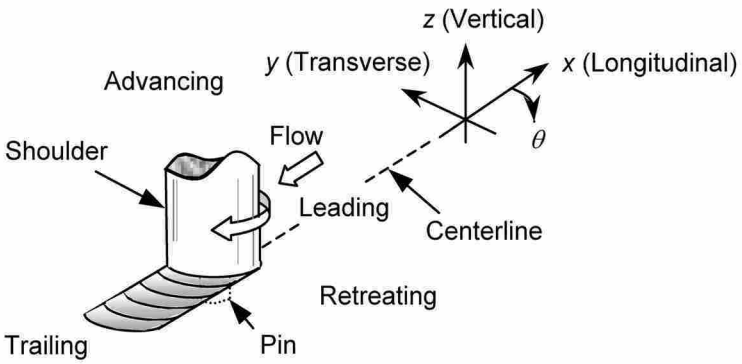

Figure 1-1: Friction Stir Welding Process.

The process is performed by traversing a rotating tool through a workpiece material along a desired path as shown schematically in Figure 1-1. Generally, the FSW tool consists of a cylindrical shoulder and a concentric pin, although off-axis pins have been used successfully [2]. The tool pin is forced into the workpiece, and acts to increase the penetration depth of the weld or processed zone. The shoulder is positioned at the surface of the workpiece, consolidating material that flows around the pin. At the retreating side of the tool, the direction of the tangential velocity of the rotating tool is opposite to the direction of the tool feed. At the advancing side, the tangential velocity of the tool is in the same direction as the tool feed.

1.2 Previous Studies

1.2.1 Material Flow Observations

An important research area of FSW is the flow of material around the tool. An understanding of the plastic deformation that occurs during the process is critical if an optimized tool shape and set of input conditions is to be determined. A significant effort has been made to experimentally visualize material flow in FSW. Early work revealed vortex-like swirl features in the welded zone [3, 4]. These studies placed different aluminum alloys and/or aluminum and copper plates on either side (advancing and retreating) of the centerline. After joining of the two dissimilar plates, sections were cut and chemically etched to show deformation features apparent from the contrasting materials. Often, a concentric ring pattern (so-called “onion rings”) was observed in cross-sections of the weld nugget. However, it was concluded that material flow features from the welded plates varied due to tool rotational rate, feed rate, and tilt angle. At low

rotational speeds, mixing of the two weldpieces can be very minimal. As the rotational rate increases (traverse speed constant), mixing can become more uniform where the interface between markers and/or two weld pieces becomes blurred [5-7]. For example, Reynolds [6], and Seidel and Reynolds [7] have investigated material flow differences at varying weld pitch (tool advance distance per rotation) by inserting several contrasting aluminum markers at various depths on both the advancing and retreating sides of the weld. They discovered a rotational motion about the longitudinal axis caused by the trailing edge of the shoulder. Material directly under the trailing edge of the shoulder was displaced from the retreating side of the centerline to the advancing side. This displacement induces a vertical component of deformation where material is forced vertically downward at the advancing side and upward at the retreating side. At a relatively high weld pitch (feed distance per tool rotation), this rotating flow had a minimal effect and the interface between markers was obvious even after welding. However, as the weld pitch decreased, the flow pattern became more prominent and the interface between markers was blurred. Others have also observed this blending or mixing of material in the weld zone at higher rotational rates (and low to moderate feed rates) [5, 8]. It is unclear whether this effect is due to greater material softening resulting from the higher temperatures experienced at low weld pitch, or an effect resulting from pin threads.

Several studies have investigated material deformation as it flows around the tool by employing a stop-action technique where the rotational and forward motion of the tool is nearly instantaneously stopped [8-10]. Colligan [9] embedded small steel spheres along lines parallel to the direction of tool travel in an aluminum workpiece. Post-weld

x-ray imaging of the particles revealed detailed material flow around the tool. Generally, particles initially at the lower half of the weld were simply extruded around the pin and deposited at the retreating side of the centerline. In the upper part of the workpiece, however, material was lifted upward to fill the concave shoulder and rotated several times with the tool. This rotating material was generally deposited at the advancing side of the centerline. Guerra *et al.* [8] also observed a thin rotating region around the tool pin. By placing a thin vertical copper foil at the centerline, the study revealed that material inside this rotating region experiences a complex vertical flow path due to the pin threads. It was concluded that material was pulled down by the pin threads, flowed outward near the bottom of the pin, and upward at the outer edge of the rotating region. Material in the rotating region was intermittently deposited in the wake of the pin in arch-shaped layers.

This intermittent behavior raises important questions about the nature of the boundary condition and there is some debate as to whether material sticks or slips at the tool interface during FSW. There is evidence that in some cases, a slipping or sticking/slipping boundary condition prevails. Schmidt *et al.* [10] observed a cyclic deposition of copper marker material in aluminum welds, which is attributed to a sliding/sticking condition. To further complicate the boundary condition, sometimes a void may form at the back surface of the pin. If a void is present in the processed region, slipping must be occurring due to the extremely viscous nature of material flow during FSW. Creeping viscous flows around cylinders have been widely documented in the fluid mechanics community [11]. These flows are distinguishable by smooth streamlines around the upper and lower halves of the cylinder. These streamlines join perfectly at the back of the cylinder with no flow separation. Therefore, void formation (precipitated by

flow separation) behind the tool pin in FSW is likely a result of a slipping interface. Gerlich *et al.* [12, 13] and Frigaard *et al.* [14] have demonstrated that the sticking/slipping boundary condition is dependent on workpiece material. Additionally, Kim *et al*. [15] showed that tool downforce contributes greatly to the formation of voids and other defects.

Most of the experimental data on material flow and boundary conditions in FSW is largely qualitative. There is only very limited data available on strain-rate and velocity measurements in FSW. By analyzing final marker positions after welding, Schmidt *et al.* [10] have estimated the material velocity just outside the rotating region at 10 - 30% of the tool's rotational speed. Additionally, average strain-rate values in the deforming region have been determined using the Zener-Hollomon parameter, calculated from measured grain sizes in FSW sections [12-14]. Results from these studies indicate that the friction boundary condition is dependent on the workpiece material and tool rotational rate. With some alloys (Al 5754 and Al 6061), strain-rates were found to be consistent with a no-slip condition at the tool surface, and increased with tool rotational speed [13]. Strain-rates in other alloys (Al 2024 and Al 7075), however, were observed to decrease with rotational speed, and are several orders of magnitude lower than expected for no-slip conditions [13].

It is somewhat difficult to understand the mechanism behind material-dependent tool slip. However, under high normal stress, the frictional condition is often best modeled as a function of the material's flow stress [16], and thus, a link may be made between the contact interface and the specific material. The work by Gerlich *et al.* [12], Gerlich *et al*. [13], and Frigaard *et al*. [14] provide what appears to be the first

quantitative experimental data designed to directly report on strain-rates and slip in FSW. However, aside from the limited data presented by Frigaard *et al.* [14], these results apply to friction stir spot welding, and it is unclear how well the data can be extrapolated to FSW with a translating tool.

1.2.2 Analog Models

Material flow visualization and measurement using metals is complicated by several factors. In many studies, individual markers are inserted into the workpiece [7-10]. This marker material is distinctly different from the parent material. During FSW, the inserted marker material may slip relative to the parent material, resulting in an uncharacteristic flow behavior. More importantly, material flow in FSW is influenced by thermo-mechanical material properties (*eg.*, flow stress). Consequently, flow features may be altered by the presence of markers with different physical properties than the surrounding material. This consequence has been observed in FSW studies of dissimilar systems [5, 17]. These studies note distinct differences in flow features from a uniform workpiece compared to butt welds of dissimilar metals. It is possible to observe material flow features in a homogenous workpiece, but detail is limited and chemical etching and polishing is required. In addition, it is difficult to distinguish flow features in a homogenous workpiece from strain and temperature effects.

Physical modeling of FSW using transparent polycarbonate materials has been attempted [18]. Polycarbonate offers potential for visualization of material flow during FSW. Some of the general flow characteristics in aluminum were observed during the polycarbonate weld. However, welding of the polycarbonate with a threaded tool could

not be achieved because the threads became clogged with the polymer. In addition, edge entry of the tool produced poor weld results. Further, it must be acknowledged that the thermomechanical properties of polycarbonate are inherently different from metals, and thus, its weld characteristics will depart fundamentally from that expected in FSW of metals.

If an appropriate modeling material is chosen through careful analysis, it can be used to predict many behaviors of the metal, such as the temperature, strain, and/or stress distributions [19]. In order to gain a firm understanding of flow processes during FSW and their causes, this study investigates plasticine for use as a physical analog. "Plasticine" is the original brand name of oil-based modeling clay. However, the name has since become synonymous with oil-based modeling clay and the two terms (clay and plasticine) are used here interchangeably. Although plasticine is an amorphous material, which will result in differences at the microstructural level, it may duplicate gross material flow of metals. Substantial research has been done to validate the use of plasticine to model material flow in metal forming processes, such as extrusion, rolling, and forging [20-23]. Three-dimensional extrusion processes have previously been analyzed with physical modeling and finite element analysis to validate the use of plasticine as an analog model for the behavior of both elastic-plastic materials [23] and elastic-viscoplastic materials [20]. The results of both the finite element analysis and the plasticine model were in agreement in each case.

Plasticine has not been previously used to model FSW, and offers several potential benefits: 1) clays of several different colors (all of identical properties) can be used as markers, 2) due to highly contrasting colors, flow features from welded sections

are immediately obvious (no etching is required), 3) macroscopically mixed regions in the weld zone can be analyzed simply by the color of the region to determine the extent of mixing (*i.e.*, to determine percent advancing/retreating material present in the weld nugget), 4) multiple colored layers and markers can be fused by compression of the layers, eliminating discontinuities (the ability to combine multiple contrasting layers of the plasticine to form a more homogenous workpiece allows for observation of material flow with minimal intrusion), and 5) ease of stop-action, where material flow can be nearly instantaneously suspended. To achieve stop-action in metals, the rotational motion of the tool must be rapidly suspended [8, 9] at great load to the processing machine. The rotational speed of the tool does not need to be suspended for successful stop-action with plasticine because measured transverse and longitudinal forces during FSW of plasticine are very small (10-20 N) and drop rapidly to zero once the forward motion of the tool is suspended. Thus, by suspending the forward motion of the tool and immediately extracting it (decoupling the shoulder/material interface), results in frictional forces around the pin that are not sufficient to cause further material motion, except for material inside the threads, which is extracted with the tool.

Additionally, the melting point of plasticine is very low compared to metals, which makes constitutive property measurements comparatively simple at temperatures typically observed in FSW. Currently, information on mechanical constitutive behavior of metals at high temperatures and strain-rates is an area of concern and current models may lack adequate description [24, 25]. In some instances the tool/material boundary condition may be dependent on these constitutive relations. For example, a Tresca friction condition is proportional to the flow stress (determined from constitutive

relations) of the material. Therefore, if such a boundary condition is to be used in a numerical model, then a model for the flow stress must be accurate.

1.2.3 Computational Models

Computer modeling is an important tool for the prediction and optimization of the FSW process. The most general FSW model would include both an elastic and plastic response, and feature full mechanical and thermal coupling. However, due to computational costs, several simplifications are made to reduce the complexity of the FSW problem. For example, Zhang and Zhang [26] imposed an experimentally determined temperature field in numerical simulations to decouple the thermomechanical problem. Additionally, the translational and rotational speeds were increased by a factor of 1000 to accelerate computation to steady-state conditions. Although predictions appear reasonable, no comparison is made between the model and experimental data. Chen *et al*. [27] included the thermomechanical coupling, but simplified the domain by employing symmetry along the weld line and neglected any deformation heating in the weld region. Although predicted temperature and residual stress values compared reasonably well with experiments, experimental and numerical data has shown that material flow in FSW is not symmetric about the weld line [9, 28]. Additionally, since the nature of the boundary condition is largely unknown, it is difficult to compare the magnitude of direct frictional heating at the tool compared to deformation heating, which others report as substantial and should not be neglected [29]. A more comprehensive model is presented by Schmidt *et al*. [29], which includes deformation heating and more general tool/material boundary conditions. The model by Schmidt *et al*. [29] shows very

good results, including comparisons between predicted and measured values of heat generation, shear layer size, and plunge force. Additionally, the model is capable of predicting void formation, which could serve to determine suitable welding parameters. However, even with only 20,000 elements and mass scaling, the elastic-viscoplastic solution required a 14-day solution time to reach steady-state conditions. Buffa *et al*. [28] also incorporated both tool and deformation heat sources but used a rigid-viscoplastic model (negligible elastic response). The approximation made in the rigid-viscoplastic model is generally acceptable in FSW since plastic strains can be very large compared to elastic strains. Both the initial plunge phase and translation were simulated. Predicted and experimental vertical welding forces were found to be nearly identical, and general qualitative temperature distributions were similar to experimental data.

Although the models presented above show encouraging results, they use either a Lagrangian or arbitrary Lagrangian-Eulerian formulation and require computationally expensive re-meshing for the transient approach. Traditionally, problems in solid mechanics are formulated using a Lagrangian approach. This vantage point is useful especially for visualization of final material deformation. However, the extreme deformation possible in FSW lends itself to an Eulerian reference frame. An Eulerian formulation permits a fixed mesh and modeling of the steady-state FSW translating phase. The primary disadvantages of an Eulerian model include lack of an elastic response and inability to directly predict void formation. Given the large plastic flow in FSW, however, the elastic response could be neglected without significant loss in accuracy if the material is insensitive to strain-hardening (*i.e.*, a rigid-viscoplastic material model) [30]. Generally, it is more difficult to impose material strain hardening

since the history of the material is not tracked directly. Rather, a separate hardening law must be implemented in the model, which must be integrated along a pathline as presented by Cho *et al*. [30] and Bastier *et al*. [31]. Additionally, He *et al.* [32] have recently developed a porosity evolution model to predict void growth during FSW using an Eulerian fluid mechanics type model.

Unlike their Lagrangian counterparts, Eulerian models have been developed using both a finite element [30-34] and a more traditional fluid mechanics-based control volume formulation [24, 35, 36]. Similar to the Lagrangian finite element models discussed previously, these models also show promising results, but have the advantage of relatively short computation times. For example, the finite element method used by Bastier *et al*. [31] in steady-state FSW flow shows workpiece temperature predictions that match well with experiments. The computational time for this model is on the order of 90 minutes. The solution of the thermomechanical problem was also integrated along particle pathlines to determine mechanical history and residual stresses. Strain and residual stress results compare well qualitatively with experimental data. By contrast, Nandan *et al*. [36] employed a control volume approach for discretization of the FSW domain. Generally, resulting temperature profiles compare well with experiments. Additionally, predicted torque values are in agreement with measured data.

Regardless of modeling approach, the large deformation plastic flow and coupled thermal behavior in FSW make numerical simulation difficult. For example, material in contact with the rotating tool may stick and/or slip against the tool. The detailed physics of this boundary condition are unknown, and researchers are left to make approximations. Most assume a constant material velocity at the tool equal to the tangential speed of the

tool [24, 34, 37], or at some fraction of the tool speed [36, 38]. For example, Heurtier *et al.* [38] estimated as much at 99% slip in AA2024, which was extrapolated from the size of the material zone that rotates with the shoulder in experiments. A Coulomb friction model using a constant value for the friction coefficient limited by the material flow stress has also been employed [26, 29]. Such a boundary condition is capable of predicting void formation and tool slip as part of the solution. However, in some cases the upper limiting shear stress at the tool/material boundary could be lower than the actual shear flow stress [16], and no transition between the sliding and sticking model is included. An applied surface traction, proportional to the tool/material velocity difference, has also been employed [32, 34]. This so-called viscoplastic model, however, predicts zero friction when a sticking condition exists (*i.e.*, it neglects static friction effects). The thermal boundary condition at the tool has also been modeled in many forms. Of course, if a no-slip condition is assumed then no frictional heating is generated by the tool surfaces, and all heat input stems from deformation heating. Nandan *et al.* [36] proposed an algebraic model for the slipping boundary condition based on an assumed friction coefficient, normal pressure, material yield stress, and operational conditions. Others model the heat generation using a simple convection model, assuming a tool temperature and heat transfer coefficient [32, 34].

1.3 Problem Statement

This study includes both experimental and numerical modeling of the FSW process. Thermomechanical behavior, including material flow processes, boundary conditions, and deformation heating during FSW are experimentally determined. This

component of the study incorporates the use of plasticine as an analog to model FSW of metals. The analog model is used to aid in exploration of a numerical model. The major objectives for this study are:

i. Identify the suitability of plasticine for study of material flow in FSW of metals.
ii. Explore analytically the similarity implications and identify similarity parameters.
iii. Use the plasticine in a detailed investigation of FSW under various operating conditions.
iv. Develop a numerical model, and use experimental plasticine data to validate the model.

The first objective of this work is to explore the use of plasticine as an analog for material flow in FSW, and to determine a suitable type of plasticine for physical modeling of FSW in metals. The analysis is carried out through both experimental (Chapter 2) and analytical analysis (Chapter 3). Once a modeling material is established it can then be used for material flow visualization and measurement (Chapters 4 and 5). Although development of a strict set of corresponding operational parameters between metal and plasticine FSW may be quite difficult, it is believed that the analog model can be refined to the point that it distinguishes between material flow trends based on input parameters. The intent of this study is to provide a more complete and clear picture of material flow *regimes* in FSW. It is recognized that material flow in FSW can vary between different metals, tooling, and operating conditions, and hence, studies with plasticine are designed to illustrate extreme cases. Differences in FSW flow features at both high and low tool rotational speeds, increasing tool down force (or tool plunge

depth), and a threaded versus a smooth tool pin are investigated. A systematic study under extreme conditions in each of these scenarios permits a "cause and effect" analysis of tool rotational rate, material behavior with and without flash generation, and the consequence of pin threads. Finally, a numerical model of the process exploring various sticking/slipping boundary conditions is presented and validated with the experimental findings (Chapter 6).

2 Plasticine Analog Model

Several types of plasticine of varying physical properties were friction stir processed to explore the feasibility of using plasticine to model FSW of metals. Results presented in this chapter are strictly qualitative, but provide sufficient resolution to access similarity in deformation and material flow patterns between the various plasticine materials and metals. A detailed similarity analysis presenting the necessary dimensionless numbers required for a rigorous similarity analysis are presented in the following chapter. Among the types of clay investigated for FSW were: non-sulphurated plasticine (NSP) of varying hardness, manufactured by Chavant; Roma Plastilina, produced by Sculpture House; and a relatively soft clay manufactured by Van-Aken International. All of the clays above are oil-based and are available from various distributors.

2.1 Workpiece Setup and FSW Operating Conditions

The plasticine was first flattened to a uniform thickness of approximately 2 cm using a hydraulic press. Partial penetration welds were performed in the plasticine using both a smooth and threaded (0.9 threads/mm) pin on a fully automated vertical milling machine linked to a personal computer for input control and data acquisition. The welding tools that were used have a pin diameter of 7.7 and 8.2 mm and a length of 7.3 and 6.5 mm for the smooth and threaded pins, respectively. The shoulder (25.4 mm

diameter) of both tools is concave and was tilted back approximately 2.5 degrees during welding to aid in material consolidation. Both of these tools are shown in Figure 2-1. Rotational and traverse speeds ranged from 250 to 1500 rpm and 0.2 to 2.0 mm/s, respectively. Sections were cut from the welded plasticine using a thin wire (0.3 mm diameter) to minimize smearing.

Figure 2-1: Smooth and threaded pin tools.

2.2 Preliminary Results

Non-sulphurated plasticine (NSP) manufactured by Chavant has a melting temperature of 85^{o}C and is readily available in various hardness's classified as soft, medium, and hard. Significant plastic flow during welding in the hard and medium NSP clays could not be achieved (for the weld operating parameters explored), and as a result, large defects were present in the weld. Typically, much of the material was expelled at the retreating side of the shoulder as flash, resulting in a large trench behind the tool. The hardness of the soft NSP material and Roma Plastilina were very similar (note that hardness was determined solely by tactile feel). These two materials produced welds without defects. However, sound welds could not be achieved at rotational speeds above 1000 rpm. Cross-sections from successful welds of the NSP soft and Roma Plastilina

clays are shown in Figure 2-2. In each case a contrasting color was placed on either side of the centerline. The deformed interface observed in the figure is nearly identical for both clay types. However, the extent of deformation is quite minimal and many metals show significant deformation and complex flow patterns [6-8]. Therefore, due to the limited operating range and material flow, these materials were deemed unsatisfactory for a general analog model.

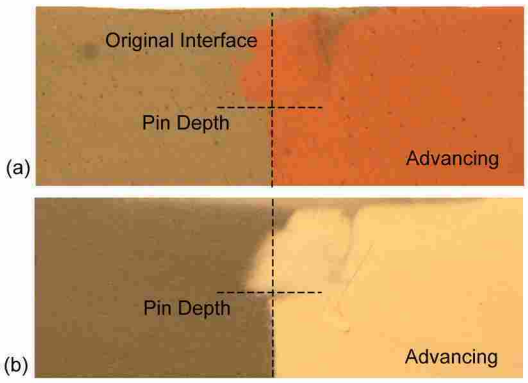

Figure 2-2: Welds conducted in (a) NSP Soft and (b) Roma Plastilina plasticine (450 rpm, 1.1 mm/s traverse speed).

A comparatively soft clay manufactured by Van Aken International (melting temperature of 65^{o}C) produced a defect-free weld for the entire range of operational parameters investigated. The Van Aken plasticine also exhibits material flow features that are similar to FSW of metals (as discussed below). Additionally, compared to other oil-based clays, the Van Aken material is available in a wider array of colors, which is useful for flow visualization. By using two or more clays of different colors in the weld, regions of mixing can be analyzed to determine, to some extent, the origin of the displaced material. Note that mixing is defined here as joining of the two different

workpieces and/or markers such that the resulting material is some intermediate composition. These desired characteristics of the Van Aken plasticine (*i.e.*, operational range, material flow similarity to metals, and color availability) distinguish it from all others investigated. Thus, the remainder of this work only addresses FSW of Van Aken plasticine and all other oil-based clays were abandoned.

2.3 Experimental Procedure for Van Aken FSW Analysis

To facilitate a quantitative analysis of the composition of mixed regions in the weld, color calibration curves consisting of red, green, and blue values (RGB) from digital photographs were obtained by mixing different colors of melted clay in known mass fractions. ImageJ (an open source code developed by the National Institutes of Health) was used for photo analysis to obtain RGB levels of the known color fraction clay mixtures. Note that RGB values are sensitive to lighting and specific camera settings (*i.e.*, shutter speed, aperture, white balance, *etc.*). To ensure consistency, all photographs were taken with the same Nikon D100 digital camera under two 250-Watt incandescent photoflood light bulbs with constant camera settings.

Welds were conducted with contrasting colors of the plasticine on either side of the centerline. To replicate flow features observed in previously published experiments using aluminum, some workpieces were constructed by strategically inserting contrasting color markers or orientating two cyan/magenta pieces in other than a butt weld configuration. The setup of these workpieces will be discussed as they are presented in the following section.

In addition to comparing flow features between welded clay samples and aluminum, heating effects were also examined. Thermal softening plays a significant role in the formation of weld features observed in metals. To replicate these features, a model (physical or numerical) should also exhibit significant softening in the weld region due to frictional/deformation heating. To determine if frictional/deformation heating plays any significant role in FSW of plasticine, two K-type thermocouples were inserted into the clay for some welds at approximately mid-pin depth, one along the centerline of the weld and another at the advancing side shoulder edge. Note that there is some difficulty in exactly locating the thermocouples in the plasticine because they can be shifted after insertion simply by the weight of the thermocouple wire in the soft clay. Additionally, the thermocouple at the centerline is pushed to the retreating side of the pin as the tool moves past it.

2.4 Van Aken FSW Results and Discussion

2.4.1 Color Calibration

Figure 2-3 shows red, green, and blue (RGB) levels measured in arbitrary units based on color intensity in the range 0 to 255 as a function of composition for two different clay color combinations. Ideally, the RGB response of a particular color of plasticine would be sufficiently sensitive to introduction of another color over the full range of mixture fraction. A linear curve, with a moderate gradient would show this desired characteristic. The white/blue plasticine color combination shown in Figure 2-3a exhibits large RGB value differences between the two colors. The green level as blue plasticine is added to white plasticine decreases nearly linearly. The red value scale

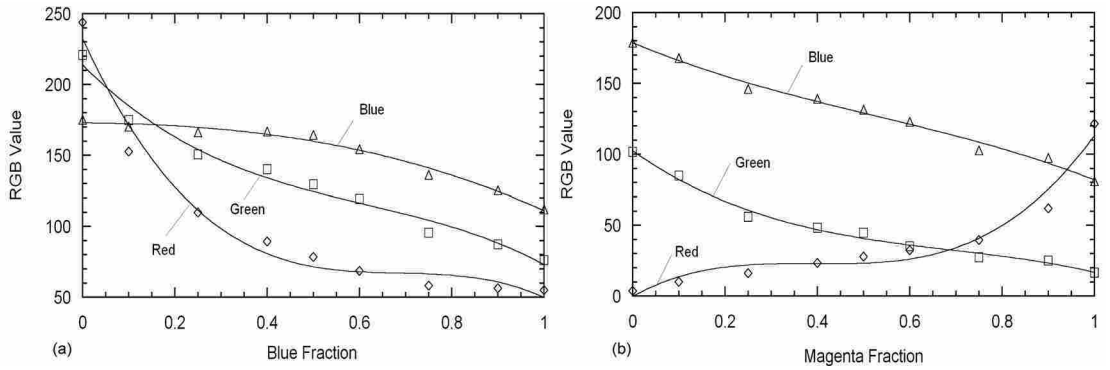

Figure 2-3: RGB calibration curves for mixed plasticine colors: (a) blue/white, and (b) cyan/magenta.

shows good sensitivity in the low blue/high white clay mixtures, while the opposite is true for blue values. The cyan/magenta plasticine combination in Figure 2-3b shows a near-linear decrease in blue level as magenta-colored clay is added to cyan. Red and green values, however, are less sensitive at particular mixture levels.

It should be noted that colors were found to differ slightly between each batch of parent plasticine. This introduces some uncertainty in the calibration curves. To correct for slight color variations, each point on the calibration curve is adjusted such that the RGB values at the endpoints of the curve match the specific clay used for a particular weld. Linear interpolation between points on the adjusted curve is then used to analyze areas of a weld that contain a mixture of both clay colors (macroscopically mixed regions).

The calibration curves make it possible to quantify the concentration of marker material at specific regions in the weld. By measuring RGB values at a particular point in the weld, the fraction of each clay color present can be determined. To estimate the uncertainty in the concentration predictions, ten clay fractions, ranging from 100% cyan to 100% magenta, were randomly chosen and the plasticine mixed accordingly from

several different cyan and magenta samples. The samples were then analyzed using the procedure discussed above. The largest error in concentration level for all tests was 7% but was less than 5% for 9 of the 10 samples (see Table A-1 in Appendix A).

2.4.2 Thermal Response

Heating inside the weld region was explored through the use of thermocouples. Temporal responses from the two thermocouples at the weld centerline and at the advancing side shoulder edge (both at approximately mid-pin depth) are plotted in Figure 2-4a and b, at two tool rotational rates of 500 and 1500 rpm.

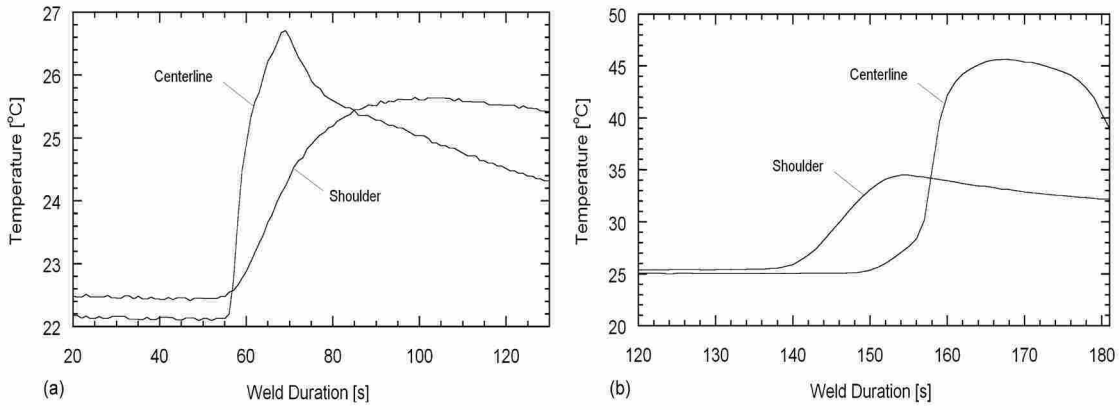

Figure 2-4: Temperature response from thermocouples at weld center and advancing shoulder edge. Welds conducted with a 1.1 mm/s traverse speed: (a) 500 rpm; (b) 1500 rpm.

Note that for each weld the two thermocouples were placed at different locations along the welding direction (*i.e.*, the shoulder thermocouple location for the 1500 rpm weld was encountered by the tool before the centerline thermocouple). The lower-rpm weld shows lower heating compared to the weld conducted at high rotational speed. At

500 rpm, the temperature at the centerline increases by over 4°C, while at 1500 rpm, a maximum temperature rise of approximately 20°C is observed. At the centerline the lower rotational speed weld shows a steeper gradient at the onset of heating and cools more rapidly compared to the high-rpm weld.

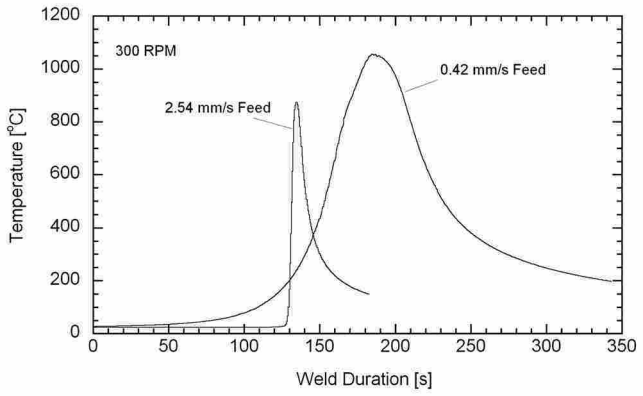

Figure 2-5: Temperature response from thermocouples located 5 mm from weld centerline on the advancing side in 304L stainless steel. Welds were conducted at 300 rpm with a traverse speed of 2.54 mm/s and 0.42 mm/s.

The initial steep temperature increase of the low-rpm weld is due to the relatively high travel speed of the tool compared to the advancing thermal wave. These general heating trends observed in plasticine are also documented in metals. Figure 2-5 shows thermocouple readings from welds conducted in 304L stainless steel at 300 rpm with a tool travel rate of 2.54 and 0.42 mm/s, respectively. (The 304L welds were performed using a scrolled shoulder and pin tool on the same mill that was used for the plasticine welds.) Like the plasticine weld, the initial temperature increase of the colder 304L weld is more rapid compared to the hotter weld, which shows a more gradual thermal increase and subsequent decrease. It is observed that the use of plasticine as the weld medium requires an adjusted set of operational parameters, compared to those used in a metal

weld, to mimic material flow in FSW of metals. The transient temperature response during welding provides one mechanism for determining the range of operational parameters for plasticine that corresponds to metal welds.

2.4.3 Plasticine Color Similarity

Initially, welds in the softer plasticine were conducted using dark blue and white colors placed on either side of the weld. These colors were chosen to provide high contrast. However, it was discovered that weld cross-section characteristics differed depending on whether the white clay was initially on the advancing or retreating side, as shown in Figure 2-6.

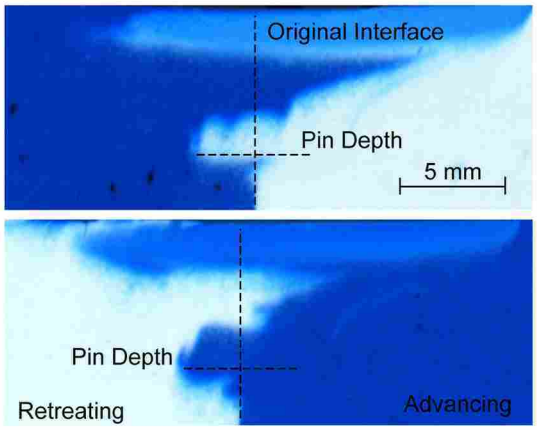

Figure 2-6: Weld side dependence comparison of blue/white plasticine (450 rpm, 1.1 mm/s traverse speed).

The figure shows transverse (perpendicular to welding direction) sections cut from two different welds. This result suggests color-dependent material properties. The weld with blue clay at the retreating side has a flow arm that penetrates much deeper into the advancing side compared to the weld with white plasticine on the retreating side. In

addition, with the white plasticine on the retreating side, the mixed region immediately below the shoulder is approximately 79% advancing material while the reverse-configuration weld shows a nearly uniform concentration (50%) of blue and white clay in this region. It is concluded that the white clay contains titanium dioxide (rather than the dye used for pigment in the blue), making it slightly harder than other plasticine colors. Figure 2-7 shows cyan/magenta clay cross-sections from welds conducted using a smooth pin at 450 rpm and 1.1 mm/s with each color on either side of the weld. These two colors are weld-side independent, where data for the inverted configuration are obtained and only minor differences are present. The mixed area below the shoulder is approximately 68% advancing material with the magenta clay on the advancing side, and 74% advancing material with the cyan clay on the same side. Unless stated otherwise the results reported hereafter employ the cyan/magenta plasticine combination with the threaded pin tool described above and a single feed rate of 1.1 mm/s.

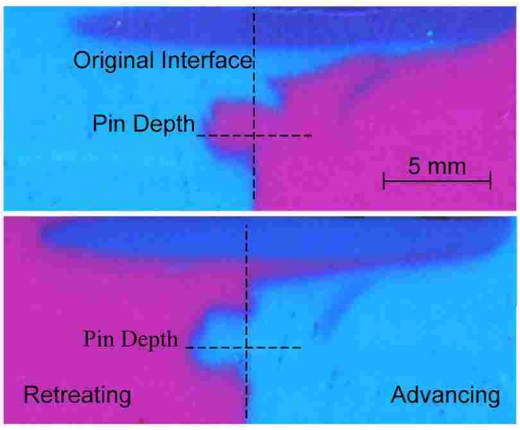

Figure 2-7: Weld side dependence comparison of cyan/magenta plasticine (450 rpm, 1.1 mm/s traverse speed).

2.4.4 Van Aken Plasticine/Metal Flow Similarities

Figure 2-8 compares cross-sections of welds conducted at rotational speeds of 250, 500, and 1500 rpm and feed rates of 0.21, 1.1 and 1.7 mm/s. The cyan clay is on the advancing side of the weld and magenta is on the retreating side. Note that welds were partial-penetration welds (with the pin depth indicated on the figure), and an unwelded area is seen at the bottom of the workpiece. These cross-sections show a large difference between welded sections. In FSW a large macroscopically-mixed region where the advancing/retreating weld interface is no longer distinguishable typically characterizes a hot weld, *i.e.*, as exhibited by the 1500 rpm figure. At the other extreme, a cold weld shows no large-scale mixing and the weld interface is clearly discernable (although displaced). These same definitions for "hot" and "cold" welds are used here for plasticine.

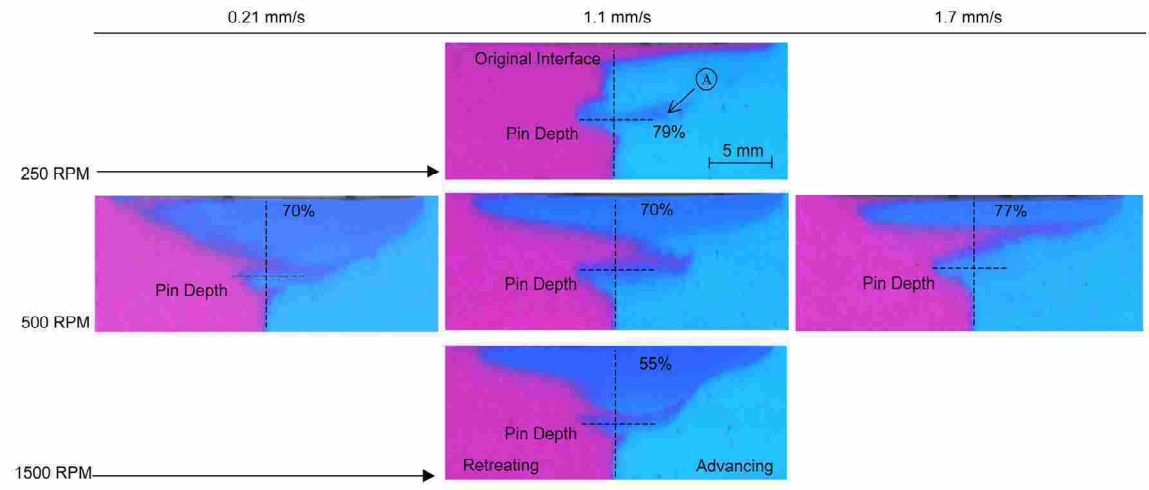

Figure 2-8: Plasticine welds performed at 250, 450, and 1500 rpm and tool traverse speeds of 0.21, 1.1, and 1.7 mm/s with a threaded pin.

At 250 rpm, the welded clay shows very little mixing at large scales, and a flow arm consisting only of retreating side material penetrates across the weld just under the tool shoulder. There is a region near the bottom of the weld, indicated by point A in the figure, where retreating side material has penetrated the advancing side. In this and other figures which follow, the calculated fraction of cyan material in a mixed region is shown as a percentage in the image. On average the small mixed region in the 250 rpm weld is approximately 79% cyan plasticine. Aside from this mixed zone, the interface between weld sides is clearly distinguishable.

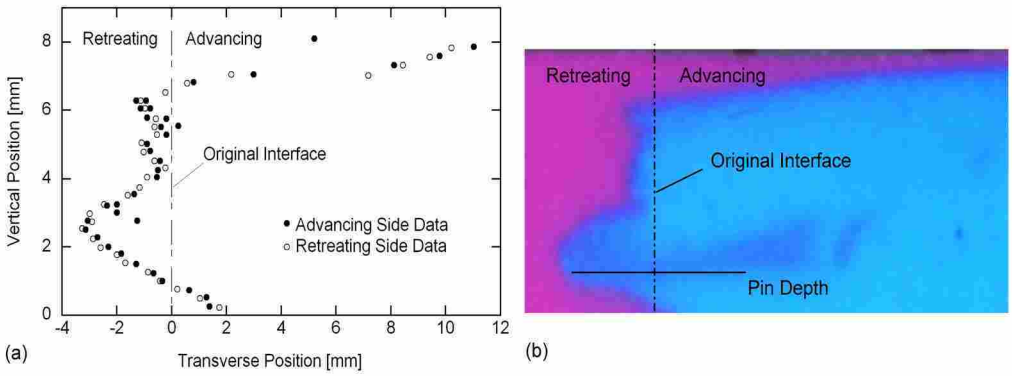

Figure 2-9: Advancing/Retreating interface from a) aluminum weld from Reynolds [6], and b) cyan and magenta plasticine.

Figure 2-9a shows a map of advancing and retreating 5454 Al markers at the interface from a full penetration weld conducted in 2195-T8 aluminum, as reported by Reynolds [6]. Reynolds noted that the interface line determined from both the advancing and retreating side aluminum markers is nearly identical, and no large-scale mixing occurred. Remarkable similarity is observed in the interface characteristics between the aluminum weld from Reynolds experiment and the partial penetration 250 rpm clay weld from this study (Figure 2-9b). Both welds exhibit a large flow arm across the top of the

weld. In addition, the interface in the lower half of the weld (near the bottom of the pin) is shifted significantly to the retreating side of the weld.

As the rotational speed increases to 500 rpm, a region of clay directly under the tool shoulder begins to mix (for all feed-rates investigated), and the interface immediately below this mixed zone shifts to the advancing side of the weld. Regardless of feed rate, at 500 rpm the mixed material at the surface contains 70 to 77% cyan material, increasing slightly with the highest feed-rate. At the lowest feed-rate (500 rpm), mixing in the weld region is substantial and the section is comparable to the 1500 rpm weld. With these two conditions, mixing is nearly complete (no distinct weld interface) throughout the stir-affected zone, except perhaps very near the bottom of the pin. However, the mixture of cyan and magenta in the 1500 rpm weld contains a more uniform concentration of cyan and magenta (55%) than the lower feed rate weld (70%). Complete destruction of the interface line has been observed previously in aluminum FSW [5] and uniform mixing of the two weld sides is seen in 7075 aluminum welds under similar hot-weld conditions [17]. The weld pitch (tool feed/rotation) for the 1500 rpm (1.1 mm/s) and 500 rpm (0.21 mm/s) welds is only 0.044 and 0.025 mm/rot, respectively. The very low weld pitch for both cases explains the relative similarity between the two welds. However, the weld pitch for the 250 rpm (0.264 mm/rot) and 500 rpm high feed-rate case (0.204 mm/rot) are nearly identical but the cross-sections differ considerably. Therefore, weld pitch alone does not account for differences in material flow. Rather, the material flow is a function of feed-rate and rotational rate.

A similar investigation with a smooth pin tool (no threads) is shown in Figure 2-10. Consistent with the threaded pin, mixing is significant near the shoulder at

rotational rates above 500 rpm (regardless of feed rate and weld pitch). Although the cross-section for the 500 rpm and 0.21 mm/s weld exhibits a significant mixed area at the upper part of the weld, it is distinctly different from the other welds at the same rotational rate. Rather than a uniform mixture near the surface, the mixed region has been pushed to the advancing side of the weld. The exact cause for this deviation is unknown, but is likely due to the thermal response and associated material softening for this operating condition (plasticine constitutive behavior will be discussed in Chapter 3). As already noted in Figure 2-4, temperature increases during FSW can be very sudden or more gradual, depending on operating conditions. Though some similarity is observed between the threaded and smooth pin welded sections in Figure 2-8 and Figure 2-10, the 1500 rpm weld for each case is dramatically different. At 1500 rpm, the area near the bottom of the weld is unmixed in the smooth pin weld, and the interface between the two colors is obvious. Therefore, as expected, in addition to operating conditions, material flow is also a function of tooling.

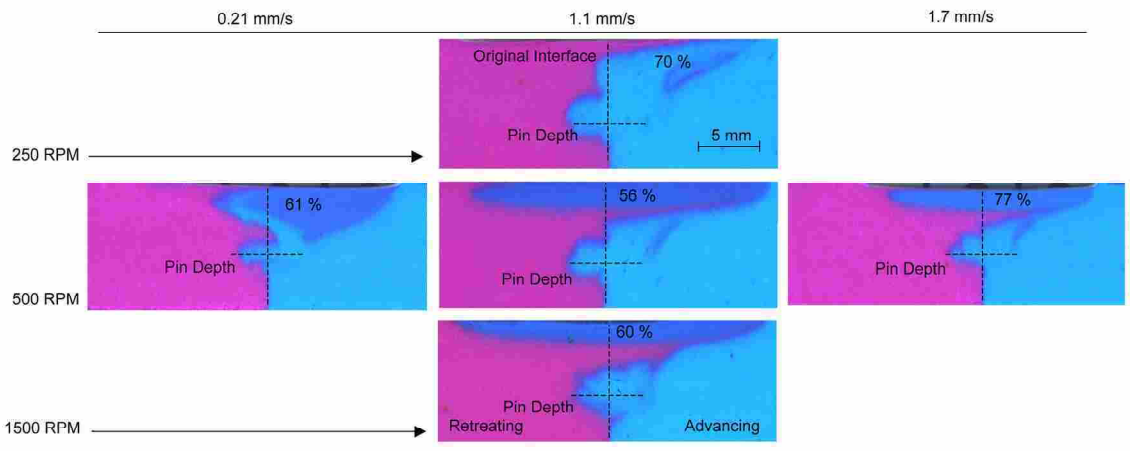

Figure 2-10: Plasticine welds performed at 250, 450, and 1500 rpm and tool traverse speeds of 0.21, 1.1, and 1.7 mm/s with a smooth tool pin.

Visualization of material movement in the tool feed direction was achieved by cutting a groove (approximately 5 mm wide by 7 mm deep) into a workpiece of magenta plasticine and inserting a dark blue marker on the retreating side and a cyan marker into the advancing side, as shown schematically in Figure 2-11a. The tool (threaded) was then passed through the markers at 250 rpm and 1.1 mm/s, corresponding to cold-weld conditions. Plan view sections at vertical depths of 0, 1, 3, and 6 mm, corresponding to 0, 15%, 46%, and 92% of the pin length (each indicated by a black line in Figure 2-11b), respectively, were investigated and are presented in Figure 2-11c. At the top of the weld, the retreating side marker has been pulled across the weld by the back of the tool shoulder. This feature corresponds to the weld arm seen in the cross-sections previously discussed. Just under the flow arm, however, the interface between the two markers is shifted slightly to the retreating side of the weld. This interface is pushed even further from the centerline deeper into the weld near the vertical midplane. At each of these depths, the advancing side marker is carried forward with the motion of the tool and rotated behind the pin, while the retreating side marker only moves backward relative to the tool motion. The last section shown was taken from the mixing region near the bottom of the pin. Here, the marker interface is shifted significantly to the retreating side of the weld and marker material is carried for a short distance with the pin (the marker material ends a short distance beyond the edge of the photograph). The general deformation characteristics of plasticine during FSW matches plan view sections presented by Reynolds [6] using a similar marker insert method. A portion of Reynolds' work, showing a plan view section slightly below the weld midplane, is reproduced here in Figure 2-11d. The vertical dotted line across the white marker represents the interface

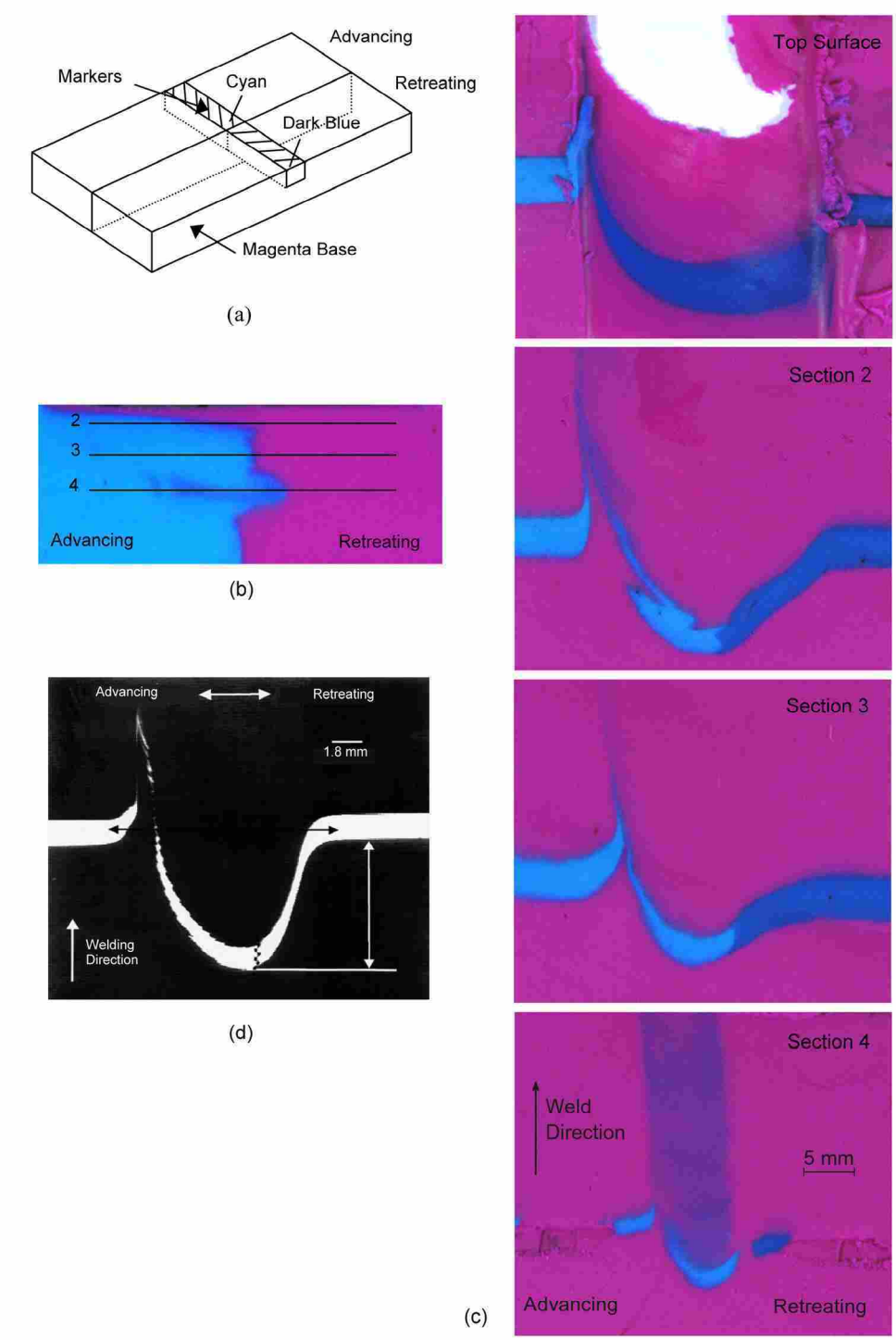

Figure 2-11: Weld performed in workpiece with contrasting marker inserts: (a) contrasting marker insert setup sketch; (b) cyan/magenta butt weld cross-section from weld (250 rpm and 1.1 mm/s traverse speed) showing corresponding horizontal section cut locations for marker insert study; (c) marker insert weld horizontal sections at several vertical depths (250 rpm, 1mm/s traverse speed); (d) weld horizontal section (slightly below weld mid-plane) of aluminum weld using similar marker insert technique from Reynolds [6].

between advancing and retreating side markers. This line is shifted laterally toward the retreating side of the weld. A similar shift is observed in the plasticine weld, where the final marker positions for the plasticine and aluminum welds in Figure 2-11c and d (Section 3) are nearly identical.

Depending on operational parameters, during FSW of metals it has been observed that some material, called flash, is expelled from beneath the tool shoulder at the top surface of the weld at the retreating side of the tool. Kim *et al.* [15] reported that flash occurs in aluminum welds when the down-force is large, resulting in an increased tool depth in the workpiece. Significant changes in the material flow features can be realized by changing the tool depth. Generally, the sections presented previously that show a large region of uniformly mixed cyan and magenta colored plasticine under the shoulder were conducted with some flash generation. However, welds were also carried out at 250 and 1000 rpm and a feed rate of 1.1 mm/s with an adjusted tool depth in order to achieve more or less mixing. Since the mixing was relatively minor at 250 rpm for both the smooth and threaded pin, the tool depth was increased to determine if large scale mixing could be realized at the lower rotational rate. Samples from welded sections using the threaded and smooth tool at the increased depth are shown in Figure 2-12 (250 rpm). Note that for each weld, the tool depth was such that a large amount of flash was generated and the leading edge of the tool was approximately 1 mm below the surface of the workpiece. Despite the differences in tool pin, the two sections in Figure 2-12 are nearly identical (aside from the cyan fraction in the mixed region). Differences are noticeable between Figure 2-12 and shallower conditions for the threaded (Figure 2-8) and smooth pin (Figure 2-10) at 250 rpm and 1.1 mm/s feed-rate. The distorted interface

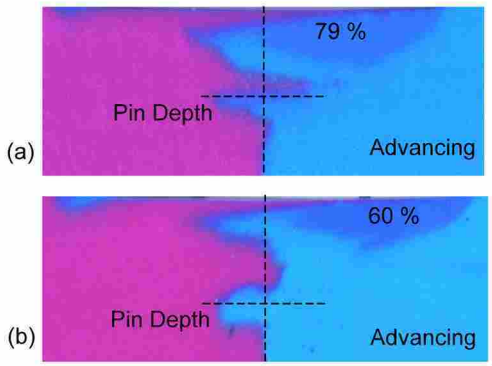

Figure 2-12: Cross-sections of plasticine welds performed at high tool depth such that the leading edge of the shoulder was 1 mm below the surface of the workpiece (250 rpm, 1.1 mm/s feed): (a) threaded pin; (b) smooth pin.

is significantly different than the previous welds at same rotational and feed rate where the cyan advancing material is observed to penetrate well into the magenta material at the upper portion of the weld. However, even at this extreme tool depth, material mixing directly under the shoulder is not as dominant as at the higher rotational rates above 500 rpm. Additionally, unlike the 250-rpm weld with the threaded pin in Figure 2-8, the mixed area at the bottom of the pin is absent, and similar to the smooth pin, the region at the upper advancing side is a mixture of cyan and magenta colors. At such a high tool depth, material flow is influenced mainly by the shoulder, and pin effects are minimal.

Differences in material flow features at 1000 rpm are also noticeable with varying tool depth. Presented in Figure 2-13 are cross-sections from cyan/magenta butt welds conducted at 1000 rpm and 1.1 mm/s at two different tool depths. When flash is created during welding at this high rotational speed, there is a significant mixing region in the upper half of the weld that is consistent with the 500 and 1500 rpm welds presented in Figure 2-8 (at the same feed-rate). This large mixed region under the tool shoulder is absent in a weld created without flash, and the transverse section more closely resembles

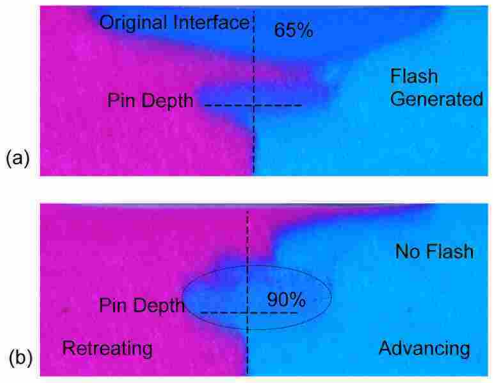

Figure 2-13: Plasticine welds performed both with and without flash generation (1000 rpm and 1.1 mm/s tool traverse speed): (a) cut cross-sections; (b) corresponding surface plots of advancing (cyan) fraction in weld region.

the 250 rpm weld in Figure 2-8. However, the center of the weld conducted at 1000 rpm has a larger mixed region compared to the 250 rpm weld. Although virtually no flow lines can be seen in this mixed region, there is evidence that its elliptical shape corresponds with the "onion ring" patterns that have been observed in aluminum FSW [3, 5, 8, 17, 39]. The size, shape, and location of the ring pattern and the mixing region are nearly identical (both in this weld and others presented in sections to follow). Like the ring patterns in aluminum, the mixed plasticine region is roughly elliptical in shape. It is possible that the rings observed in joined metals are due to the strain and/or thermal history of the material during FSW, which would not be apparent with the plasticine. Loading and thermal cycles could cause property variations in the metal that would be observable in etched sections. Unlike tempered metals, properties of plasticine do not significantly change under a thermal cycle and any variation in the clay due to strain effects would not be evident in sections directly cut from the weld. Furthermore, it has been observed that some alloys (namely 7075 Al) do not exhibit the ring pattern after welding, and similar to plasticine, more uniform mixing occurs [17]. If the development

of this mixed clay region can be characterized, then valuable insight to the formation of the onion rings in metals may also be gained.

Some previous studies [5, 8] have concluded that material travels several times around the rotating pin, traveling forward with the tool (which would increase the amount of large-scale mixing in the weld). Guerra *et al*. [8] were able to observe this region by suddenly stopping the tool during welding, and subsequently cutting a horizontal (plan view) section through the mid-pin depth of the weld. Figure 2-14 shows a horizontal (plan view) section cut at the mid-pin depth of a cyan/magenta butt weld (weld parameters were 1000 rpm, 1.1 mm/s, and flash tool depth) at the location where stop-action was performed. In contrast to Figure 2-11, the weld shown in Figure 2-14 was performed at a significantly higher rotational speed. Adjacent to the pin there is a ring of mixed magenta and cyan plasticine. This region surrounds the pin, rotating and translating with it. This mixed region is observed even downstream of the pin and is biased to the advancing side of the weld. This behavior is consistent with that observed in metal welds [8].

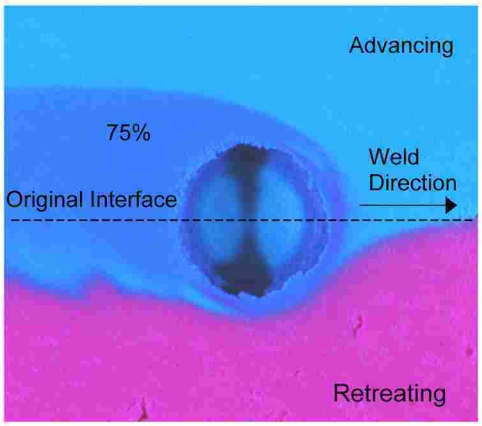

Figure 2-14: Plan view at mid-pin depth at extracted tool location (1000 rpm and 1.1 mm/s tool traverse speed).

Flow studies in FSW of aluminum have shown considerable vertical motion during FSW [8]. Vertical material motion in the plasticine welds discussed previously could not be observed because of the arrangement of the cyan and magenta plasticine in the workpieces. Vertical motion during welding was therefore analyzed by stacking a horizontal layer of cyan plasticine on top of a magenta layer (*i.e.*, a lap weld). The thickness of the upper cyan layer was half the length of the pin. Figure 2-15 shows cross-sections from two cyan/magenta lap welds conducted both with and without the presence of flash, respectively. In both welds the cyan material in the top half of the weld has penetrated into the bottom magenta plasticine. In addition, to balance the downward material flow the magenta plasticine has moved up toward the top of the weld. Consistent with welds conducted with flash creation, Figure 2-15a shows a region in the top of the section that has been mixed by the shoulder in addition to a thin mixed area near the bottom the pin. The top mixed zone is primarily cyan material and the bottom mixture is mainly magenta. When no flash is generated during welding, there is a large mixed region in the center of the weld. As explained previously, this region likely

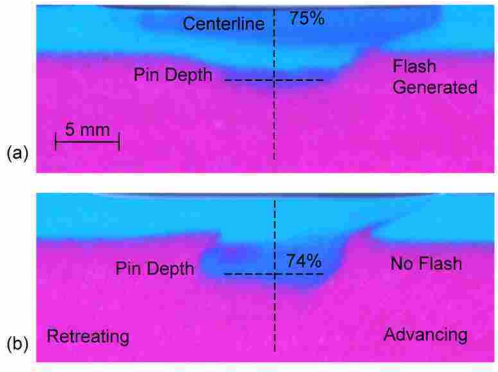

Figure 2-15: Transverse section of cyan/magenta lap welds both with and without flash generation (1000 rpm and 1.1 mm/s tool traverse speed): (a) cut cross-sections; (b) corresponding surface plots of advancing (cyan) fraction in weld region.

corresponds to the onion ring pattern seen in many metal FSW welds. This region contains more of the upper cyan material compared to the bottom of the weld with flash. The top of the weld contains only cyan material except for a thin line of magenta that penetrates to the top surface.

All of the weld sections presented above are from partial penetration welds. Lap welds were also investigated at 1000 rpm under full penetration conditions. Results for both flash and no flash tool depths are shown in Figure 2-16. The welded section for each case is nearly identical to the corresponding case in Figure 2-15; therefore, it is assumed that flow features are independent of a partial or full penetration weld.

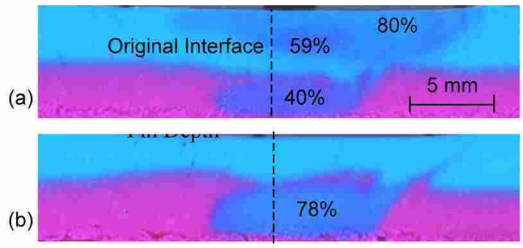

Figure 2-16: Transverse section of cyan/magenta full penetration lap welds both (a) with and (b) without flash generation (1000 rpm and 1.1 mm/s tool traverse speed).

In summary, many of the weld deformation features observed in the plasticine compare well with limited material flow studies performed in metals. General similarities between metal and plasticine FSW include (dependent on operational parameters) corresponding advancing/retreating side interface distortion, similar deformation in plan sections, significant vertical motion from pin threads, both simple extrusion and a region of entrained material which rotates many times with the tool, and a qualitatively similar thermal response. It was also demonstrated that material flow features were independent of cyan and magenta colors of the particular plasticine.

Furthermore, multiple colored layers of the plasticine can be fused by compression of the layers, eliminating discontinuities between layers. The ability to combine multiple contrasting layers of the plasticine to form a more homogenous workpiece allows for observation of material flow with minimal intrusion.

3 Thermo-Mechanical Response and Similarity

The use of plasticine as a physical model to study the flow behavior of metal forming processes has been a viable method since the work of Green [21] in the early 1950's. Early work using the physical modeling technique (PMT) was largely qualitative. Identification of dimensionless similarities laws, however, has enabled a quantitative aspect to the PMT, including predictions of forming pressures [40] and workpiece strain/strain-rate and temperature distributions [19]. Boer et al. [41] has outlined several similarity laws that must be satisfied for a model material to mimic a metal forming process including: 1) physical (or geometrical) similarity, 2) mechanical or flow stress similarity, 3) tool/workpiece friction similarity, and 4) thermal similarity. Often, it is not possible to satisfy all similarity laws exactly (thermal similarity proving the most difficult). In many engineering applications, however, approximate solutions are sufficient. Similarity is established through dimensionless parameters, which can be used to correlate results from the model to the actual metal forming process [41]. If the appropriate modeling material is chosen through careful analysis, it can be used to predict many behaviors of the metal, such as the temperature, strain, and/or stress distributions [19].

Substantial research has been done to validate the use of plasticine to model material flow in metal forming processes, such as extrusion, rolling, and forging [20-23]. Three-dimensional extrusion processes have previously been analyzed with physical

modeling and finite element analysis to validate the use of plasticine as a model for the behavior of both elastic-plastic materials [23] and elastic-viscoplastic materials [20]. The results of both the finite element analysis and the plasticine model were in agreement in each case.

Strain and strain hardening effects of the actual metal must be represented by the plasticine model. The physical property variations of plasticine can be used to model a range of metals by matching the properties of a certain color and/or plasticine type with the metal under examination [42]. Sofuoglu and Rasty [42] examined 16 different colors of Peter Pan Playthings Plasticine at room temperature and increasing strains. However, strain-rates during compression tests were not held constant, and it is unclear whether the increase in flow stress was caused by strain or strain-rate effects. The physical properties of Beck's green and black plasticine have also been investigated at relatively low strains (20%) and strain-rates (10^{-1}) and constant temperature [43]. At room temperature, it was concluded that strain and strain-rate hardening is significant.

Prior research with plasticine only considered relatively low strains/strain-rates and/or temperatures. Additionally, there is limited data on temperature-dependent thermal properties. In many metal forming processes, strains/strain-rates are large and deformation heating is important. For example, welding temperatures in FSW approach the materials' melting point, and strain rates on the order of 10 s^{-1} are not unreasonable.

In this chapter plasticine manufactured by Van Aken International is examined at high temperatures, strains, and strain-rates. The plasticine is directly compared to steel and aluminum alloys through a detailed similarity analysis.

3.1 Theoretical Background

3.1.1 Constitutive Behavior

Compression tests are widely performed to determine the true stress-strain relationship of a material [44]. In a typical compression test, the sample is compressed between two parallel flat plates. The time, force, and height of the sample are recorded during the test. The instantaneous magnitude of the force (F) and cross-sectional area (A) are used to determine the true stress. Note that since the sample is continuously yielding during the compression tests in this work, the true stress values presented are flow stress values. True or logarithmic strain is defined as $\varepsilon = \ln(l/l_o)$ where l is the current height and l_o is the initial height before compression. The instantaneous cross-sectional area of the sample can be determined by assuming that the material is incompressible (constant volume) and remains prismatic throughout the test (*i.e.*, $A = A_o l_o / l$). A prismatic assumption requires vanishing friction between the sample and platens [45, 46]. The sample will experience barreling and deformation due to shear if a significant frictional force exists, and the resulting compressive stress will increase appreciably [45].

Maintaining a constant strain-rate throughout the compression is essential for determining both strain and strain-rate effects. The true strain-rate is determined from the instantaneous velocity (v) and height of the sample during compression. A relationship between velocity and strain-rate can be used to create a height-time curve that will maintain a constant strain-rate. The instantaneous velocity is the time derivative of sample height,

$$v = \frac{dl}{dt}. \tag{3-1}$$

The velocity is related to the axial strain-rate by Eq. (3-2),

$$\dot{\varepsilon} = \frac{d\varepsilon}{dt} = \frac{d}{dt}\left(\ln\left(\frac{l}{l_o}\right)\right) = \frac{1}{l}\frac{dl}{dt} = \frac{v}{l} \tag{3-2}$$

or

$$\frac{dl}{dt} = \dot{\varepsilon}\, l\,. \tag{3-3}$$

Separating the variables of Eq. (3-3) and integrating over the initial and current points gives

$$\int_{l_o}^{l} \frac{dl}{l} = \int_{0}^{t} \dot{\varepsilon} dt\,, \tag{3-4}$$

which reduces to

$$l = l_o e^{\dot{\varepsilon} t}\,. \tag{3-5}$$

The strain-rate ($\dot{\varepsilon}$) in Eq. (3-5) is always negative in a compression test. For constant strain-rate compression, the sample must deform according to Eq. (3-5).

Generally, the flow stress of plasticine (and many metals) can be described as a power law function of strain, strain-rate, and temperature (T) as

$$\sigma_f(\varepsilon, \dot{\varepsilon}, T) = k_o e^{-\beta T} \varepsilon^n \dot{\varepsilon}^m\,. \tag{3-6}$$

Eq. (3-6) is commonly known as the Norton-Hoff viscoplastic model [47].

3.1.2 Friction

Under high loads, friction in metal forming processes can be represented by the Tresca friction approximation [48],

$$\tau_T = \frac{m^* \sigma}{\sqrt{3}}\,. \tag{3-7}$$

where m^* is the shear friction factor. Due to its simplicity, the shear friction factor is often determined from a ring compression test [48, 49]. In the ring compression test method, the inner diameter of a relatively thin ring of material is measured during uniaxial compression. This change in inner diameter is then related to m^*.

3.1.3 Thermal Properties

Thermal properties of interest are the thermal conductivity (k) and specific heat capacity (c_p). Using a resistance heater, a constant heat flux can be applied at the surface of a plasticine slab, as shown in Figure 3-1. The thermal conductivity of the plasticine is then determined from Fourier's Law,

$$-kA\frac{\partial T}{\partial x} = q = I\mathcal{V}\,, \tag{3-8}$$

where A is the cross-sectional area of the plasticine sample and $\mathcal{V}$ and I are the applied voltage and current, respectively. Shown in Figure 3-1, the top of the heater (temperature T_1) is insulated and the opposite side of the plasticine slab is maintained at a constant temperature (T_2).

Figure 3-1: Sketch of setup for thermal conductivity measurement.

At steady-state, the temperature profile through the plasticine slab is linear [50]. Thus, the spatial temperature gradient in Eq. (3-8) is constant over the thickness (b) of the plasticine slab. Making this substitution and solving for the thermal conductivity gives

$$k = \frac{bI\mathcal{V}}{A(T_1 - T_2)}. \tag{3-9}$$

The thermal conductivity can be estimated at multiple temperatures (approximated here as the average of T_1 and T_2) by adjusting the heat sink temperature.

The specific heat capacity can be estimated by measuring the temperature of a heated sphere (radius r_s) of plasticine as it cools. Consider a heated sphere, initially at a temperature of T_i, which is suddenly subjected to a lower (constant) temperature (T_∞) at its surface. It can be shown that the center temperature (T_o) of the sphere under such conditions varies temporally according to Eq. (3-10) [50],

$$\theta_o = \frac{T_o - T_\infty}{T_i - T_\infty} = 2\sum_{j=1}^{\infty}(-1)^{j+1}\exp\left(-(j\pi)^2 Fo\right). \tag{3-10}$$

where the Fourier number $Fo = kt/(\rho c_p r_s^2)$ and the density of the plasticine is $\rho = 1570$ kg/m^3. To determine the specific heat, $\theta_o(t)$ is measured experimentally and $Fo(\theta_o)$ and is then calculated from Eq. (3-10) using iterative methods. Finally, the specific heat capacity is determined from the definition of Fo and experimentally determined values for the thermal conductivity. Note, however, that Fo in Eq. 3-10 is assumed to be constant, which is not the case for the plasticine. Therefore, the temperature dependence of Fo (and hence c_p) obtained from such an analysis results in an integrated average response for c_p.

3.2 Experimental Procedure

Compression tests were performed with magenta colored Van Aken plasticine to determine its flow stress response as a function of strain, strain-rate, and temperature. According to the manufacturer, the material is primarily comprised of scale wax and pigments derived from calcite. Only magenta colored plasticine is examined in this section, but other colors such as cyan have shown mechanical behavior similar to magenta in FSW (see Chapter 2). Smooth samples, 3.0 cm in diameter and 5.1 cm long, were used for the compression tests. Samples were manually pressed from blocks using a 3.0 cm diameter steel tube and subsequently cut to height using a thin (0.3 mm diameter) wire. Typically, a smaller aspect ratio (height-to-diameter) is desirable to eliminate buckling. The relatively large length was chosen to reduce the amount of uncertainty in the stress measurement (see Appendix B), and the maximum diameter attainable from the as-received plasticine blocks was used. Samples from the manufactured plasticine blocks with minimal alteration were used because cold working may cause strain hardening, as noted by others [42, 43]. Thus the reference state of the plasticine is as sent by the manufacturer. It is acknowledged that samples may vary slightly between different batches of the clay. However, this variation is not large and may be reduced through averaging across tests from multiple batches. Despite the relative large aspect ratio, buckling was not a problem during compression as long as the sample ends were perpendicular to the sides of the sample.

In addition to buckling, barreling was also a concern during the compression tests. The ends of the sample were lubricated with Vaseline to reduce friction and barreling during the compression. Plastic plates were also used at the sample ends to further

reduce barreling. The compression tests were conducted at four different strain-rates (0.1, 1.0, 2.5, and 5.0 s^{-1}) and three different temperatures (24, 30, and 40ºC). Note that all strain and strain-rate values presented are in compression. To achieve the specified temperatures, the samples were placed in a temperature bath until a uniform temperature was obtained. An Instron compression/tension machine (fitted with a 4500 N load cell) capable of constant strain-rate testing was used for all tests. Each strain-rate/temperature combination was repeated at least twice to ensure validity of the results. The results of the compression tests were then fit to Eq. (3-6).

To determine the frictional behavior of the plasticine, ring compression tests were conducted [48, 49]. The dimensions of the plasticine annulus were: 3.5 cm outer diameter, 1.7 cm inner diameter, and 1.2 cm thickness (approximately 6:3:2 ratio). The ring samples were compressed at room temperature with and without Vaseline. The inside diameter of the annulus was measured during compression to determine the shear friction factor (m^*) of the plasticine using calibration curves presented by Hawkyard and Johnson [49].

The thermal conductivity of plasticine was determined using the set-up shown in Figure 3-1. The temperature plate was set to four different temperatures (20, 30, 40, and 50ºC). A steady flow of water through channels in the constant temperature plate maintained a uniform temperature at the bottom of the plasticine slab. The temperature of the heater (at the plasticine/heater interface) was measured using a K-type thermocouple. A constant voltage of 14.1 Volts was applied to the heater, which has a resistance of 12.8 Ω at room temperature. Depending on its temperature, the resistance of the heater changed slightly during testing. To account for this, the current drawn by the

heater was monitored in order to determine the power supplied to the heater. Extreme values of the current were 0.96 and 1.01 Amps at 50 and 20ºC, respectively. The size of the plasticine slab was 25 x 25 x 3.0 cm and the polystyrene insulation (k_{ins} = 0.04 W/mK) was 10 cm thick. Once steady-state conditions were reached, the temperature of the plasticine/heater interface was recorded. The outer surface temperature of the insulation (opposite to the heater) was also measured during testing to determine the amount of energy lost through the insulation. The thermal conductivity was then determined according to Eq. (3-9).

The heat capacity of the plasticine was determined by first heating a 2.7 cm diameter sphere of the material to a uniform temperature of 50ºC in a constant temperature bath. The sample was then placed in a separate temperature bath at 13ºC. Upon immersion in the "cold" temperature bath, the surface temperature of the sphere will be equal to the water temperature if the convective heat transfer coefficient is sufficiently large. A large heat transfer coefficient was achieved by placing a stirring paddle in the cold temperature bath. By observation of small particles in the water bath, the velocity under the paddle was estimated to be well above 1 m/s. This velocity resulted in a convective heat transfer coefficient larger than 6000 W/m^{2}K (calculated from widely accepted experimental data), which is sufficiently large such that the surface temperature of the sphere is equal to the bath temperature (T_∞) [50]. As the sample cooled, its temperature was recorded using a K-type thermocouple. The temperature data was then converted to a dimensionless temperature and the specific heat capacity determined according to Eq. (3-10).

3.3 Results

3.3.1 Mechanical Properties

Figure 3-2 shows the flow stress of the Van Aken plasticine at various strain-rates and temperatures. The flow stress is presented for a strain range of 0.1 to 0.7 at four different strain-rates (0.1, 1.0, 2.5, and 5.0 s^{-1}) and three temperatures (24, 30, and 40°C). Note that no measurable temperature increase occurred in the plasticine during compression at high strain-rate. Only minimal barreling was observed during compression with Vaseline lubrication. Typically, the minimum to maximum diameter ratio after compression was greater than 0.95.

Data from compressed samples with a higher minimum/maximum diameter ratio were discarded. For all strain-rates and temperatures, the curves presented are the average of multiple tests. The plots indicate that the flow stress increases with strain-rate and decreases with temperature. A maximum flow stress of approximately 210 kPa occurs at a temperature of 297 K and a strain-rate of 5.0 s^{-1}, while a minimum flow stress of approximately 30 kPa occurs at a temperature of 313 K and a strain-rate of 0.1 s^{-1}. From the uncertainty analysis given in Appendix B, the typical error in the flow stress data is less than 15%, with a higher uncertainty at 313K and strain-rates < 1.0).

The flow stress data in Figure 3-2 was fit to Eq. (3-6) using the generalized reduced gradient optimization method to minimize the sum of the squared residual between the model and experimental values. Constants for the Norton-Hoff model are presented in Table 3-1, and the curve fit (solid lines) is overlaid on the experimental data (points) in Figure 3-2. In some cases, flow stress gradients below $\varepsilon < 0.2$ are appreciably steeper than at high strain, and the Norton-Hoff model cannot adjust with the rapid

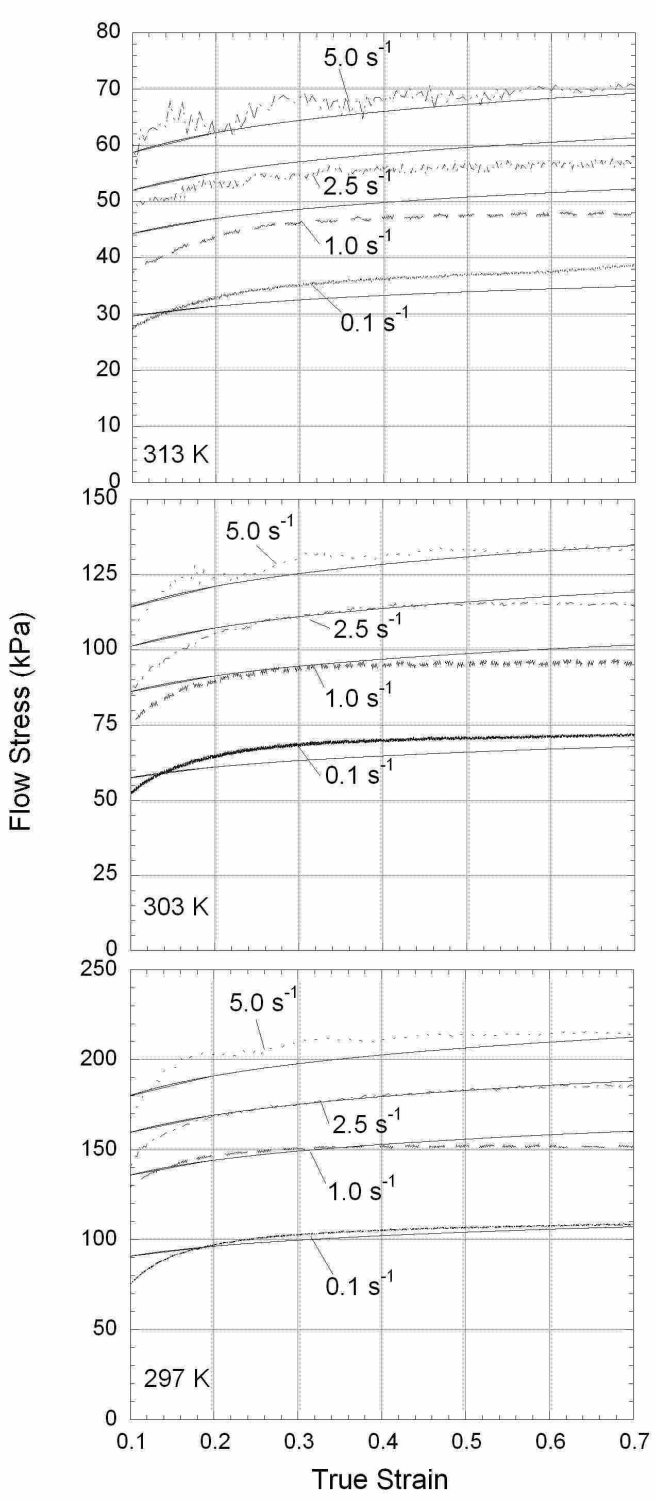

Figure 3-2: Variation in Van Aken plasticine flow stress at 297 K, 303 K, and 313 K and several strain-rates. Points are from experimental data and solid lines are Norton-Hoff curve fit.

Table 3-1: Norton-Hoff coefficients for the flow stress of Van Aken plasticine.

Parameter	Value
k_o [kPa]	1.820E11
n	0.0850
m	0.1750
β	0.0701

decrease in material strength. Therefore, error in the curve fit becomes large at low strain. Aside from low strain values ($\varepsilon < 0.2$) the Norton-Hoff model fits the data well, with a maximum error less than 10% between the fit and experimental data. The non-zero strain and strain-rate sensitivities (n and m, respectively) indicate that the plasticine is a strain and strain-rate hardening material. Strain hardening of the clay, however, varies with the strain level. The plots show that at low strains, strain hardening is important and generally cannot be neglected. Above a true strain of approximately 0.3 - 0.4, however, the flow stress appears to be nearly independent of the strain level ($n \rightarrow 0$). This behavior is consistent for all strain-rates and temperatures tested, except perhaps for the lowest strain-rate at 313 K, which appears to increase more rapidly past a strain of approximately 0.6. Experimental data obtained under this scenario, however, contains the largest amount of uncertainty (see Appendix B).

Figure 3-3 is a plot of the shear friction factor of plasticine with and without lubrication. Note that two tests were conducted for each boundary condition. The solid lines in the graph are calibration curves determined by Hawkyard and Johnson from a numerical simulation [49]. These calibration curves are independent of material and depend only on the initial geometry of the sample (6:3:2 ratios). Data from both unlubricated tests are similar and show a significant reduction in the inner diameter of the plasticine ring. The unlubricated data falls between $0.7 < m^* < 1.0$. The shear friction

factor is difficult to determine precisely from the curves since points do not follow the shape of the calibration curves exactly. This discrepancy can be explained by the initial size of the plasticine ring, as the size of the rings deviated by a few percent from the exact 6:3:2 ratios used in the computer model. The inner diameter of both samples lubricated with Vaseline increased during compression and the shear friction factor is between $0.10 < m^* < 0.15$. Since $m^* > 0$ with the Vaseline, a small frictional force is present at the boundary of the plasticine and plastic plates during compression. Equation (3-7) predicts that this shear stress is approximately 9% ($m^* = 0.15$) of the materials flow stress. However, the combined compressive and shear stress field results in an increase in the principal stress (and flow stress in this case) of only 0.3%.

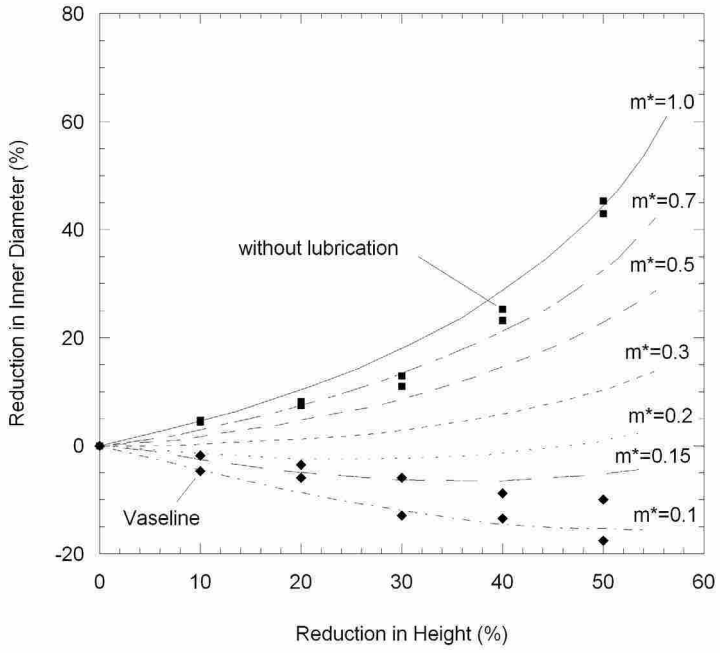

Figure 3-3: Shear friction factor of Van Aken plasticine with and without lubrication (data points). Calibration curves are from a computer simulation presented by Hawkyard and Johnson [49].

3.3.2 Thermal Properties

The thermal conductivity (k) of the plasticine was determined at several temperatures using the setup in Figure 3-1. During testing, the outer surface of the insulation remained constant at room temperature, indicating that all heat generated from the heater was conducted through the plasticine slab. For each plate temperature used (T_2 = 20, 30, 40, and 50°C) the thermal conductivity of the plasticine remained at a constant value of k = 0.65 ± 0.05 W/mK (refer to Appendix B for uncertainty analysis).

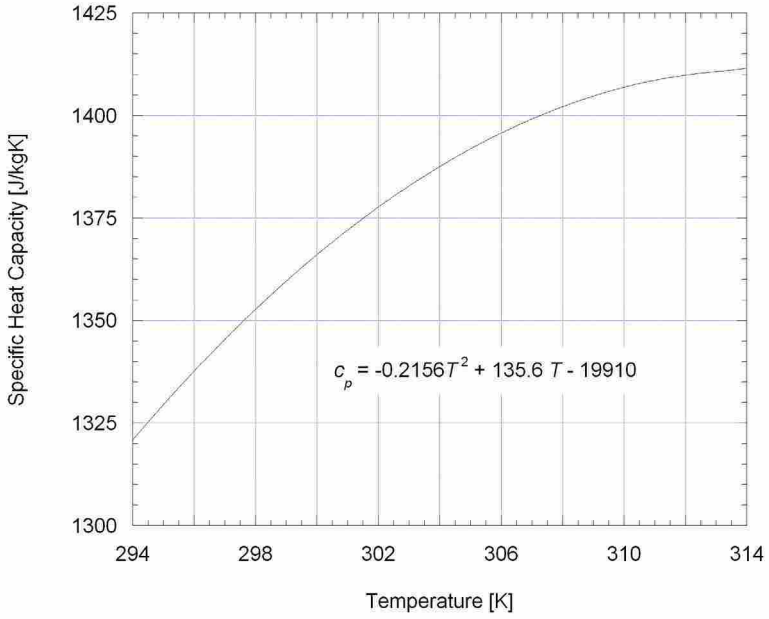

Figure 3-4: Temperature dependent specific heat capacity of Van Aken plasticine.

As explained previously, the specific heat capacity of the plasticine was estimated by suddenly exposing a heated (323 K) sphere of the material in a cold environment (286 K) with a high convection coefficient in two temperature baths. Results from multiple cooling tests are plotted in Figure 3-4. Note that the experimental data was sampled at 1000 Hz and averaged over every 100 points using Labview. The experiment was

repeated and the two results averaged, which resulted in the smooth curve shown in the figure. The figure shows the specific heat capacity of the plasticine between the temperature range of 294 to 314 K. Values near the cold and hot temperature baths are not plotted because errors of several hundred percent can result at the two extremes. The specific heat capacity increases slightly with temperature from 1320 J/kgK at 294K to 1410 J/kgK at 313K. As discussed in Appendix B, the error in c_p over this temperature range is approximately 18%.

3.4 Van Aken Plasticine/Metal Similarity

It is informative to quantitatively compare plasticine with metals to validate its use as a physical analog. For similarity, the plasticine model must be correlated to the actual metal weld in four areas, including; geometric, dynamic response, material mechanical behavior, and thermal response. Geometric similarity requires that all tool features for plasticine and metal welding (*i.e.*, shoulder and pin diameters and pin length) are scaled by a single arbitrary constant value. In modeling FSW, the inertial response is often completely omitted [32, 34] due to its negligible contribution to material flow. With this assumption, dynamic similarity is not a requirement for plasticine and metal FSW. In fact, by non-dimensionalizing the governing equation for momentum transport, it can be shown that an inertial response is negligible if the ratio $\rho v_c L_c/\eta_c \ll 1$, where v_c, L_c, and η_c are a characteristic material velocity, tool size, and material viscosity, respectively. This ratio is commonly referred to as the Reynolds number. Due to the high effective viscosity, the Reynolds number for both plasticine and metals approaches zero, and dynamic similarity is always matched for FSW of the two materials.

Mechanical similarity is then achieved through a correlation between the flow stress of the two materials. In general, the flow stress of the plasticine follows the Norton-Hoff model (Eq. (3-6)) well. This behavior corroborates the conclusion of others [20, 45, 51], that plasticine is a viscoplastic material (like many metals at high temperature). Specifically, for rheological similarity, the ratio of the flow stress of the model and actual material must be constant [19]. Under identical strains and strain-rates this requires that $n_M = n_A$, and $m_M = m_A$, where subscripts "M" and "A" refer to the plasticine model and actual material (presumably metal), respectively. Typical values for aluminum and steel at elevated temperatures are $0.05 < m < 0.30$ and $0.10 < n < 0.50$ [16, 44]. The strain-rate sensitivity ($m = 0.175$) of the plasticine is very similar to many steel and aluminum alloys. The strain hardening value of the plasticine ($n = 0.085$) is comparable to metals that do not experience significant strain hardening. Note that at high strain-rates and temperatures, strain hardening effects in many metals are often neglected ($n \rightarrow 0$) [16, 44, 52], which is a good assumption for the Van Aken plasticine.

To determine β for various aluminum alloys, the Zener-Hollomon flow stress model modified by Sheppard and Jackson (1997) was refit to Eq. (3-2) at temperatures above 400K for several different aluminum alloys with better than 99% accuracy for each alloy selected, 1050, 2024, 5054, 6061, and 7050. For all alloys examined, the temperature sensitivity is between $0.004 \leq \beta \leq 0.006$. Comparison of the temperature sensitivity between the plasticine and aluminum reveals that the plasticine ($\beta = 0.070$) is much more sensitive to temperature changes than aluminum. However, the range of material temperature change during FSW is quite different between the plasticine model and actual metal. For example, in FSW the temperature difference between the

deforming metal and material just outside the deformation zone might be a few hundred degrees, whereas with plasticine the temperature difference is only 1 to 10 K, depending on operating parameters (see Chapter 2). Since the temperature excursion of the model material differs significantly from the actual material, $\beta_M = \beta_A$ and $m_M = m_A$ is not adequate for similarity in FSW. To achieve similarity between the actual and analog material in FSW, we seek an identical fractional reduction in the flow stress over the range of process temperature excursion between the highly deforming material and material just outside the processing zone. This is achieved if

$$\left(\frac{e^{-\beta T_{high}}}{e^{-\beta T_{low}}}\right)_M = \left(\frac{e^{-\beta T_{high}}}{e^{-\beta T_{low}}}\right)_A , \tag{3-11}$$

where T_{high} is the highest temperature experienced during the weld and T_{low} is the temperature just outside the deforming region. Equation (3-11) can be simplified to give $(\beta\Delta T)_M = (\beta\Delta T)_A$ where $\Delta T = T_{high} - T_{low}$. Furthermore, by accounting for the process temperature scale in this manner, a rudimentary attribute of thermal similarity is incorporated into the physical model. Previous thermocouple data show a representative temperature difference as low as approximately 50 K [30] to nearly 300 K [53]. This temperature difference gives $0.2 < (\beta\Delta T)_A < 1.8$. A 1 to 10 K change in material temperature in the plasticine during FSW results in $0.1 < (\beta\Delta T)_M < 1.0$. Thus, a significant range of the scaled temperature sensitivity of aluminum and plasticine coincide.

To complete mechanical similarity, frictional boundary conditions must be considered. At a relatively high normal stress, the frictional stress can be approximated according to Eq. (3-7). If similarity is achieved in the material flow stress, then the shear

friction factor (m^*) between the plasticine and actual material is all that remains for mechanical similarity. Typically, the shear friction factor of a metal-metal interface approaches 1.0 [16, 54]. For an unlubricated plasticine/metal boundary $0.7 < m^* < 1.0$ and similarity holds between the plasticine and metals. Often, however, a lubricant is used in forming processes of metals to reduce friction [54]. The plasticine sample lubricated with Vaseline demonstrates that the shear friction factor between plasticine and a metal interface can be reduced to lower values. When lubricant is used in a forming operation it is a simple matter of identifying a lubricant for the plasticine such that m^* is identical to the actual conditions [48].

It is also informative to compare dimensionless thermal parameters determined from the normalization of equations governing thermal transport. Assuming constant material properties, heat transfer is governed by Eq. (3-12),

$$\dot{T} + v_i T_{,i} = \alpha T_{,ii} + \kappa\left[2v_{i,i}^2 + \left(v_{i,j} + v_{j,i}\right)^2\right], \tag{3-12}$$

where the thermal diffusivity, $\alpha = k/\rho c_p$, is the ratio of thermal conduction to heat storage, $\kappa = \eta/\rho c_p$, and η is the effective viscosity of the flowing material. Commas in Eq. (3-12) denote spatial differentiation. The two terms on the left hand side of Eq. (3-12) are the time rate of change in temperature and thermal advection, respectively. The first term on the right side of the equation represents energy diffusion and the last term on the same side accounts for viscous (deformation) heating. Introduction of the dimensionless parameters $t^* = \alpha t / L_c^2$, $x_i^* = x_i / L_c$, $v_i^* = v_i / v_c$, and $\theta = T / T_c$ (where the subscript "c" denotes a characteristic value) into Eq. (3-12) results in

$$\dot{\theta} + Pe\, v_i^* \theta_{,i} = T_{,ii} + Pr\, Ec\left[2\left(v_{i,i}^*\right)^2 + \left(v_{i,j}^* + v_{j,i}^*\right)^2\right]. \tag{3-13}$$

The dimensionless numbers in Eq. (3-13) are the Peclet number ($Pe = v_c L_c/\alpha$), Prandtl number ($Pr = c_p \eta_c/k$), and the Eckert number ($Ec = v_c^2 / c_p T_c$). If the imposed boundary condition is a heat flux due to friction, then it can be expressed in terms of the shear stress (τ_c) and a characteristic velocity as $q" = \tau_c v_c$. A dimensionless heat flux at the tool interface is $Q = q"L_c/kT_c$. This dimensionless wall heat flux, along with *Pe* and *PrEc* product must be matched between the model and actual process for thermal similarity. However, the similarity analysis can be simplified if the material is viscoplastic and yielding occurs at the tool interface. In this scenario, the effective viscosity can be determined as $\eta = \sigma_f(T, \dot{\varepsilon}_e)/3\dot{\bar{\varepsilon}}$ [24], where $\dot{\bar{\varepsilon}}$ is the local effective strain-rate [24]. If the material is yielding at the tool then $\sigma_f = \sqrt{3}\tau_c$ (von-Misses yield criteria) and the effective viscosity becomes $\eta_c = \tau_c / \sqrt{3}\dot{\bar{\varepsilon}}$. Using a characteristic strain-rate of v_c/L_c and substitution of η_c into the Prandtl/Eckert product results in $PrEc = Q/\sqrt{3}$. Therefore, the thermal boundary condition and deformation heating can be matched by choosing an appropriately scaled model value for the product $v_c L_c$. This, however, leaves no "free" parameter (unless different types of plasticine or modeling material are considered) for matching the Peclet number between the model and actual process, and therefore, *Pe* must match "naturally."

Representative values of the dimensionless parameters for FSW of plasticine and aluminum are listed in Table 3-2. Note that in Table 3-2, the characteristic length of both the model and actual process are equivalent, and the characteristic material velocity (assumed to be the tangential velocity of the pin as in a sticking condition) is scaled between plasticine and aluminum to achieve similarity. It should be noted that the

characteristic velocity is the velocity of material, not necessarily the tool, but may be a function of the tool rotational rate. This velocity cannot generally be controlled directly in FSW since slipping may occur at the interface. However, it is generally believed that increasing the tool rotational rate also causes an increase in material velocities at the tool, thus to at least some extent, the material velocity may be adjustable in some cases. Approximate values for the tool/material shear stress were determined from experimental torque data. The characteristic temperature is defined as the difference between the flowing and undeforming material temperature (identical to the value used for mechanical similarity in the Results section). Thermal conductivity (k) and diffusivity (α) values are only approximate as these values may vary with temperature, and between different aluminum alloys.

Table 3-2: Typical characteristic parameters for friction stir welding of aluminum and plasticine (assuming a no-slip tool/material boundary condition).

Term	Aluminum	Plasticine
k_c [W/m K]	150	0.65
L_c [m]	0.008	0.008
ΔT_c [K]	200 [7]	5 [7]
v_c [m/s]	0.200	0.015
α_c [m^2/s]	6.1E-5	3.2E-7
η_c[kPa s]	1155	21.55
τ_c[kPa]	50,000	70
Dimensionless Numbers		
Heat Flux, Q	2.67	2.67
Pe	26.2	375
PrEc	1.54	1.54

Using the values listed in Table 3-2, similarity in the thermal boundary condition, and deformation heating between a typical aluminum alloy and the plasticine during FSW requires that $(v_cL_c)_p = 0.075(v_cL_c)_{al}$, where subscripts *"al*" and "*p*" denote aluminum and

plasticine, respectively. Additionally, the Peclet number requires that $(v_c L_c)_p = (\alpha_p/\alpha_{al})(v_c L_c)_{al} = 0.005(v_c L_c)_{al}$. Therefore, *exact* thermal similarity cannot be achieved with the Van Aken plasticine. The consequence of this is that the plasticine analog cannot be directly linked to FSW of a specific metal. However, it is apparent from Chapter 2, that to some extent, thermal and mechanical similarity is maintained between the plasticine and metals. Despite the inability to correlate plasticine results with a specific metal alloy, the similarity analysis presented above permits the collection of general material flow trends and some quantitative information, which has not been heretofore possible.

In summary, the thermomechanical behavior of Van Aken plasticine has been investigated under various strain, strain-rate, and temperatures. It can be concluded that the dependence of the flow stress on strain and strain-rate for the plasticine is consistent with that of many steel and aluminum alloys. Considering differences in the magnitude of the temperature response during FSW of plasticine and metals, the temperature sensitivity of the plasticine is also within a range comparable to many metals, and mechanical similarity is possible. Furthermore, the shear friction factor approaches one at the plasticine/metal boundary, which is similar to a metal/metal interface. Dimensionless thermal parameters including the boundary heat flux, Prandtl-Eckert number describing the significance of deformation heating, and Peclet number, which describes the relative magnitude of advection and diffusive heating. It was found that similarity can be achieved in the heat source terms by adjusting the characteristic material speed at the welding tool and/or the pin diameter. However, thermal diffusion is less significant in plasticine than metals during FSW, and the Peclet number cannot generally be matched for the two materials. This limits similarity to a more qualitative analysis.

4 Material Flow Measurements

This chapter presents an experimental particle-grid method for quantifying material flow in FSW. The objective of such an analysis is to better characterize the tool/material boundary condition, such as stick/slip as well as characteristic strain and strain-rate values near the tool. This data will be used subsequently to validate a numerical model of FSW. Optical grid methods have been used for several years to determine surface strain and strain-rates in plastic deformation processes [55]. In the grid method, a typically uniform grid pattern is placed on the surface of a component. As the part is placed under load, deformation of the grid is recorded through image processing techniques. A slight variation on this method, along with radiography is applied here to FSW of plasticine at the mid-pin depth. Particle placement in the plasticine is relatively simple compared to metals. The formability of the plasticine makes it possible for the particles to be embedded in the workpiece without gaps between the particle and parent material. A grid pattern can also be easily pressed into the plasticine, which can be observed after FSW.

4.1 Experimental Setup

The plasticine was flattened to a uniform thickness of 14 mm for FSW. A screen with a grid size of 1.5 x 2.0 mm was pressed into the surface of the plasticine (in the *x*-*y* plane shown in Figure 1-1). The screen was then removed, leaving a uniform grid pattern

on the clay. Small spherical steel particles (1.0 mm in diameter) were then positioned within the grid (the grid was used for precise particle placement) as shown in Figure 4-1. Particles were placed in a single line parallel to the tool motion (or streamlines). Single particle streamlines were used to eliminate any confusion of multiple flow paths, which may cross in the pin wake. After positioning the particles, another sheet of plasticine, half the thickness of the pin was placed on top of the piece containing the particles. The two clay pieces were pressed slightly (30-50 kPa) to ensure good contact. Seven samples were processed with the particle lines located at approximately y/r_p = -1.2, -0.86, -0.34, 0, 0.37, 0.90, and 1.4 mm from the centerline, where r_p is the tool pin radius (negative values indicate locations on the retreating side of the tool). An eighth sample, containing only a pressed grid with no particles was also processed. To the extent possible, the top layer of this sample was removed after processing to reveal the distorted mesh away from the processed section (*i.e.*, far field distortion).

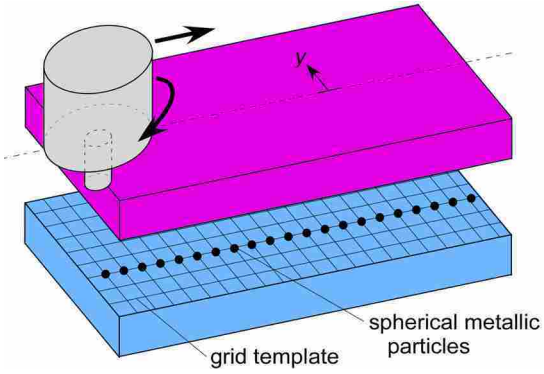

Figure 4-1: Particle and grid setup sketch.

Material deformation sufficiently far from the pin is relatively small, and material motion can be determined solely from the pressed grid. After processing, the top layer of

plasticine ahead and to the sides of the stirred zone can be peeled away from the bottom layer to reveal the deformed grid at the mid-pin depth. Behind the tool, however, the top layer of plasticine becomes fused to the bottom layer and the two pieces cannot be separated. In addition, the grid pattern directly adjacent to the extracted pin location becomes deformed beyond recognition. These effects limit acquisition of information from the deformed grid for the flow far from the pin, and no information can be retrieved downstream of the tool. The usefulness of the grid (without the particles) is that it produces the deformation field away from the pin without the cost of manual particle placement and x-ray imaging.

The workpieces were processed using a tool rotational rate of 250 RPM and a feed-rate of 1.1 mm/s. The tool was also tilted 2.5 degrees. The penetration depth of the tool into the clay was set to a constant value, chosen such that no (or minimal) material was expelled from the FSW zone at the surface (no flash), and no voids behind the tool were apparent. The FSW tool has a 25.4 mm diameter concave shoulder and a smooth concentric pin, 7.3 mm in length with a diameter of 7.7 mm.

Results from Chapter 2 demonstrated that material flow under these operational parameters is relatively simplistic, where material is primarily extruded past the pin and vertical motion is less pronounced. In addition, the selected operational parameters result in general flow features in the plasticine that correspond well with FSW of aluminum. The method used in this study requires identification of individual particles both before and after FSW, and the technique fails if material rotates more than once around the pin. It has been observed that with a threaded pin, the plasticine can become trapped in the threads and forced to the bottom the pin (see Chapter 2). Preliminary stop-action welds

with a threaded pin resulted in particle locations on both the advancing and retreating sides of the pin (*i.e.*, in a rotation region around the tool), as well as at various vertical depths. Similar vertical motion and rotating regions have also been observed in FSW of metals [8]. The smooth pin tool was selected for this study so that individual particles could be clearly identified with respect to their neighbors both before and after welding. It is acknowledged that the existence of a rotational or non-rotational region of material flow around the pin is likely dependent on the material being processed [13].

A stop-action technique, as outlined in previously in Chapter 1, and similar to previous metal studies by Colligan [9] and Guerra et al. [8], was used to suspend the flow of material around the tool. After processing, x-ray images of the six plasticine samples containing the particles were obtained. Images were taken of each particle sample both in the *x-y* (plan view) and the *x-z* (longitudinal) planes. The x-ray photographs allow observation of the steel particles around the pin.

4.2 Particle Field Analysis

The steel particles will follow the flow of material if their inertia is negligible compared to the inertia of the flow. Particle inertia effects can be determined by considering a single particle in the flow. At the extreme case, the stationary particle is instantaneously placed in a flow around the pin where the material is moving at the speed of the pin ($V = r_p\omega$). Newton's second law governs the motion of the particle, where drag is the primary force acting on it. The small size of the particle, along with the extremely large effective viscosity (η) of the plasticine results in a very low Reynolds number flow around the particle. Under such a case, the drag coefficient can be

estimated from Stokes' law ($C_d = 24/Re$) [11]. The velocity of the particle (v) with time is then

$$v(t) = V\left(1 - e^{-t/\tau^*}\right), \tag{4-1}$$

where the time constant $\tau* = d^2\rho_p/18\eta$, d is the particle diameter, and ρ_p is the density of the particle. The particles are steel (ρ_p = 7870 kg/m^3) with a diameter of 1.0 mm. The viscosity of the Van Aken plasticine can be determined from the flow stress and strain-rate according to Peryzna's viscoplasticity model ($\eta = \sigma_f / 3\dot{\bar{\varepsilon}}$) (refer to chapter 6 for a detailed derivation). At relatively high temperatures (330 K) and strain-rates (10 s^{-1}), the effective viscosity is on the order of 1000 Pa s. With a tool rotational speed of 250 RPM, the maximum velocity of the material is 0.1 m/s (assuming full-stick conditions at the pin). Under these conditions, the particle velocity will reach 99% of the FSW material velocity in 0.1 μm (2 μs). This suggests that the steel spheres will closely follow the material flow.

If a reference frame is adopted where material flows toward a stationary tool (which is rotating), then particles well upstream of the tool have a velocity equal to the workpiece feed-rate (f = 1.1 mm/s). The time required for the furthest upstream particle on a streamline to move to the next particle's location is $\Delta t = f/\Delta s_o$, where Δs_o is the initial spacing between the two particles (before FSW). Note that despite care taken to place the particles equidistant from each other, Δs_o varies slightly along a streamline, and therefore, Δt is unique for each particle pair. After FSW, the distance between particles along a streamline is measured and divided by Δt to obtain the magnitude of the local velocity. By definition, the direction of the velocity is tangent to the streamline. Near the pin, the distance between two particles along a streamline can become significantly

larger than the original spacing. In such a case, the streamline is approximated as an arc with a radius equal to the average distance of the two particles from the pin center. The local material velocity is then determined according to Eq. (4-2),

$$v = \frac{\Delta s}{\Delta t} = \frac{(r_m \phi) f}{\Delta s_o}, \tag{4-2}$$

where r_m is the mean distance of two particles from the center of the pin and ϕ is the angle between the two particles. Note that the average velocity between two adjacent particles along a streamline is determined from Eq. (4-2), not the velocity of an individual particle.

Generally, strain-rates can be determined from gradients in the velocity field. However, the coarseness of the particle field, along with large gradients near the pin make accurate spatial differentiation difficult. Instead, strain and strain-rates are calculated based on stretching (or compression) of individual streamlines. If the primary direction of deformation during FSW is along streamlines, then values along the streamline will more accurately reflect the overall effective strain (as opposed to a one-dimensional analysis in the feed direction, for example). The strain, based on stretching of the streamline is,

$$\varepsilon = \frac{\Delta s - \Delta s_o}{\Delta s_o}, \tag{4-3}$$

and the effective strain-rate is defined according to Eq. (4-4)

$$\dot{\varepsilon} = \frac{1}{\Delta t} \frac{\Delta s - \Delta s_u}{\Delta s_u} = \frac{f}{\Delta s_o} \frac{\Delta s - \Delta s_u}{\Delta s_u}. \tag{4-4}$$

In Eqs. (4-3) and (4-4), Δs is the streamwise distance between a pair of adjacent particles after FSW, and Δs_u is the streamwise spacing between a neighboring pair immediately

upstream. Both the strain and strain-rate values are expressed at the geometric midpoint (streamwise) between the two particles.

An automated system for determining the grid intersections proved difficult because there is virtually no contrast between the pressed grid lines and surrounding material. The locations of grid intersection points and particles were therefore determined manually in the digital photographs and x-ray images, respectively.

4.3 Uncertainty Analysis

The uncertainty in the velocity measurement, U_v, is determined by differentiation of Eq. (4-2) with respect to the initial and final particle spacing,

$$U_v^2 \approx \left(\frac{\partial v}{\partial \Delta s_o} U_{\Delta s_o} \right)^2 + \left(\frac{\partial v}{\partial \Delta s} U_{\Delta s} \right)^2, \tag{4-5}$$

where $U_{\Delta s_o}$ and $U_{\Delta s}$ are uncertainties in the initial and final particle spacing, respectively. It can be assumed that the uncertainty in the tool feed-rate is negligible compared to the error in the measured particle spacing.

The largest source of error is the ability of the user to identify the center of the steel particles in the digital images, denoted U_x. Both of the uncertainties on the right-hand-side of Eq. (4-5) are dependent on U_x. By enlarging sections of the digital images, the particles can be located with an accuracy of ±0.1 mm.

For any two points, it can be shown that the uncertainty in the straight-line distance between the points is $U_{\Delta s_o} = \sqrt{2} U_x$. Error in the FSW particle spacing, $U_{\Delta s}$, is approximately equal to $U_{\Delta s_o}$. The derivatives in Eq. (4-5) are readily evaluated, and

given the coordinates of two particles (both before and after processing), the uncertainty in the local velocity can be determined.

The uncertainty in the strain and strain-rate can be determined by differentiation of Eqs. (4-3) and (4-4). The result for the error in strain values is similar to Eq. (4-5) (with strains substituted for velocities). Uncertainty in the strain-rate, however, includes an additional source of error from inaccuracies in measuring the particle spacing in the FSW x-ray image immediately upstream, $U_{\Delta s_u}$ (approximated $U_{\Delta s_u} \approx U_{\Delta s} \approx U_{\Delta s_o}$). (Refer to Appendix B for a more detailed derivation.)

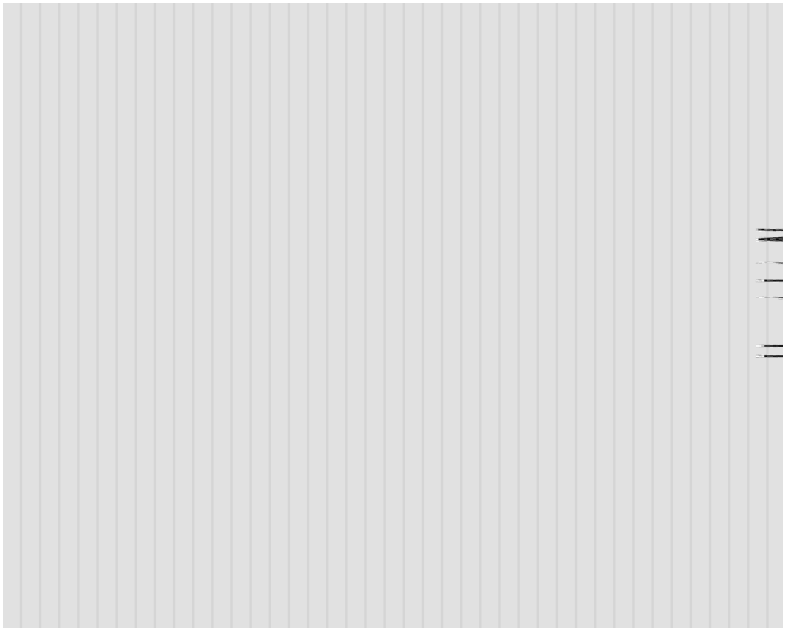

Figure 4-2: Uncertainty in velocity, strain, and strain-rate values as a function of streamwise particle spacing after processing. Both the initial and upstream particle spacing is 2.0 mm.

Assuming an initial particle spacing of 2.0 mm and a feed-rate of 1.1 mm/s, U_v and U_ε are dependent on Δs only. The strain-rate error, however, remains a function of both Δs and Δs_u. Figure 4-2 shows the uncertainty in the velocity, strain, and strain-rate

as a function of the FSW particle spacing. When velocities are significantly lower than the feed-rate, corresponding to $\Delta s/\Delta s_o < 1$, U_v becomes large. Similarly, the error is also large as the strain and strain-rate approach zero, corresponding to $\Delta s/\Delta s_o = 1$ ($v = f$) in the figure. The uncertainty analysis reveals that the method used in analyzing the digital images is not accurate for small deformation processes. However, if the deformation is sufficiently large (in either compression $\Delta s/\Delta s_o \lesssim 0.9$, or tension $\Delta s/\Delta s_o \gtrsim 1.1$), then the error in both the strain and velocity is less than 10%. In Figure 4-2, the strain-rate has been evaluated assuming that $\Delta s_u = \Delta s_o$. Typical values observed in this work range from $0 < \Delta s/\Delta s_o < 5.4$, and aside from lower limit of vanishing velocity, strain, and strain-rate values, uncertainty is between 5 to 15%. Of course, as $\Delta s/\Delta s_o \rightarrow 0$, there is no material deformation and the velocity is equal to the feed-rate. It should be noted, however, that this window of $\Delta s/\Delta s_o$ corresponding to 10% uncertainty decreases modestly as Δs_u decreases (not shown in the plot).

4.4 Results and Discussion

Deformation away from the processed section is observable from the deformed grid (no inserted particles) in Figure 4-3. Recall that after processing, the top layer of material can be peeled away from the bottom layer to reveal the pressed grid pattern wherever sufficient bonding has not occurred. This process reveals not only some of the deformation away from the weld, but it also shows that only a relatively small area of material is joined (for a lap weld with the interface at the mid-pin depth). The figure shows that bonding only occurs over an area from the retreating edge of the pin to a distance of approximately one pin radius from the advancing edge of the pin. Additionally, a void can be seen at the back advancing side of the pin in the cyan colored

material. This void has also been observed in welded sections of a single layer of plasticine, and therefore it is not a result of a discontinuity between the two layers.

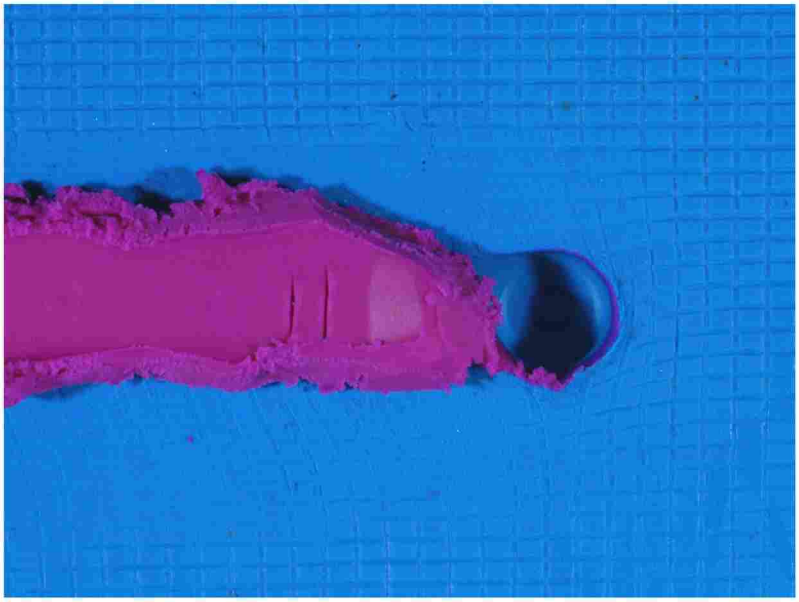

Figure 4-3: Deformed grid from FSW processed workpiece.

Steel particles and x-ray imaging must be used in areas where the two layers of plasticine cannot be removed without damaging the grid pattern. Figure 4-4 shows both plan and longitudinal x-ray images of several particle streamlines with locations expressed as a fraction of the pin radius, y/r_p. The coordinate y is measured relative to the centerline, where positive values indicate the advancing side. In some of the images (*i.e.*, Figure 4-4d) a small void is observed at the back advancing side of the pin. The void persists from the bottom of the pin to approximately the mid-pin depth, but is closed at a short distance downstream of the pin. Though the void is not clearly visible in all of the images, it was observed in all of the welds. The figure shows that for particle lines originating at the advancing side of the centerline, the spacing between particles

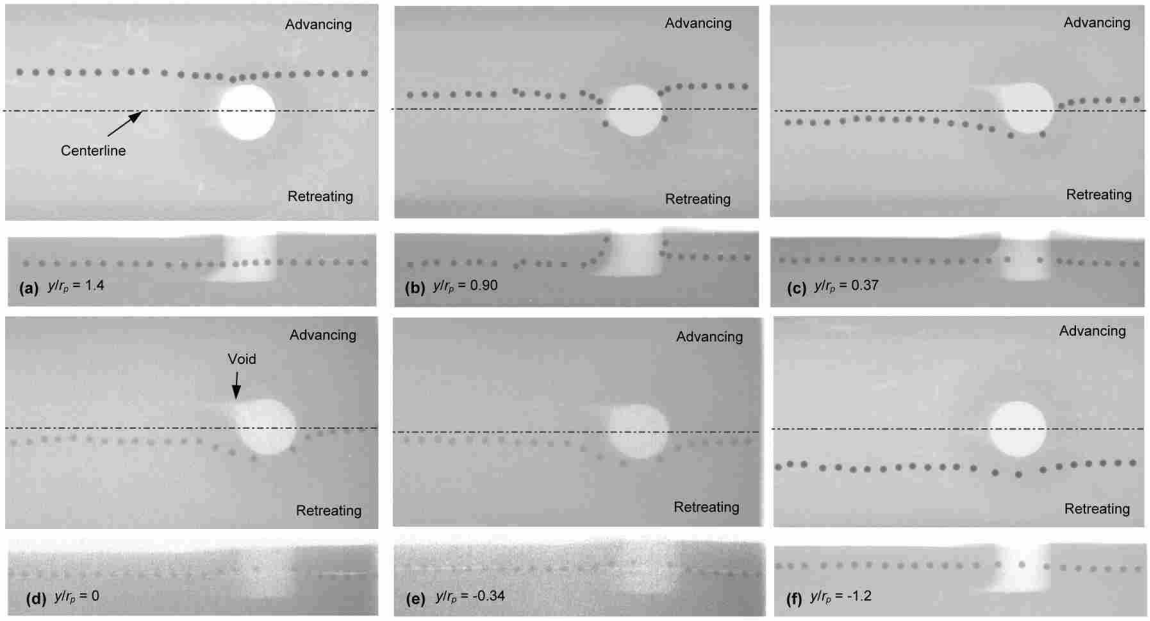

Figure 4-4: Steel particle radiograph plan (*x-y* plane) and longitudinal views (*x-z* plane).

decreases at the front of the pin, but significant stretching occurs as material moves around the retreating side of the pin. For particle lines initially at the retreating side no compression region is observed at the front of the pin, and relatively little stretching is evident. Behind the tool, the particles return to approximately their initial spacing for all cases. Note, however, that the particle streamline behind the pin in Figure 4-4b is more chaotic, as evidenced by a more non-uniform particle spacing. Although the spacing is not uniform, the average spacing of the particles behind the tool in this streamline is approximately equal to the initial spacing. This chaotic flow is attributed to both slipping of the material against the pin and substantial vertical motion, which is apparent in the side view image in Figure 4-4b. This streamline of particles is initially at $y/r_p = 0.90$. As the particles along $y/r_p = 0.90$ move around the pin, they also flow vertically upward toward the shoulder. Immediately behind the pin, these particles move down to a final position below their initial depth, filling the trailing edge pin void. Particles in this

streamline also return to their initial transverse location behind the tool (relative to the centerline). It is interesting that no other particle lines experience any significant vertical motion. Even at a short distance from this streamline (y/r_p = 1.4 and y/r_p = 0.37) vertical motion is very minimal. The lack of upward motion results in deposition at the retreating side of the pin, except for particles initially at y/r_p = 1.4, where they always remain at the advancing side of the pin. To summarize, at the mid-pin depth, it appears that there is a small region near y/r_p = 0.90 where material is lifted to nearly the shoulder, flows around the retreating side of the pin and is forced downward at the back advancing side of the pin. If material is not lifted closer to the shoulder, it simply extrudes around the pin and is deposited at the retreating side of the centerline.

Each of the welds shown in Figure 4-4 were conducted such that no or very minimal flash was expelled during processing. Some experiments were also performed with a small amount of flash by increasing the tool depth by 1 mm. Obviously, if the particle depth below the workpiece surface is fixed, then increasing the tool depth results in particle lines slightly closer to the shoulder, but it also may have some effect on the friction boundary condition at the tool/material interface due to higher vertical forces. X-ray images from these welds are provided in Figure 4-5. Even with the higher tool depth, a void still appears at the bottom advancing side of the pin (Figure 4-5b). Generally, the figure shows significantly more vertical motion compared to Figure 4-4 and a much more chaotic flow. In Figure 4-5a particles move upward and appear to contact the shoulder. These particles cluster at the back advancing edge of the pin (after rotating around the retreating side of the pin) and the spacing of the particles behind the pin is highly irregular. This irregular deposition suggests that particles are deposited intermittently,

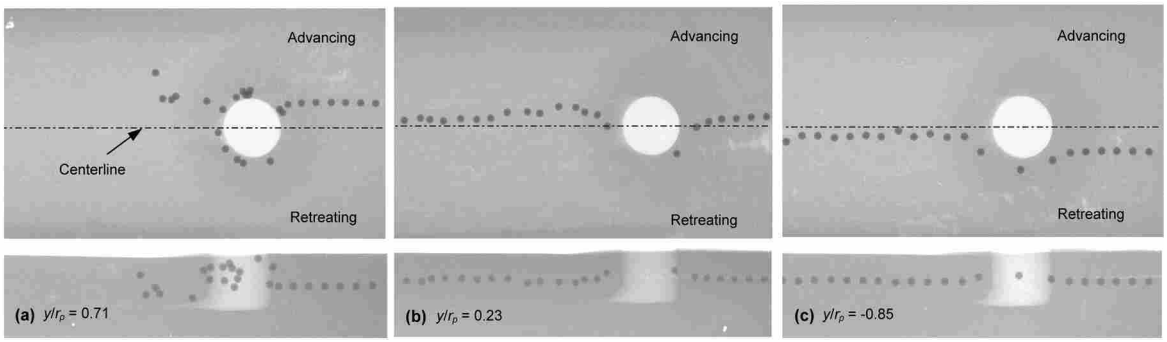

Figure 4-5: Steel particle radiograph plan (*x-y* plane) and longitudinal views (*x-z* plane) at increasing tool depth.

perhaps due to a sticking/slipping boundary condition. However, the reason for intermittent deposition cannot be explained by this particle study. In all cases, particles that begin at the advancing side of the centerline (Figure 4-5a-b) show significant vertical motion as they move around the retreating side of the pin and are deposited at the advancing side of the pin very near their initial transverse location. This behavior is in contrast to the shallower depth where only material near y/r_p = 0.90 exhibits such behavior. Material initially at the retreating side of the pin (Figure 4-5c) shows virtually no vertical motion and simple extrusion around the pin. The clustering and irregular deposition of particles prohibits calculation of velocity and strain/strain-rate values since each particle must be uniquely identified. Therefore, further FSW experiments with the particles at increased tool depth were abandoned.

Streamlines from particle radiographs (no-flash welds from Figure 4-4) and grid intersection points (Figure 4-3) are shown in Figure 4-6. All streamlines in the figure begin at the same approximate distance upstream of the pin. In addition, every streamline in the figure consists of 20 particles, and thus, the final location of the last particle (downstream of the pin) in a particular streamline can be compared relative to the

termination point of other streamlines. The last particle in all streamlines in Figure 4-6 has been connected with a dashed curve. This curve illustrates the post-processing deformation of a line of material that is initially straight (shown as the dashed vertical line upstream of the tool) before FSW. The shape of the downstream curve compares well with flow visualization studies previously conducted in metals [7] and plasticine experiments in Chapter 2 (Figure 2-11). The formation of the curve is a result of material elongation along streamlines initially located at approximately $y/r_p < 1$, along with compression of advancing side streamlines near the pin that do not rotate around the retreating side of the pin.

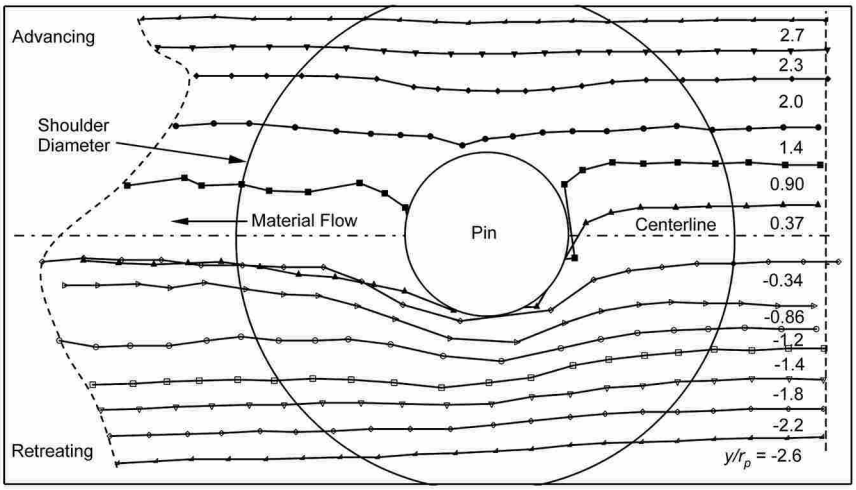

Figure 4-6: Flow lines and final positions of particles and grid line intersections at mid-pin depth.

Another interesting observation from the figure is the significant difference in behavior of the streamlines initially at $y/r_p = 0.90$ and $y/r_p = 1.4$. At some location between these two streamlines the flow must stagnate at the pin. At this location, material is bifurcated and some of the workpiece travels past the advancing side of the

pin, while the remainder flows around the retreating side of the pin. The material that travels past the tool at the advancing side experiences compression, evidenced by the shorter total travel, while material that rotates around the pin is in tension and undergoes extreme plastic deformation.

Figure 4-6 also reveals that particles from the two streamlines straddling the centerline (y/r_p = 0.37 and –0.34) merge downstream of the tool, and are deposited on the retreating side at a nearly identical transverse location. This is a result of minor differenced in the tool depth during welding of the two particle streamlines. As stated previously, the tool depth for the data of Figure 4-6 was such that no material was expelled from the surface of the plasticine workpiece (*i.e.*, no flash). Flash generation was found to have little effect on streamlines originating on the retreating side of the centerline. However, these additional experiments revealed, in contrast to the no-flash data of Figure 4-6, that all streamlines initially on the advancing side were deposited on the advancing side when tool depth was set such that flash was produced (including the streamline initially at y/r_p = 0.37). The deposition of particles along these streamlines was significantly more irregular than under no-flash conditions. As a result, the sequential order of particles along streamlines behind the tool could not be determined.

Given the FSW particle locations as shown in Figure 4-6, local velocities can be determined from Eq. (4-2). Figure 4-7 is the resulting velocity vector field at the mid-pin depth. The magnitudes of the vectors both far ahead of and far behind the tool are nearly identical, and are equal to the material feed-rate. Note that downstream of the tool, the particle spacing in the feed direction of the streamline initially at y/r_p = 0.90 (see Figure 4-6) has been averaged to eliminate unrealistic values due to the irregular nature of the

material flow. The average spacing of these particles is within 3.5% of the initial particle spacing, resulting in a material velocity approximately equal to the feed-rate. The transverse locations of the downstream particles for this streamline are also averaged.

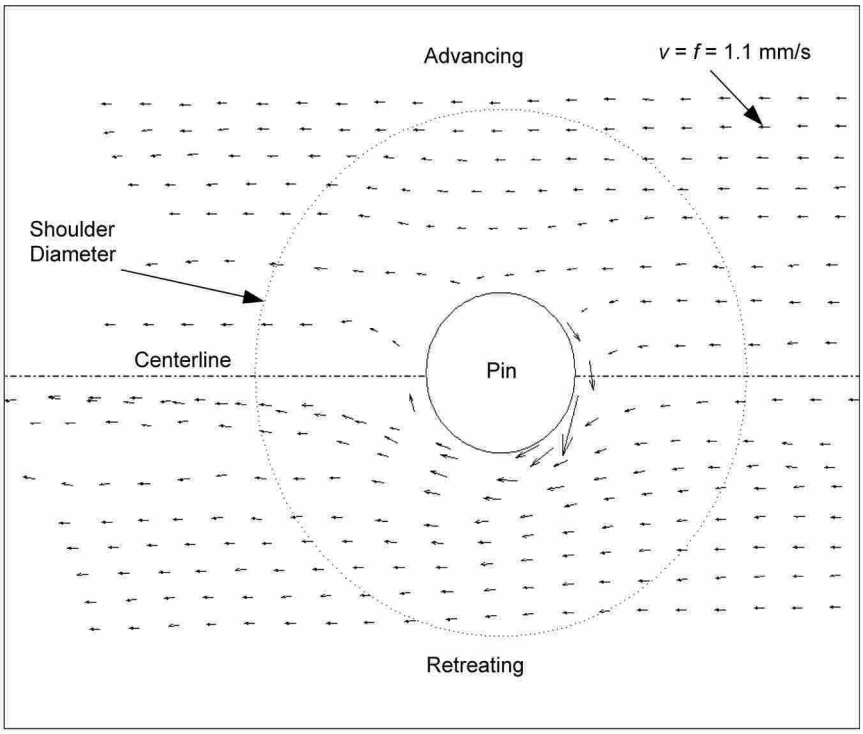

Figure 4-7: Velocity vectors from final particle locations and grid line intersections.

Generally, velocities are lower than the feed-rate as material approaches the pin at the advancing side. However, velocities increase to several times that of the feed-rate as material flows around the leading and retreating sides of the pin. Behind the pin, at the retreating side, the velocity returns to the material feed-rate.

Velocity profiles normalized by the surface speed of the pin are shown in more detail in Figure 4-8 for several streamlines that are significantly affected by the pin. The

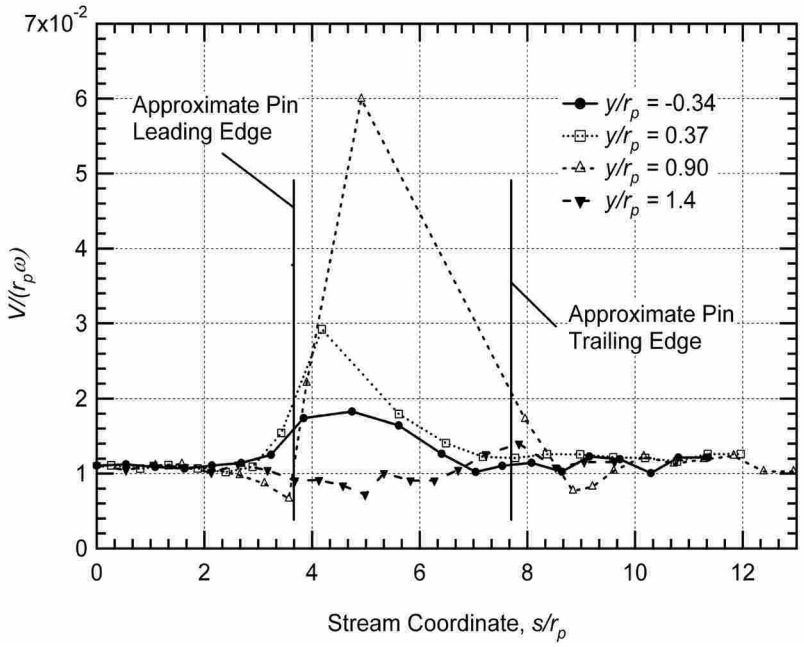

Figure 4-8: Dimensionless velocity profiles along the stream coordinate for several streamlines near the pin (y/r_p is the initial particle position relative to the centerline).

velocity profiles are plotted along the stream coordinate normalized by the pin radius, s/r_p. The stream coordinate is set arbitrarily to zero at the first upstream particle location, and follows the particular streamline. Particle lines initially located closest to the centerline show an increase in velocity from the feed-rate to 1.8 - 2.9% of the tangential pin velocity as they pass the retreating side of the pin. The furthest streamline to the advancing side of the centerline (y/r_p = 1.4) does not flow around the retreating side of the tool. Rather, particles on this streamline slow slightly as they are extruded past the advancing side of the pin. Toward the back of the pin, the particle velocity on this streamline returns to the feed-rate. Particles initially at y/r_p = 0.90 also show a slight reduction in velocity as they approach the pin. However, particles on this streamline contact the pin, and as a result, their velocity increases rapidly as they move around the retreating side of the pin. The largest velocity experienced by the material in contact with

the pin is only 6.0 ± 0.4% of the pin speed. Behind the pin, particles along this streamline slow to a velocity below the feed-rate as material fills the trailing edge pin void.

The velocity of material in contact with the pin is lower than previous reports by Guerra *et al.* [8] for Al 6061 where material sticks to the tool. However, the data are more comparative to results from Schmidt *et al*. [10] for Al 2024 where material velocities are estimated at 10 to 30 percent of the tool speed in the transition zone very near the pin. While it is difficult to directly relate the plasticine velocity to a particular metal, plasticine/metal similarity, as discussed in Chapter 3, permits the general extrapolation that slip may be substantial at high weld pitch (tool feed per revolution). The plasticine experiments in this study illustrate an extreme case with respect to tool/material slip, and it is recognized that this boundary condition is likely dependent on the process material and operating parameters. For example, as the rotational speed of the tool approaches zero (weld pitch approaching infinity), the process becomes one of simple extrusion around a cylinder and slip at the sides of the cylinder is expected. At the other extreme, Gerlich *et al*. [13] have shown that Al 7075 and 2024 experience substantial slip with a threaded pin tool during friction stir spot welding (a weld pitch of zero), and a no-slip condition was observed in Al 6061 and 5754.

Strain profiles along several streamlines calculated from Eq. (4-3) are plotted in Figure 4-9. Note that according to Eq. (4-3) and Figure 4-2, the uncertainty in the strain measurement can be as large as 20-30% for $|\varepsilon| < 0.3$. The largest strains occur along streamlines originating at the advancing side of the centerline. Specifically, the streamline initially at $y/r_p = 0.90$ experiences the greatest strain as it flows around the

retreating side of the pin. Material along this streamline experiences an average strain of 4.4 ± 0.3 (tension) as it deforms around the pin. To the author's knowledge, experimental data on material strain in FSW have not been presented for any working material. However, this value is comparable with analytical values estimated by Heurtier *et al.* [38] for aluminum.

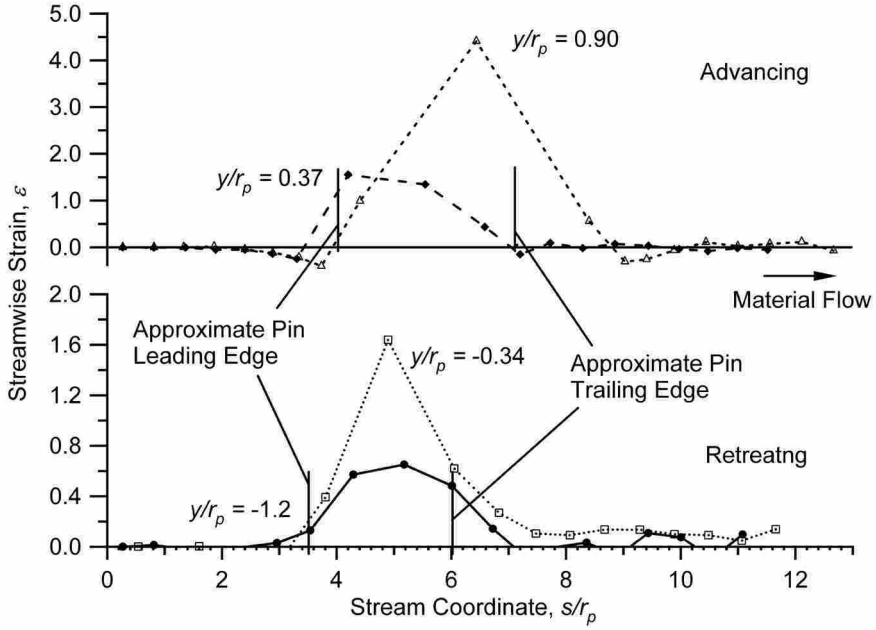

Figure 4-9: Streamwise strain profiles along the stream coordinate for both advancing and retreating side streamlines near the pin.

Figure 4-9 reveals that generally, material is compressed as it approaches the leading-edge of the pin. Both streamlines at the advancing side of the centerline are compressed to a strain of nearly -0.5 as they approach the pin. (Note that according to Eq. (4-3), strain values range from -1 in compression to $+\infty$ in tension.) The material then experiences positive strain (relative to initial lengths) as it moves around the retreating side of the pin. The material is re-compressed to its initial condition toward the

back of the pin; downstream of the tool, the streamwise strain is essentially zero for all streamlines. In fact, the average particle spacing downstream of the tool must return to the initial spacing if the feed-rate is to be recovered according to Eq. (4-2).

Although the streamwise strain downstream of the tool vanishes, a finite strain transverse to the feed direction remains in the material after FSW. Referring to Figure 4-6, material between streamlines $y/r_p = -0.34$ and $y/r_p = 0.37$ is compressed laterally as it flows past the retreating side of the pin. An overall transverse strain can be estimated by measuring the initial and final spacing between two adjacent streamlines. Material between the two streamlines that initially straddle the centerline is compressed laterally to a strain approaching $\varepsilon = -1$, *i.e.*, the spacing between the two streamlines essentially vanishes downstream of the tool. At the other extreme, material between $y/r_p = 0.37$ and $y/r_p = 0.90$ is stretched in the transverse direction behind the pin to approximately twice the initial spacing of these two streamlines, corresponding to $\varepsilon \approx 1$.

Strain-rates along streamlines as calculated according to Eq. (4-4) are plotted in Figure 4-10. Values approaching zero contain the largest uncertainty, where from Eq. (4-4) and Figure 4-2, the error in strain-rate can be as large as 20-30% for strain-rates less than approximately 0.1 s^{-1}. The largest strain-rate for both streamlines at the advancing side of the centerline is 1.2 ± 0.2 s^{-1}. This strain-rate prevails over a longer streamwise distance along the streamline $y/r_p = 0.90$ compared to the other advancing side streamlines. Strain-rates at the retreating side are approximately half those on the advancing side. As expected, the average strain-rate downstream of the tool is approximately zero for all streamlines.

Given the tool's tangential speed (100 mm/s) and an estimated deformation zone thickness of 1 mm at the retreating side of the tool, strain-rates on the order of 100 s^{-1}

would be expected if a no-slip condition prevailed. The low values determined from the plasticine model support a slipping condition. Although experimental FSW strain-rate data are limited, strain-rate values calculated using the Zener-Hollomon parameter have been presented for both FSW [14] and friction stir spot welding [12, 13]. For some alloys (5754 and 6061) the material sticks to the tool and strain-rates are large [13]. However, strain-rates reported for other alloys (2024, 6082, 7075, and 7108) indicate substantial slip with strain-rate values as low as 1.6 s^{-1} during FSW [14] and 20 s^{-1} for friction stir spot welding [13].

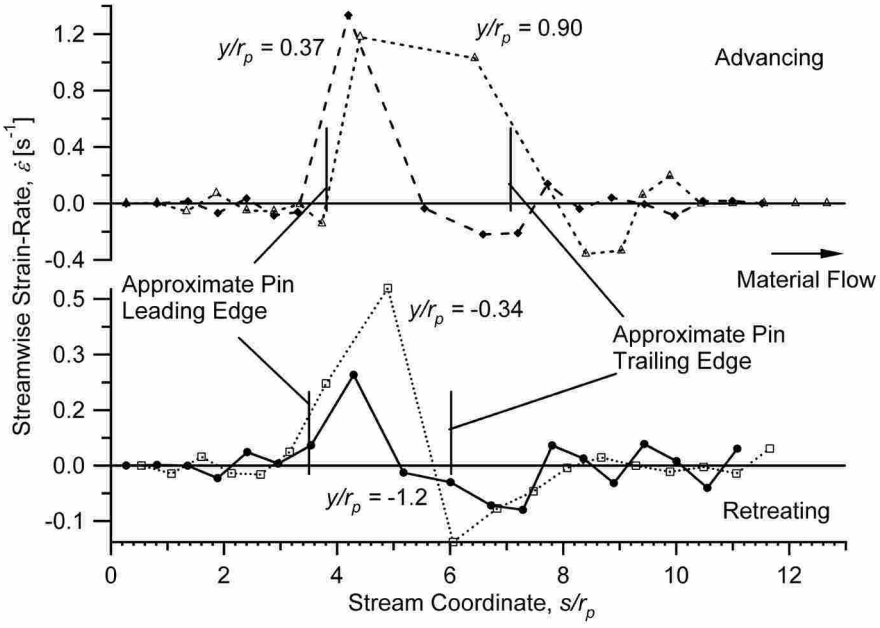

Figure 4-10: Streamwise strain-rate profiles along the stream coordinate for both advancing and retreating side streamlines near the pin.

From this study it is concluded that there is substantial slip at the tool/material interface. The largest velocity of material originating at the mid-pin depth was determined to be only 6.0% of the pin speed. Material that contacts the pin during

processing experiences strains as large as 4.4 and a strain-rate of 1.3 s^{-1}. Generally, material at the mid-pin depth simply extrudes around the pin and does not rotate with the tool. Also, significant material lifting is observed as particles extrude around the retreating side of the pin. These results are applicable for welds using an unthreaded smooth pin at welding depth corresponding to no flash conditions. If the tool depth is increased such that flash is generated, particles were observed to rotate with the pin and a more chaotic flow ensued.

5 Material Flow Visualizations

Although significant research has been presented concerning material flow at the tool in FSW of metals, each study primarily presents variations in one or two different materials, tools, and/or operating parameters, sacrificing the broader picture. In addition, the true three-dimensional character of the flow is often under-represented due to limited material marker arrangements or flow interrogation methods. As stated previously, the ability to arrange multiple contrasting colors of plasticine, which have nearly identical physical properties, in various orientations makes non-intrusive three-dimensional study possible (and at low cost). The intent of this portion of the study is to provide a more complete and clear picture of material flow *regimes* in FSW. Through multiple marker setup arrangements, this work presents a detailed three-dimensional assessment of material flow around the tool under various operating conditions.

It is recognized that material flow in FSW can vary between different metals, tooling, and operating conditions, and hence, studies with plasticine are designed to illustrate relatively extreme cases. Specifically, differences in FSW material flow features at both high and low tool rotational speeds, increasing tool down force (or tool plunge depth), and a threaded versus a smooth (no thread) tool pin are presented. In addition, stop-action, along with variously oriented marker material is used such that material motion around the tool can be examined in vertical, transverse, and longitudinal directions. A systematic study of each of these scenarios permits a "cause and effect"

analysis of tool rotational rate, material flow with and without flash generation, and the consequence of pin threads.

5.1 Experimental Setup

The Van Aken plasticine as described in Chapter 3 is used throughout this study. Cyan and magenta colors were chosen for their contrast and physical/mechanical property similarities as noted in Chapter 2. These two colors of plasticine were arranged in five different configurations in the process workpiece such that visualization of material flow in all spatial directions could be examined. Each workpiece setup is shown schematically in Figure 5-1. The five configurations are designated as:

i. *Streamline Configuration* (transverse cross-section shown in Figure 5-1a). This configuration consists of four thin vertical layers of alternating cyan and magenta plasticine. Each vertical layer is 2.7 mm thick and runs the length of the workpiece. Two of the layers are on the advancing side of the centerline and two are on the retreating side. Each vertical layer essentially acts as a streamline (or pathline) of the flow.

ii. *Lap Configuration* (transverse cross-section shown in Figure 5-1b). Here, a single thin horizontal layer of cyan plasticine is stacked on top of a layer of magenta. The top and bottom layers of the Lap Configuration are 3.5 mm (approximately half the length of the pin) and 14 mm thick, respectively. This configuration permits visualization of the extent of vertical motion.

iii. *Staggered Lap Configuration* (transverse cross-section shown in Figure 5-1c). This configuration is comprised of three horizontal layers with contrasting colors arranged in an alternating pattern on either side of the

centerline. The top two layers in Figure 5-1c are each 2.5 mm thick and the bottom layer is 14 mm thick. The alternating pattern allows simultaneous observation of vertical and transverse motion.

iv. *Longitudinal Configuration* (longitudinal section, x-z plane in Figure 1-1, shown in Figure 5-1d). With this setup, the tool initially processes only cyan material. As the tool advances in the cyan material it suddenly encounters the magenta plasticine. This configuration allows for observation of any trapped cyan material that travels forward with the tool into the magenta colored plasticine.

v. *Butt Configuration* (transverse cross-section shown in Figure 5-1d). This setup consists of cyan colored plasticine at the advancing side of the centerline and magenta at the retreating side. Though it doesn't allow for the more detailed information as with the Streamline Configuration, the Butt Configuration is typical in FSW and it is presented here for purposes of analyzing joining between the two sides of a weld.

All plasticine workpieces were processed on a retrofitted Kearney & Trecker knee mill with PLC/PC control and data acquisition system. Both a smooth and threaded pin tool were used for FSW of the plasticine as shown in Figure 2-1. A single feed rate of 1.1 mm/s was used throughout the study with tool rotational speeds of 250 or 1000 rpm (weld pitch of 0.26 and 0.07 mm/rotation, respectively). These parameters were selected to reveal material flow under general extrusion type behavior in FSW with minimal mixing and rotation with the tool, as well as material flow with extensive rotation with the tool and large macroscopically mixing/stirred regions of material. Rotation of the threaded tool was such that material inside the threads was forced down. The tool was

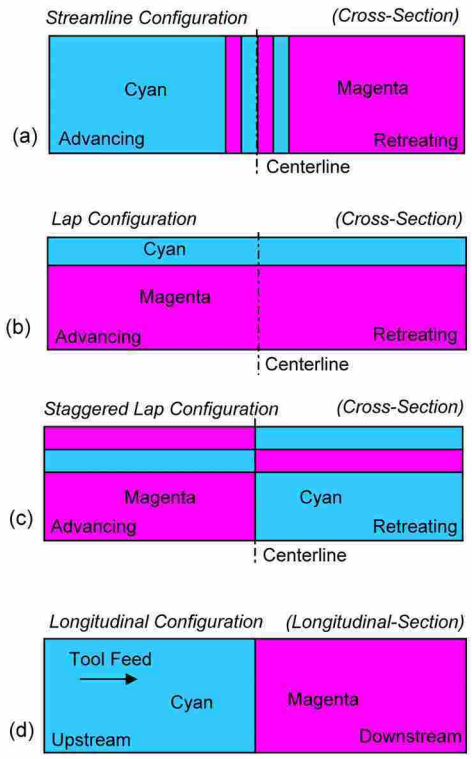

Figure 5-1: Plasticine marker setup sketch: a) Streamline Configuration cross-section, b) Lap Configuration cross-section, c) Staggered Lap Configuration cross-section, and d) Longitudinal Configuration longitudinal section.

tilted backward 2.5 degrees during welding. In addition, two different vertical plunge depths of the tool were investigated. One depth was controlled such that no material was expelled from the weld, which is referred to here as the "no-flash depth." A second, slightly deeper tool depth was also used. A small amount of material was expelled from the processed zone at the deeper tool depth condition, designated the "flash depth." Both tool depths were dependent on the tool pin type (threaded or non-threaded) and rotational rate. Generally, the difference between no-flash and flash tool depths for a given tool and rotational rate was only 0.3 – 0.4 mm. At the end of each weld, the forward motion of the tool was nearly instantaneously suspended and the tool raised from the workpiece.

As explained previously, this technique essentially stops the flow of material around the tool (except for any material inside the threads, which is extracted with the tool).

All five cyan/magenta workpiece configurations shown in Figure 5-1 were processed using both the threaded and smooth pin tools at 250 and 1000 rpm. In addition, each setup was conducted both with and without flash at 1000 rpm. Recall that depending on tool depth, some differences in deformation patterns were observed in Chapter 4 from embedded particles at a tool rotational rate of 250 rpm and with a smooth pin. However, these differences are relatively minor compared to the overall general flow. Also, experiments with contrasting colors of plasticine, as explained in Chapter 2, show only minor differences between butt welds with and without flash generation at 250 rpm for both the smooth and threaded pin tool. Therefore, the consequence of increasing tool depth is only investigated in detail at 1000 rpm. To ensure repeatability, several of the welds were successfully replicated, showing nearly identical material flow patterns. After FSW, the plasticine was sectioned using a 0.3 mm diameter steel wire to reveal material flow features from the contrasting clay colors.

5.2 Results and Discussion

5.2.1 Smooth Pin – 250 RPM

Material flow around the smooth pin tool rotating at 250 rpm is shown in Figure 5-2. The depth of the tool was such that no flash was generated at the shoulder. The figure includes: a) a section from the centerline of the Longitudinal Configuration, b) cross-section of the Longitudinal Configuration 10 mm forward of the initial cyan/magenta interface, c) a horizontal slice at the mid-pin depth from the Streamline

Configuration, d) several transverse (*y-z* plane) sections from the Streamline Configuration, e) several transverse sections from the Lap Configuration, and f) multiple transverse sections from the Staggered Lap Configuration. Each cross-section in images d-f are identified as to its location relative to the extracted tool location, including the pin leading edge (Pin L.E.), center of the pin (Mid-Pin), trailing edge of pin (Pin T.E.), and the fully processed (F.P.) weld downstream of the tool. The arrangement of the images in Figure 5-2 is repeated for each operating condition in subsequent figures as explained in the section above.

Under the welding conditions in Figure 5-2, material simply extrudes around the tool and does not rotate with the pin, except directly under the shoulder. Figure 5-2a is a photograph from a section along the centerline of the welded Longitudinal Configuration. The tool progression was from left-to-right and was extracted well to the right of the image. As the shoulder encountered the cyan/magenta interface, a significant amount of magenta material was swept behind the tool. Aside from the thin region directly under the tool shoulder (at the top of the photograph) and pin tip, little of the cyan material is observed downstream (to the right) of the interface at the centerline of the weld. However, some material became trapped in a rotating region under the shoulder and was expelled at the advancing side of weld as shown in Figure 5-2b. This image is a section of the weld transverse to the welding direction at a location of approximately 10 mm forward of the initial interface line. At the advancing side, a mixture of cyan and magenta material is evident from the upper portion of the weld to the bottom of the pin. This mixed material at the advancing side persists for about 2 shoulder diameters past the

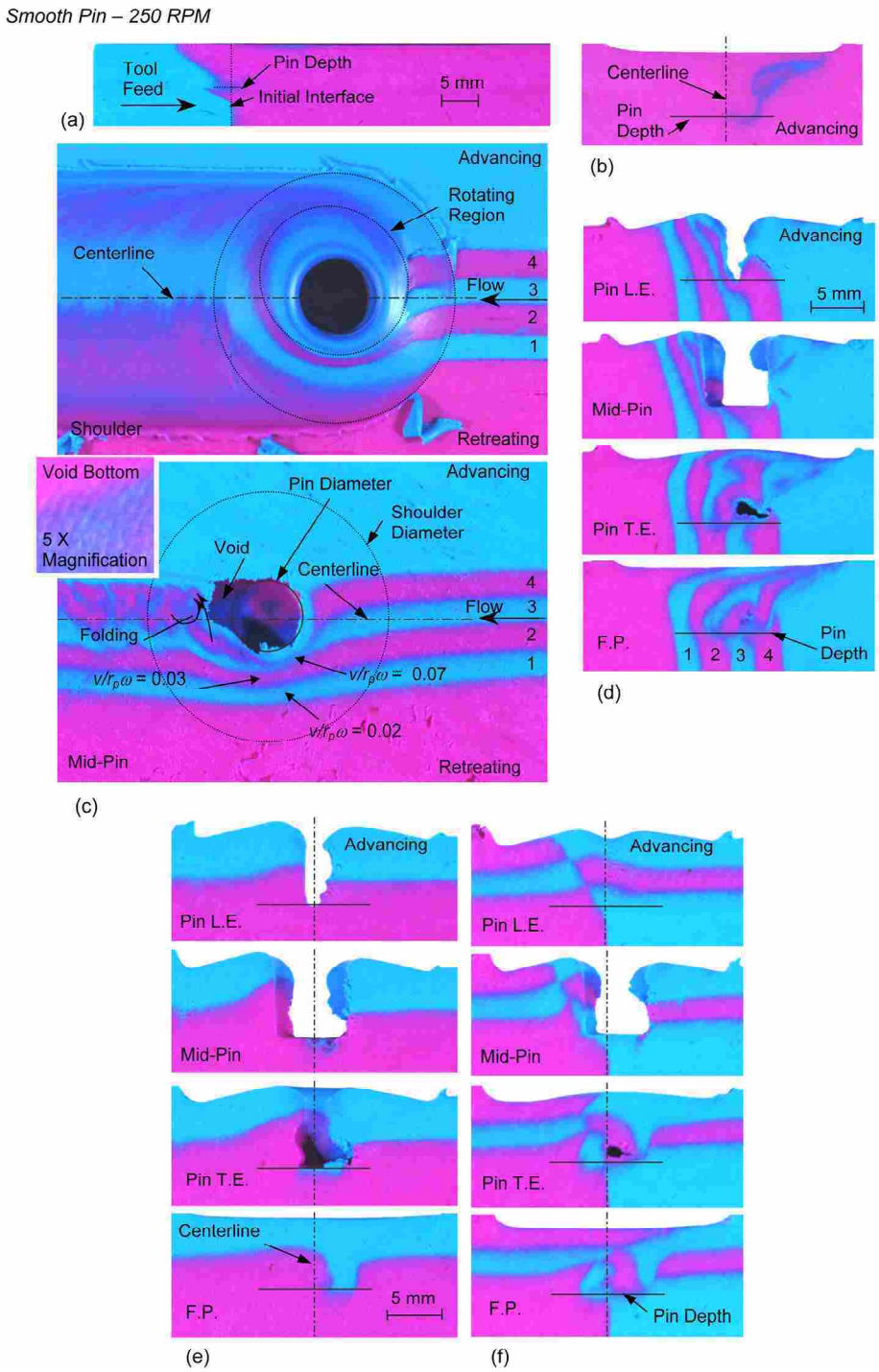

Figure 5-2: Processed plasticine using the smooth pin tool with a rotational speed of 250 rpm (1.1 mm/s feed rate): a) Longitudinal Configuration cut along the centerline, b) Longitudinal Configuration cross-section 10 mm forward of cyan/magenta interface, c) Streamline Configuration at the surface and mid-pin depth, and cross-sections at several longitudinal locations for the d) Streamline Configuration, e) Lap Configuration, and f) Staggered Lap Configuration.

initial interface. It will be shown later that this mixed material originated near the shoulder and was subsequently forced to the lower part of the weld at the back of the shoulder.

Figure 5-3 shows separate welds of the longitudinal configuration with the tool motion suspended at different locations as the tool moves through the cyan/magenta interface. Notice that as the pin approaches the interface, the magenta material is compressed forward (Figure 5-3a, Mid-Pin). At the surface the magenta material is swirling around the pin and some cyan material becomes trapped in a rotating region near the pin.

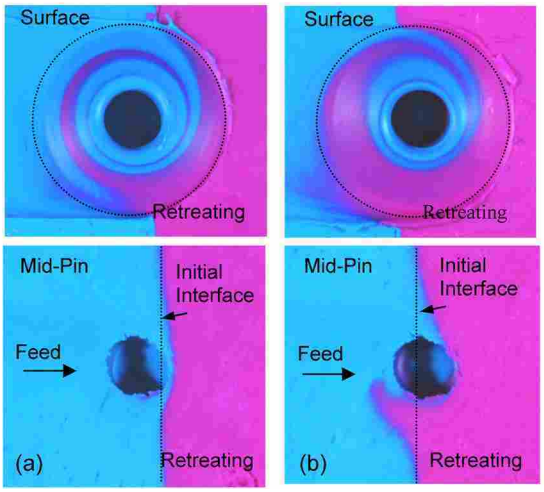

Figure 5-3: Plan view sections of the Longitudinal Configuration at the surface and mid-pin depth with stop action occurring a) as the smooth pin just contacts the initial interface between the cyan and magenta plasticine colors, and b) as the pin penetrates the interface.

Figure 5-2c is a horizontal section of the Streamline Configuration at the weld surface (top photograph) and mid-pin depth (bottom photograph). Contrasting cyan and magenta layers of plasticine are arranged such that four streamlines of the flow are

observed. Each streamline is given a number designation from 1 to 4 as shown in the figure. The hole in the center of the figure corresponds to the extracted pin location.

At the weld surface, the four streamline markers show relatively little deformation under the leading edge of the shoulder. Nearer the pin, however, an eccentric region of rotating material is apparent, which covers streamlines 3 and 4. The approximate size and shape of the rotating region is outlined in the figure. It appears that the rotating region is largest at the advancing side of the weld. The mixed cyan and magenta material is expelled from the shoulder cavity at the advancing side of the weld.

Although stirring and mixing of material at the shoulder is apparent, this behavior is not observed at the mid-pin depth. At this depth, material simply extrudes around the pin and does not rotate with the tool. However, upstream of the pin the streamline markers show significantly more movement toward the retreating side of the tool than at the shoulder. Motion around the pin begins approximately two pin diameters upstream. This deformation well ahead of the pin is unexpected and may be due to minimal variation in the plasticine flow stress at the mid-pin depth. If material near the pin were significantly softer than that in the far-field, this softer material would be unable to transmit the force necessary to cause deformation in the far-field ahead of the pin. Although the material temperature increases by a few degrees (see Chapter 2) due to direct friction and deformation heating as it approaches the pin, the velocity gradients and corresponding strain-rate also increases in this region. Equation (3-6) suggests that a small increase in temperature and a moderate increase in strain-rate have a counter-balancing effect on the plasticine flow stress, supporting the suggestion that there may be minimal flow stress variation between material near the leading edge of the pin and that

in the far-field. On the other hand, a reduction in the flow stress due to higher temperatures directly under the shoulder outweighs any increase due to higher strain-rates. Therefore, this relatively hot flowing material in the rotating region at the shoulder likely has a significantly lower flow stress than surrounding material, and hence, cannot transmit forces necessary to significantly deform material outside the rotating region.

It is noted, however, that the extent of deformation upstream of the pin depends on operational parameters, since other material flow visualization studies presented below, similar to Figure 5-2, show that deformation of the plasticine begins much closer to the pin at higher rotational speeds. Work by Bochniak and Korbel [56] has shown that plastic deformation of aluminum in a die extrusion process begins well upstream of the die contraction, and rotating the die causes deformation to begin closer to the contraction. In the limiting case, as the weld pitch approaches infinity (no tool rotation), it is likely that material deformation would begin well upstream of the tool, consistent with this die extrusion process.

Material in contact with the pin at the mid-pin depth in Figure 5-2c is primarily the cyan plasticine at the far advancing (above streamline 4) side of the pin. Streamline 4 flows in a clockwise direction around the material that contacts the pin. It appears that the stagnation point of the flow (where material is bifurcated) is well to the advancing edge of the pin. As material moves around the retreating side of the pin, the streamline markers become thinner, and then expand at the trailing edge of the pin (see, for example, streamline 3). This behavior is due to an increase in velocity as the material flows more rapidly around the pin, then slows to the nominal workpiece feed rate behind the pin. From conservation of mass, velocities at certain points can be estimated by measuring the

width of a particular streamline at various locations. The maximum velocities thus estimated for each streamline are identified in the figure. The highest velocity is approximately 7% (±1%) of the pin surface tangential speed ($v/r_p\omega = 0.07$), and hence significant slip occurs between the tool and material. Recall that the velocity measurement from the x-ray analysis in Chapter 4 was 6%. Behind the pin, the advancing side markers appear as large irregular alternating layers of cyan and magenta material transverse to the flow direction. In the figure it appears that material around streamline 4 folds together at the back of the pin. For example, streamline 4 thins considerably (increase in velocity) as it extrudes past the retreating side of the pin. At the back of the pin however, material slows to the feed rate and the width of the streamline widens considerably. The cyan material in contact with the pin, however, is still traveling at a relatively high speed and flows past the "stagnating" streamline 4. Slightly further downstream of the pin, the pooled area of streamline 4 behind the pin is forced toward the advancing side of the centerline by the trailing edge of the shoulder. As streamline 4 moves toward the advancing side it traps the cyan material that was in contact with the pin. Additionally, some material from streamline 3 is pulled into streamline 4 as it folds under the trailing edge of the shoulder.

Formation of the apparent folded layers of cyan and magenta plasticine behind the pin may also be complicated due to variations in the slipping boundary condition. The mechanism for sticking/slipping boundary conditions is unclear. Frigaard *et al*. [14] suggest that sticking/slipping might be a result of local melting and subsequent solidification. Though it is agreed that local melting would cause a significant velocity reduction in the solid material adjacent to the melted region, the melted material does not

slip at the tool. The prevailing no-slip boundary condition at a solid-liquid interface has been well established, including liquid metal flows [11]. This no-slip condition is a direct result of the inability of a liquid to withstand a finite shear stress. It may be observed, however, that a molten liquid provides a lubricating layer between the pin and adjacent solid material, resulting in an apparent slip condition. By contrast, a solid can withstand a finite shear stress, and is therefore capable of slipping at the tool. Based on this assessment, it might seem more logical that during FSW, the material initially slips at the tool (with a slip velocity that may increase with the tool speed and even approach the tool speed [13]) until the material is sufficiently softened (through frictional heat input) such that it cannot withstand the shear forces imposed by the rotating tool. At this point, local melting may occur and the molten metal sticks to the tool, but the solid material immediately adjacent to this liquid region (which might only be a few microns in thickness) experiences a significant reduction in velocity. The boundary condition, however, would be dynamic in nature as the liquid region intermittently forms and re-solidifies. Even without local melting, it may be that material flow stress gradients near the tool in FSW are steep enough that a local element of highly softened material in contact with the tool temporarily sticks to the tool due to the high stress surrounding the element. Relatively hard material, which is capable of resisting local shear stresses, then fills the wake of the accelerating soft material and a slipping condition is re-established. The extent of this scenario would be dependent on material properties (*i.e*, material flow stress behavior), operational conditions, and tooling.

Figure 5-2 also reveals a void immediately behind the pin. The void occurs only at approximately the mid-pin depth and below and is not observed at the surface (Figure

5-2c, d). Note that this void is not unique to plasticine, and a large void behind the pin in FSW of metals has previously been observed [15, 57-59]. The void is closed farther downstream of the pin by the downward force of the shoulder trailing edge of the shoulder. Formation of this void is attributed to the slipping interface between the material and pin, and is not an artifact of suspension of the tool motion. The stop-action process takes no more than 0.3 s to complete, during which the pin travels a maximum distance of 0.05 pin diameters (at the 1.1 mm/s feed rate used). Further, at the bottom of the void, arch-shaped lines are observed (Figure 5-2c insert) in the material similar to the arch-shaped ridges at the surface of the weld. The spacing of these lines at the weld surface has been correlated to the weld pitch (tool feed distance per rotation) [60] and would not be present if the void was caused by the stop-action process itself. Thus, the void must be present prior to the extraction of the tool. Formation of the void is attributed to insufficient contact between the process material and the pin. As explained previously in Chapter 1, if a void is present in the processed region, slipping must be occurring due to the extremely viscous nature of material flow during FSW. However, a slipping condition may not always result in void formation, as concluded by Frigaard *et al.*[14]. Arbegast [61] and Kim *et al*. [15] have suggested that defect formation results from improper selection of operational parameters such as rotational speed, feed-rate, and tool depth. Therefore, it appears that there may be a correlation between operational parameters, tool slip, and void formation, the specification of which is left for future work. Zettler *et al*. [58] and Zhao *et al*. [59] have demonstrated that a large internal void can occur over the entire length of the processed section under qualitatively similar processing conditions (high weld pitch, where material does not rotate more than once

around the tool pin) for Al 2024 and 2014, respectively. Internal void formation in metals along the length of the processed section as well as a large void behind the pin that fully closes under the trailing edge of the shoulder (similar to Figure 5-2) has also been observed in the FSW laboratory at Brigham Young University.

Figure 5-2d shows four sections of the Streamline Configuration cut transverse to the feed direction (in the *y*-*z* plane) at several longitudinal locations. Each of the four images in Figure 5-2d are viewed from an upstream vantage point. The top image is a section at the leading edge of the pin at the point where the material contacts the pin (the hole in the plasticine is from the leading edge of the pin). Note that as material flows around the pin, the extent of material deformation transverse to the welding direction is greater near the tool shoulder then lower in the weld. As the pin approaches, all streamlines deflect around the retreating side of the pin. In addition to extruding around the retreating side of the pin, the lower part of streamline 4 (identified in the fully processed image, F.P.) is forced under the pin. As the material continues to flow around the pin, streamline 4 splits into upper and lower sections in the mid-pin image. At the trailing edge of the pin this magenta streamline appears as two separate pieces, which surround the trialing edge pin void. As the material is squeezed under the trailing edge of the shoulder (recall that the tool is tilted 2.5 degrees) the streamline markers are pulled toward the advancing side by the rotating tool. Note that near the bottom half of the pin, the centerline (between streamlines 2 and 3) remains shifted to the left.

Figure 5-2e and f are a series of cross-sections from the Lap and Staggered Lap Configurations. These arrangements provide a more detailed analysis of vertical material motion during FSW. Sections at the leading edge and mid-pin in both Figure 5-2e and f

show that as material flows to the retreating side of the pin, it is also extruded upward to fill the concave shoulder. Both configurations show that material lower in the weld is lifted significantly at the retreating side of the pin during the weld. Material remains at its initial vertical location, however, on the advancing side of the pin. Behind the pin, as the weld finishes, material is forced downward in a clockwise motion about the longitudinal axis, filling the trailing edge pin void. A similar flow of material in aluminum FSW has been observed by Seidel and Reynolds [7]. From the pin trailing edge and fully processed sections, it is observed that the process of filling the void results in extrusion of material at the upper half of the weld to the bottom of the pin. This vertical motion suggests that the lower mixed material in Figure 5-2b was initially at or near the surface and forced down to the pin tip at the back of the tool. Note that material from the rotating region is much more prominent in Figure 5-2b, because before the tool encountered the magenta material, the rotation region contained only cyan material. With all other configurations, such a sudden change in material around the rotating region does not occur, and hence material from the upper rotating region is less apparent.

5.2.2 Threaded Pin – 250 RPM

A section from the Longitudinal Configuration processed with the threaded pin tool (no flash depth) at weld conditions otherwise identical to Figure 5-2a is shown in Figure 5-4a. In contrast to the smooth pin, a significant amount of the cyan plasticine has been carried forward several pin diameters into the magenta material at the bottom part of the pin. For this to occur, the cyan material must be entrained in a rotating region around the pin. Generally, material in the rotating region is manifest as a mixture of cyan and

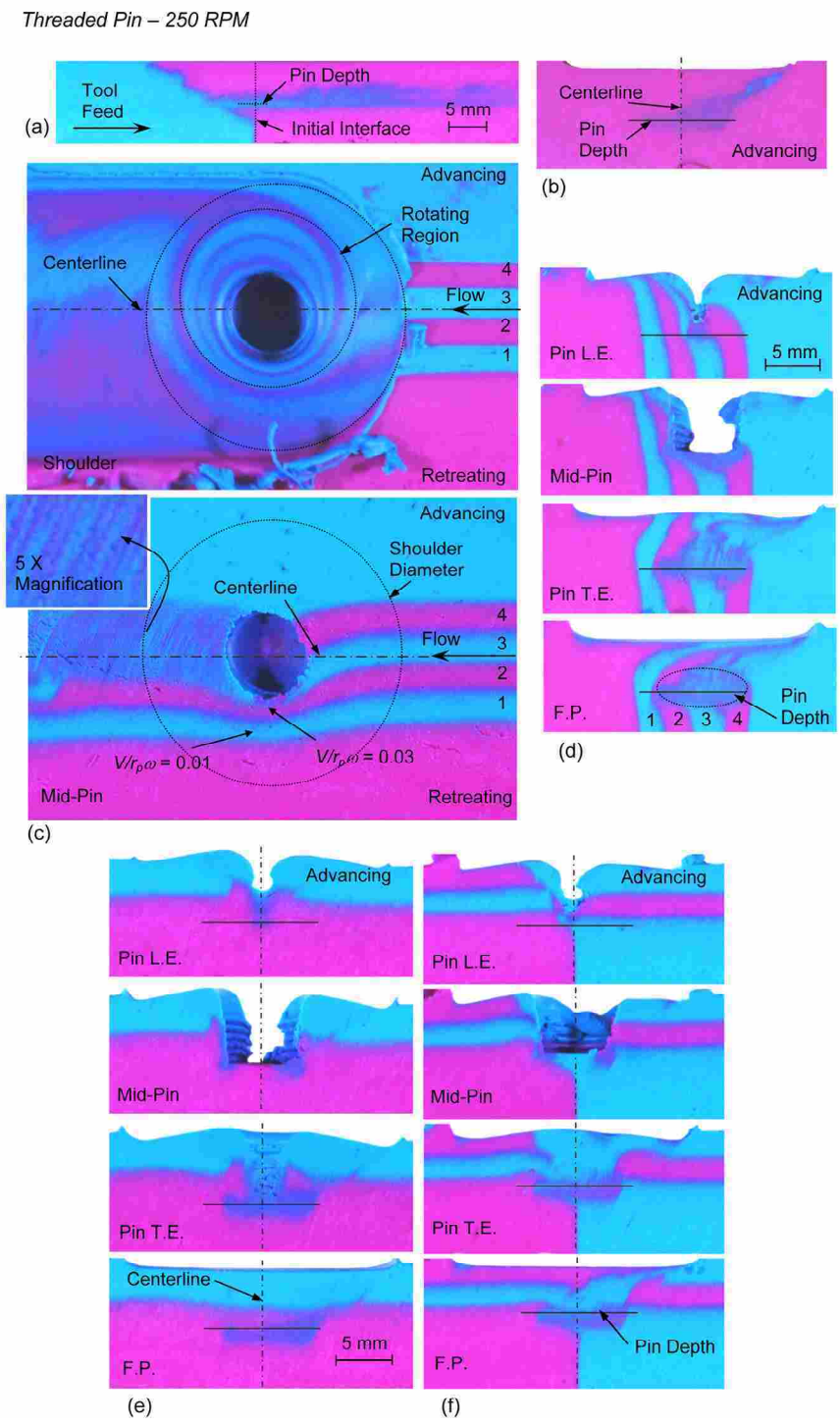

Figure 5-4: Processed plasticine using the threaded pin tool with a rotational speed of 250 rpm (1.1 mm/s feed rate): a) Longitudinal Configuration cut along the centerline, b) Longitudinal Configuration cross-section 10 mm forward of cyan/magenta interface, c) Streamline Configuration at the surface and mid-pin depth, and cross-sections at several longitudinal locations for the d) Streamline Configuration, e) Lap Configuration, and f) Staggered Lap Configuration.

magenta plasticine. As the tool advances, this entrained material is deposited near the pin tip (and underneath the pin) due to the downwash of the threads. The cyan plasticine (present in the mixed material) remains trapped around the tool for a distance over 3 shoulder diameters forward of the interface. Figure 5-4b shows that this mixture of material is deposited over much of the advancing side of the weld and even extends to the retreating side of the weld at the pin tip. The size of the mixed region is larger at the advancing side of the weld. This is because much of the material in the rotation zone around the pin is expelled at the advancing side of the pin (the remainder is expelled under the entire pin). At the top of the image a small amount of pure cyan material is observed. This is material that deformed directly under the shoulder, and it is clearly different than that mixed in the pin threads. The height of the mixed region from the pin at the advancing side of the weld is approximately the same size as the length of the threaded region on the pin (recall that the threads do not extend up to the shoulder as shown in Figure 2-1).

Figure 5-5 presents two images from another weld of the Longitudinal Configuration where the tool was suspended as the pin penetrates the interface between the cyan and magenta colors of plasticine. Deformation at the surface may be compared

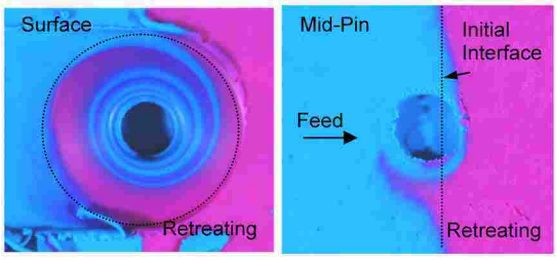

Figure 5-5: Plan view sections of the Longitudinal Configuration at the surface and mid-pin depth with stop action as the threaded pin penetrates the cyan and magenta plasticine interface.

to the smooth pin weld in Figure 5-5b. Additionally, material deformation at the mid-pin depth is very similar to the smooth pin stop-action weld. There appears to be a larger region of cyan material around the pin compared to the Figure 5-5b. However, the distance that the tool has penetrated into the magenta material is smaller.

Sections of the Streamline Configuration for the threaded pin tool at a rotational speed of 250 rpm are shown in Figure 5-4c and d. Compared to the smooth pin case, there is slightly more mixing of material at the shoulder. This result, however, is likely due to minute changes in the tool depth and only affects material flow very near the surface. Generally, the tool depth can be set so that no material mixes at the shoulder, but as the tool depth increases, mixing at the surface begins. Eventually, once the depth is sufficient, flash appears at the shoulder and mixing at the shoulder can become substantial. For the 250 rpm case, these effects are concentrated at the surface. However, as will be shown subsequently for the 1000 rpm rotational rate, the increase in tool depth to the point of flash generation can result in differences in material flow even lower in the weld.

Aside from the slightly increased mixing and deposition further toward the advancing side, material flow at the surface between Figure 5-4c and Figure 5-2c is similar, including the size and shape the rotating region. Large differences between the two tools however, are noticeable at the mid-pin depth. At the mid-pin depth, streamline 4 and much of streamline 3 enter the threads and rotate with the pin, mixing to a uniform color before deposition. Since these streamlines enter the threads, the material velocity cannot be measured by mass conservation as was done for the smooth tool. The peak velocity along streamlines 3 and 4, however, are nearly identical to the smooth pin weld.

The cyan/magenta mixture in the rotating region is deposited behind the pin in fine arc-shaped layers (see Figure 5-4c enlargement) between cyan material from streamline 3 (and possibly cyan material above streamline 4). Similar to FSW in metals, the spacing between these bands is approximately equal to the weld pitch and are more pronounced at the advancing side of the pin [8, 10, 60]. The layers suggest a periodic deposition of cyan material from either side of streamline 4 from the rotating region inside the threads. The rotation region around the pin inhibits void formation in the threaded pin scenario.

Cross-sections of the Streamline Configuration (Figure 5-4d) show a significant FSW-affected area under the threaded pin. The deposited cyan/magenta mixture from the rotating region is observed at the bottom center of the weld in the pin trailing edge and fully processed images. This mixture is approximately oval in shape, similar to the concentric ring pattern observed in some FSW cross-sections of metals [3, 5, 8, 17]. The ring pattern is not as apparent in the plasticine because the two colors mix more uniformly than most metals alloys. Also, notice in the mid-pin cross-section that the bottom of the pin contacts streamline 2, a retreating side marker. Thus some of the material from the retreating side of the weld is pulled into the rotating region around the bottom of the pin. This small mixed region of advancing and retreating side material is also observed in Figure 2-8 (250 rpm, 1.1 mm/s). Since there is no rotation region around the bottom of the smooth pin, this mixed area is absent in Figure 2-10. Note that even though only a small amount of the rotating region can be observed in Figure 5-4d, the rotating region exists over much of the length of the pin as discussed above for Figure 5-4a.

Vertical motion from FSW with the threaded pin is illustrated in more detail in Figure 5-4e and f. The pin threads pull some of the upper cyan material down where it mixes with the magenta material. As the cyan material from the upper part of the weld is drawn down, the lower magenta layer in Figure 5-4e is deformed upward on both sides of the pin. This differs from results for the smooth pin weld, where only the retreating side material moved upward. Under the back of the shoulder (Pin T.E. and F.P. sections), the magenta material in the Lap Configuration that had deformed upward around the pin is forced down and ends approximately at its initial vertical location. Underneath the pin, however, a mixture of cyan and magenta material is observed. This mixed region is nearly completely surrounded by magenta material, and unlike the smooth pin weld in Figure 5-2e, the upper cyan material does not extrude vertically downward at the advancing side of the processed zone as the weld finishes. Recall, that with the smooth pin material at the advancing side of the weld was forced down to fill the trailing edge pin void, which is absent with the threaded pin. The Staggered Lap Configuration (Figure 5-4f) shows that the original interface between advancing and retreating sides is shifted to the retreating side and material in contact with the pin is primarily from the advancing side (Pin L.E. section). Therefore, the mixture of cyan and magenta at the bottom of the pin is primarily comprised of the top two layers of material at the advancing side of the centerline.

To summarize, in FSW with a threaded pin tool, material becomes trapped inside the pin threads and is carried several shoulder diameters forward with the tool before being deposited in arch shaped layers behind the pin. In addition, some material inside

the threads is forced downward and deposited at a greater depth under the pin tip compared to the smooth pin weld at the same operating conditions.

5.2.3 Smooth Pin – 1000 RPM (No-Flash Tool Depth)

Figure 5-6 shows the processed sections for the smooth pin tool rotating at 1000 rpm. The tool depth was adjusted so that no material was expelled from the FSW zone (no flash). At 250 rpm, flash generation was found to have relatively little effect on bulk flow features (refer to Chapter 2). However, at 1000 rpm an increase in tool down force can dramatically alter material flow patterns. Processed sections with flash generation will be discussed later. It is noted that to create a weld with no flash at 1000 rpm requires raising the tool approximately 0.4 mm from the position used for welds at 250 rpm.

Figure 5-6a is a section from the Longitudinal Configuration cut along the centerline. A mixture of cyan and magenta plasticine is present along the entire length of the section at the surface of the workpiece. Some of the cyan material remains under the shoulder, gradually being replaced by the magenta plasticine for the entire weld. (A mixture of cyan and magenta was still present under the shoulder when the tool was extracted at the end of the workpiece, to the right of the photograph.) A small amount of cyan material also becomes trapped under the pin. A cross-section of the Longitudinal Configuration weld 10 mm forward of the initial interface is shown in Figure 5-6b. Compared to the 250 rpm rotational speed with the smooth pin (Figure 5-2b), the amount of mixed cyan and magenta material lower in the weld is quite small. All of the cyan plasticine under the pin is expelled once the tool travels approximately 1 shoulder diameter past the initial interface between the two plasticine colors. However, unlike the

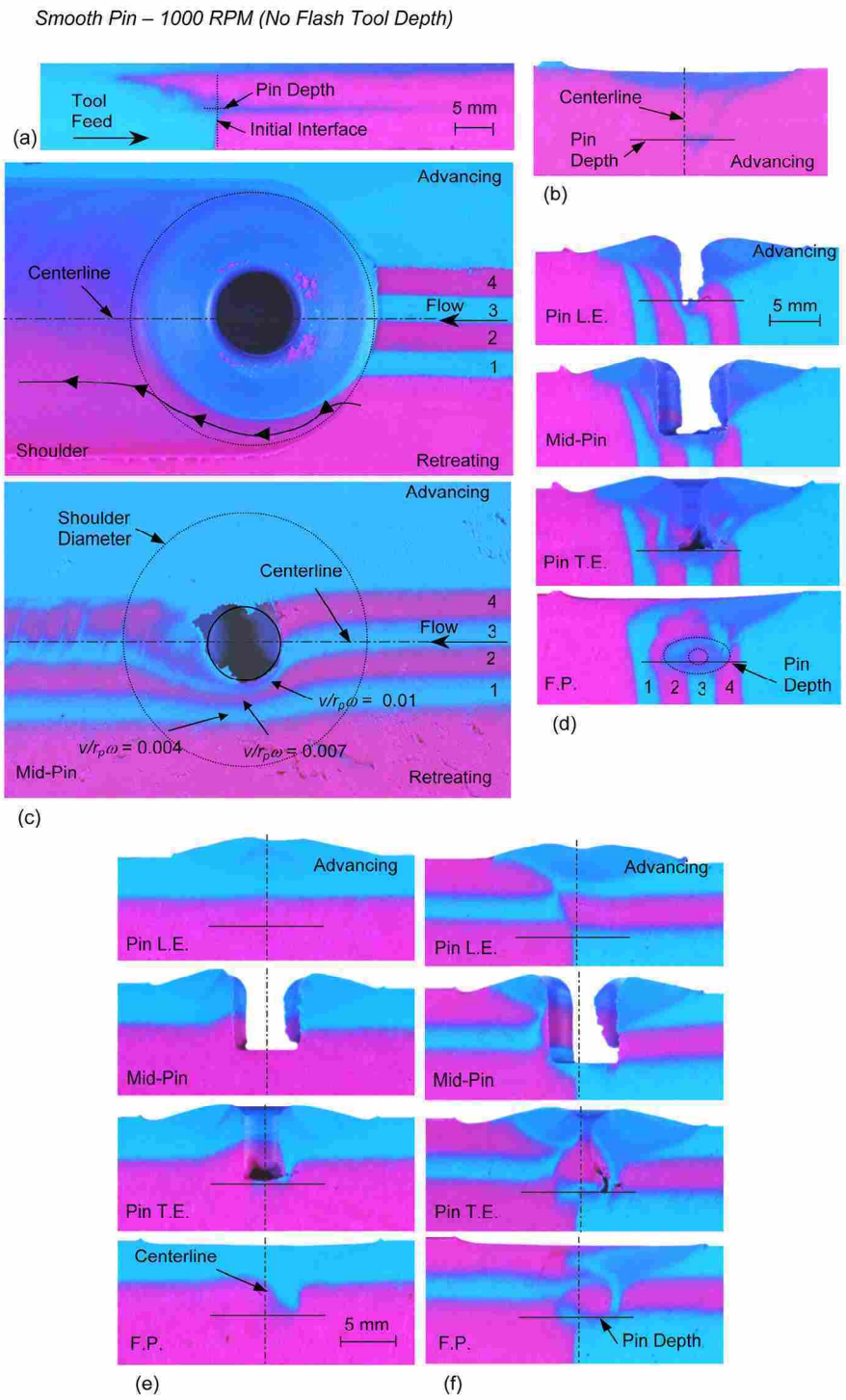

Figure 5-6: Processed plasticine using the smooth pin tool with a rotational speed of 1000 rpm (1.1 mm/s feed rate) without flash generation: a) Longitudinal Configuration cut along the centerline, b) Longitudinal Configuration cross-section 10 mm forward of cyan/magenta interface, c) Streamline Configuration at the surface and mid-pin depth, and cross-sections at several longitudinal locations for the d) Streamline Configuration, e) Lap Configuration, and f) Staggered Lap Configuration.

250 rpm case, mixing directly under the shoulder across much of the surface from the retreating to advancing side of the weld is also apparent in the cross-section image.

Mixing at the shoulder is further observed at the surface of the Streamline Configuration in Figure 5-6c. Notice in the surface section, that except for the far retreating side of the shoulder where some of the magenta material is simply extruded around the tool along an arced path (indicated by the sketched pathline with arrows), all material under the shoulder is a uniform mixture of cyan and magenta plasticine. At the mid-pin depth, however, the flow of material is comparable to the 250 rpm rotational rate in Figure 5-2c. Even at 1000 rpm, a void (although smaller than at 250 rpm) appears at the trailing edge of the pin on the advancing side. Normalized velocities ($v/r_p\omega$), estimated from conservation of mass at corresponding locations shown in Figure 5-6c are approximately an order of magnitude less than the 250 rpm case (suggesting significantly more slip and/or much higher velocity gradients, and associated frictional heating), and absolute material velocities at 250 and 1000 rpm are nearly identical. However, it is expected that much higher velocities occur in the rotation region directly under the shoulder due to the extent of material mixing.

Consistent with Figure 5-6a, the transverse cross-sections in Figure 5-6d exhibit regions of mixing directly under the shoulder and pin tip. These regions are considerably different from the 250 rpm weld in Figure 5-2d. Much of the mixed material directly under the shoulder advances with the tool, and as observed in the fully processed section, any material that is expelled from the FSW zone is pushed to the advancing side by the trailing edge of the shoulder. It was shown in Chapter 2 that higher rotational speeds result in significant heating inside the welding zone. The consequence of much higher

temperatures is a reduced material flow stress, which allows the material to flow more readily around the tool. It should be noted that even though strain-rates may also increase near the tool at high rotational speeds, which would act to increase the flow stress, the plasticine is much more sensitive to temperature changes than increased strain-rates. The center region of the fully processed (F.P.) cross-section has an appearance resembling the concentric ring pattern observed in some metal FSW cross-sections [8]. Generally, the ring pattern is not observed in cross-sections from FSW with a smooth pin, and has previously been attributed to the pin threads [62]. The fully processed cross-section in Figure 5-6c, however, suggests that the formation of the ring pattern is not a result of pin threads alone since the general shape of the ring pattern is clearly evident as illustrated in the figure. It is likely that the concentric rings are created both by a longitudinal rotation from material flow under the trailing edge of the shoulder and cyclic deposition of the rotating region material surrounding the pin threads, as discussed for the 250 rpm threaded pin weld in the section above.

The Lap and Staggered Lap Configurations are shown in Figure 5-6e and f, respectively. Both configurations display more material mixing directly under the shoulder (especially in the Staggered Lap Configuration) compared with the low rotational speed used for Figure 5-2e and f. The Lap Configuration (Figure 5-6e) shows a small amount of a cyan/magenta mixture around the pin near the surface of the workpiece. During FSW, a small amount of the lower magenta material must gradually work its way up to the surface with the upward flow of material that fills the concave shoulder. This mixture of cyan and magenta plasticine under the shoulder advances with the tool and is not observed in the fully processed section in Figure 5-6e. By comparison

with Figure 5-6e, it can be concluded that the mixed region under the tool shoulder in Figure 5-6f is primarily comprised of the cyan/magenta layers on either side of the centerline at the surface of the workpiece. Formation and deposition of the mixed region in the upper part of the FSW zone of the staggered lap setup is consistent with cross-sections from the Streamline Configuration in Figure 5-6d.

The primary difference between material flow at 1000 and 250 rpm with the smooth pin is a substantial increase in material mixing across the centerline directly under the shoulder and pin tip. At the mid-pin depth, flow patterns (and absolute material velocities) are nearly independent of rotational rate.

5.2.4 Threaded Pin – 1000 RPM (No Flash Tool Depth)

Material motion along the feed direction using the threaded pin tool at the high rotational speed is observed in Figure 5-7a. Similar to the high-speed smooth pin weld, some cyan plasticine becomes trapped directly under the shoulder, moving forward with the tool. At the bottom half of the pin, however, a mixture of the two plasticine colors appears for a significant distance forward of the interface line (approximately 2 shoulder diameters) and is much larger than the weld with the smooth pin tool (Figure 5-6a). In fact, Figure 5-6b shows that this large mixed region is the dominant feature in the welded section. Recall that this image is a cross-section 10 mm forward of the initial cyan/magenta interface. This intermediate color of clay is material that rotated in a region around the pin and inside the threads, similar to the 250 rpm data of Figure 5-4a. After several pin diameters (at the right of the photograph), the remainder of the entrained cyan material under the shoulder is more suddenly expelled from the tool and

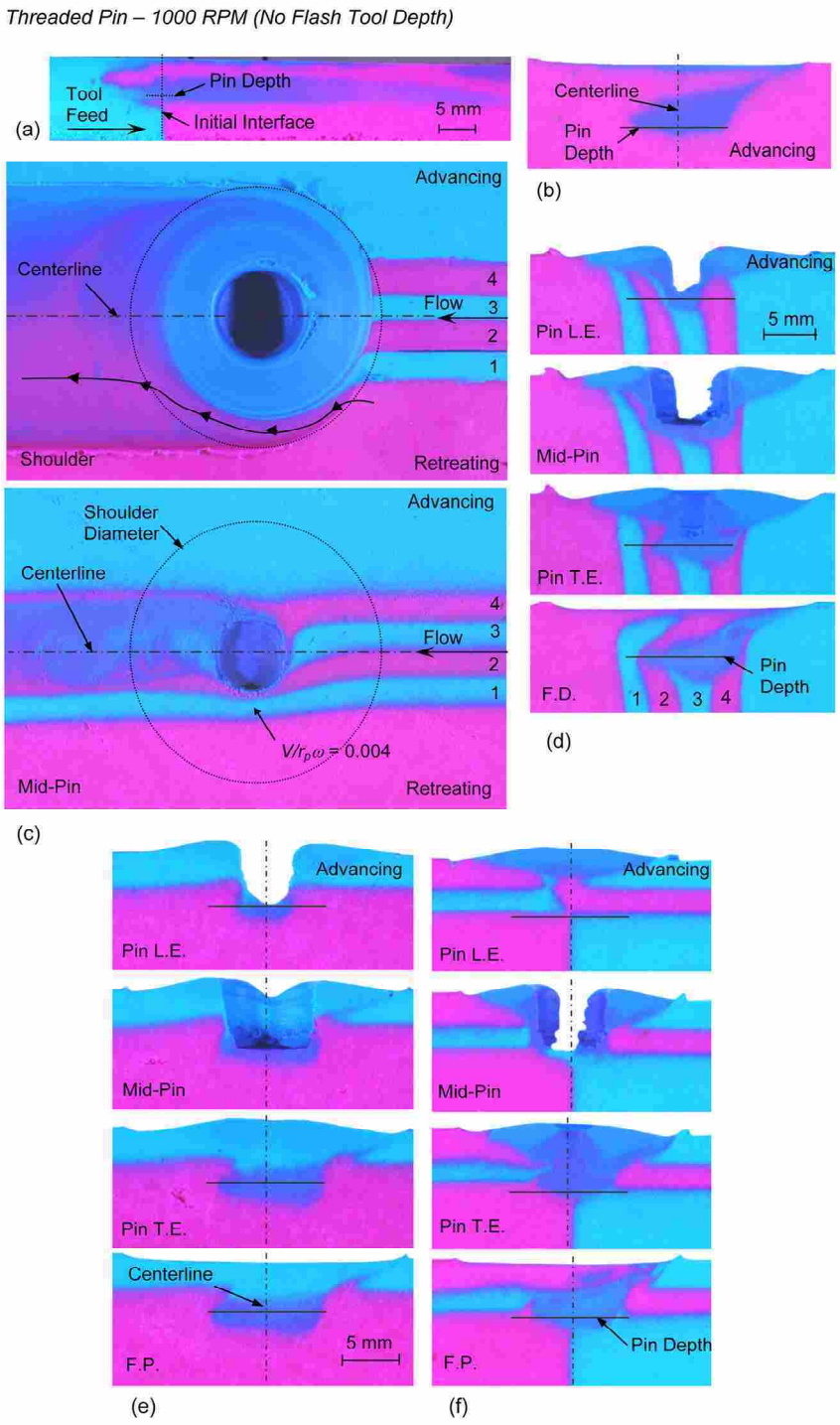

Figure 5-7: Processed plasticine using the threaded pin tool with a rotational speed of 1000 rpm (1.1 mm/s feed rate) without flash generation: a) Longitudinal Configuration cut along the centerline, b) Longitudinal Configuration cross-section 10 mm forward of cyan/magenta interface, c) Streamline Configuration at the surface and mid-pin depth, and cross-sections at several longitudinal locations for the d) Streamline Configuration, e) Lap Configuration, and f) Staggered Lap Configuration.

the amount of the cyan plasticine lower in the section rapidly decreases. The exact cause of this sudden change in flow is unknown but probably due to subtle changes in the tool depth (*i.e.*, the surface of the plasticine is not perfectly flat).

At the surface of the weld, the Streamline Configuration in Figure 5-7c is nearly identical to the smooth pin weld at 1000 rpm of Figure 5-6c. The only difference is that the mixed material contains somewhat less magenta plasticine (the color is closer to that of the cyan material), most likely due to a slightly shallower tool depth. The rotating region can also be seen at the mid-pin depth as a thin layer of mixed material around the circumference of the pin. In contrast to the lower-rpm and smooth pin results of Figure 5-4c and Figure 5-6c, the extent of the FSW-affected zone in Figure 5-7c is larger at the advancing side of the pin and a portion of streamline 4 actually extrudes around the advancing side of the rotation region. At the 250 rpm rotational speed (Figure 5-4c), there is significant mixed material downstream of the pin and the spacing between the mixed material and cyan material layers outside the rotating region was determined to be equal to the weld pitch. At 1000 rpm, however the weld pitch is 0.07 mm/rot and the very small spacing that might exist between material from the rotational region and outer extruded material cannot be observed. Some bands similar to Figure 5-4c are also observed in Figure 5-7c in the mid-pin image, but the average spacing (0.7 mm) in Figure 5-7c is much larger than the weld pitch. The spacing in Figure 5-7c is also more irregular where no bands are observed at the far advancing side of the mixed region downstream of the pin.

The normalized velocity along streamline 1 is identical to that found in the high-speed smooth pin weld (Figure 5-6c). (Velocities along all other streamlines near the pin

at the mid-pin depth cannot be estimated by mass conservation because of the larger rotating region.) Transverse cross-sections of the Streamline Configuration (Figure 5-7d) contain large cyan/magenta mixed regions at both the upper portion of the weld (similar to Figure 5-6d) and the bottom of the pin (similar to Figure 5-4d). The cross-section at the middle of the pin exhibits a more uniform rotation region along the length of the pin than the smooth pin weld at the same operating parameters. Note also that the mixture contains more magenta near the pin than at the shoulder (*i.e.*, the plasticine color is darker near the pin). The leading edge image (Pin L.E.) in Figure 5-7d shows that the increase in magenta comes from streamline 4, which flows under the upper rotating region and into the pin. In addition, some of the rotating region directly under the shoulder is pulled down by the pin threads. Rather than deposition of this mixed material at the upper advancing side of the weld as observed with the smooth pin (Figure 5-6d), the rotating region is deposited near the bottom of the pin.

The Lap and Staggered Lap Configuration in Figure 5-7e and f exhibit mixing directly under the tool shoulder and near the pin tip. Unlike the weld with the smooth pin at the same operating conditions (Figure 5-6), there is a substantial zone of mixed material around the bottom portion of the pin in both figures. This mixed zone is larger than the low-speed weld with the threaded pin (Figure 5-6e and f). There is also significant mixing directly under the shoulder in the Staggered Lap Configuration of the two plasticine colors on either side of the centerline. However, material from this cyan/magenta mixed zone is pushed to the advancing side of the weld under the trailing edge of the shoulder, and the top retreating side magenta layer appears across much of the surface of the weld in the fully processed section.

In review, increasing the rotational rate with the threaded pin results in more mixing between material at the advancing and retreating sides at the surface of the weld (similar to the high-speed smooth pin weld). In addition, the size of the cyan/magenta mixed region around the bottom of the pin is much larger than both the low-speed threaded pin and high-speed smooth pin welds discussed above. This effect results when upper mixed material is pulled downward by the threads. A high rotational rate with the threaded pin also increases size of the FSW-affected area transverse to the welding direction compared to both the low speed weld with the threaded tool and the 1000 rpm weld with the smooth pin.

5.2.5 Smooth Pin – 1000 RPM (Flash Tool Depth)

Tool depth was found to exert a significant impact on material flow at high tool rotational rates. Flash is generated by increasing the tool depth by only 0.3 - 0.4 mm from the no-flash weld depth. This increase in depth approximately doubles the vertical force on the plasticine during welding. Sections of the Longitudinal Configuration processed using the smooth pin tool at 1000 rpm with flash generation are shown in Figures 7a and b. Note that the governing variable is tool depth (or down-force) but flash is a tactile indicator of a significant change in material flow. Surprisingly, the images are almost identical to the smooth pin section with no flash at the same rotational rate (Figure 5-6a and b). In both cases, cyan material at the pin tip is transported approximately 1 shoulder diameter forward of the interface, and at the surface, cyan material is observed for the entire length of the weld (4 shoulder diameters forward of the interface). However, the concentration of cyan material at the end of the weld was found to be

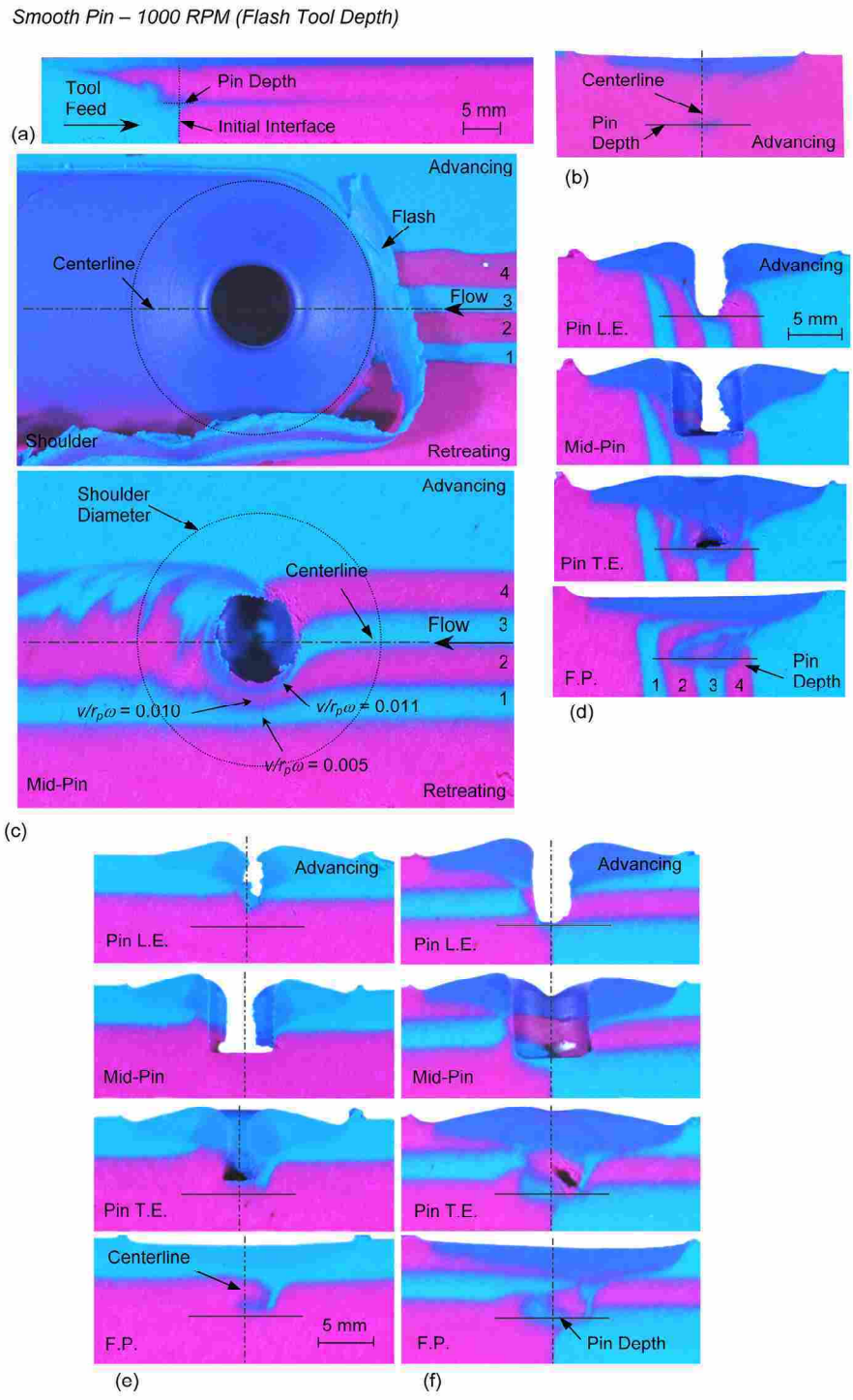

Figure 5-8: Processed plasticine using the smooth pin tool with a rotational speed of 1000 rpm (1.1 mm/s feed rate) with flash generation: a) Longitudinal Configuration cut along the centerline, b) Longitudinal Configuration cross-section 10 mm forward of cyan/magenta interface, c) Streamline Configuration at the surface and mid-pin depth, and cross-sections at several longitudinal locations for the d) Streamline Configuration, e) Lap Configuration, and f) Staggered Lap Configuration.

higher directly under the shoulder with the flash weld compared to no flash conditions.

Significant differences between the no-flash and flash welds, however, are noticeable in all other workpiece configurations. In Figure 5-8c the surface of the weld is nearly entirely comprised of a uniform mixture of cyan and magenta material (even downstream of the tool). In the surface image, flash generation at the leading and retreating edges of the shoulder is apparent. Initially, it was thought that increasing the tool depth would result in higher velocities and increased mixing throughout the weld. However, material mixing at the mid-pin depth is minimal and measurable velocities at the mid-pin depth are nearly identical to the no-flash weld (within the uncertainty of the measurement technique). Additionally, even with the increased down force, a small void still persists at the back of the pin. The most significant change at the mid-pin depth with flash generation is a slight increase in material mixing (which may come from the upper portion of the weld) and an increase in the transverse extent of deformation at the advancing side of the weld. Another difference compared to the no-flash weld with the smooth tool (of Figure 5-6c), is that each streamline marker in the figure remains undeformed until just upstream of the pin, where material deflects somewhat more sharply around the front of the pin. Note that streamline 4 cannot be observed behind the tool and much of it must extrude up near the shoulder where it is mixed with cyan material and deposited in the upper region above the mid-pin plane. The thinner deformation zone at the front of the pin is attributed to higher temperatures, and thus a lower flow stress of material near the pin compared to material away from the pin. It has previously been demonstrated that increasing the tool depth increases the shoulder temperature [63]. The first three transverse cross-sections in Figure 5-8d are nearly

identical to Figure 5-6d. However, unlike the no-flash condition, the entire top portion of the fully processed weld (F.P.) is a uniform mixture of the two plasticine colors. Additionally, in the fully processed image, streamline 1 is pushed from the retreating side to the advancing side of the weld underneath the mixed rotating region. In all other welds presented above, similar deformation of this streamline occurred very near the surface.

Transverse cross-sections from Lap and Staggered Lap Configurations (provided in Figure 5-8e and f) exhibit more mixing in the upper region near the shoulder compared to the no-flash weld. Some of the lower magenta plasticine (mixed with cyan) is observed around the length of the pin in the Lap Configuration. Although most of the magenta material that appears higher in the FSW cross-section is limited to a region near the pin, a small amount has spread outward under the shoulder. Upon close examination of Figure 5-8e it can be seen that downstream of the shoulder (F.P. section) a mixture of cyan and magenta material is present in a region extending directly under the shoulder to approximately 2 mm below the surface. Significant cyan/magenta material mixing from either side of the centerline at the shoulder is apparent in the Staggered Lap Configuration. Again, unlike the no flash condition, this mixture from the shoulder is prominent in the fully processed section in Figure 5-8f.

In general, increasing the tool depth to the point of flash generation causes advancing/retreating side material directly under the shoulder to mix intensely. This mixture is evident even in the fully processed weld downstream of the tool. The deeper tool depth also results in a wider FSW-affected area transverse to the feed direction (behind the pin) compared to the no flash weld with the smooth pin of Figure 5-6. The

FSW-affected area at the front of the pin, however, is slightly reduced possibly due to increased heat input and softening of material very near the tool. Vertical motion also becomes more significant with deeper operation conditions where material from the bottom half of the weld flows into the mixing region directly under the shoulder.

5.2.6 Threaded Pin – 1000 rpm (Flash Tool Depth)

Variation in material flow features between the no-flash versus flash processing conditions with the threaded pin is significant at high rotational rates. A section of the Longitudinal Configuration in Figure 5-9a is comparable to the smooth pin weld in Figure 5-8a. However, a section transverse to the weld in Figure 5-9b exhibits a much larger region of mixed material at the pin tip than the smooth pin weld under similar conditions. Nevertheless, this mixed region at the bottom of the pin is smaller than the no-flash weld with the threaded pin in Figure 5-7b. The reason for the reduced mixed region size is explained below. This mixed region near the pin tip extends for only 1 shoulder diameter forward of the interface, but substantial cyan material is observed at the surface of the workpiece for the entire weld (the weld was suspended approximately 4 shoulder diameters forward of the interface).

The surface of the Streamline Configuration in Figure 5-9c is identical to the smooth pin weld with flash generation. However, the processed Streamline Configuration at the mid-pin depth in Figure 5-9c shows significantly more mixing than all other welds previously discussed. Streamline 1 at the retreating side appears to enter the rotating region behind the pin (and possibly some of the magenta plasticine at the retreating side of the streamline markers). The rotating region is small at the leading

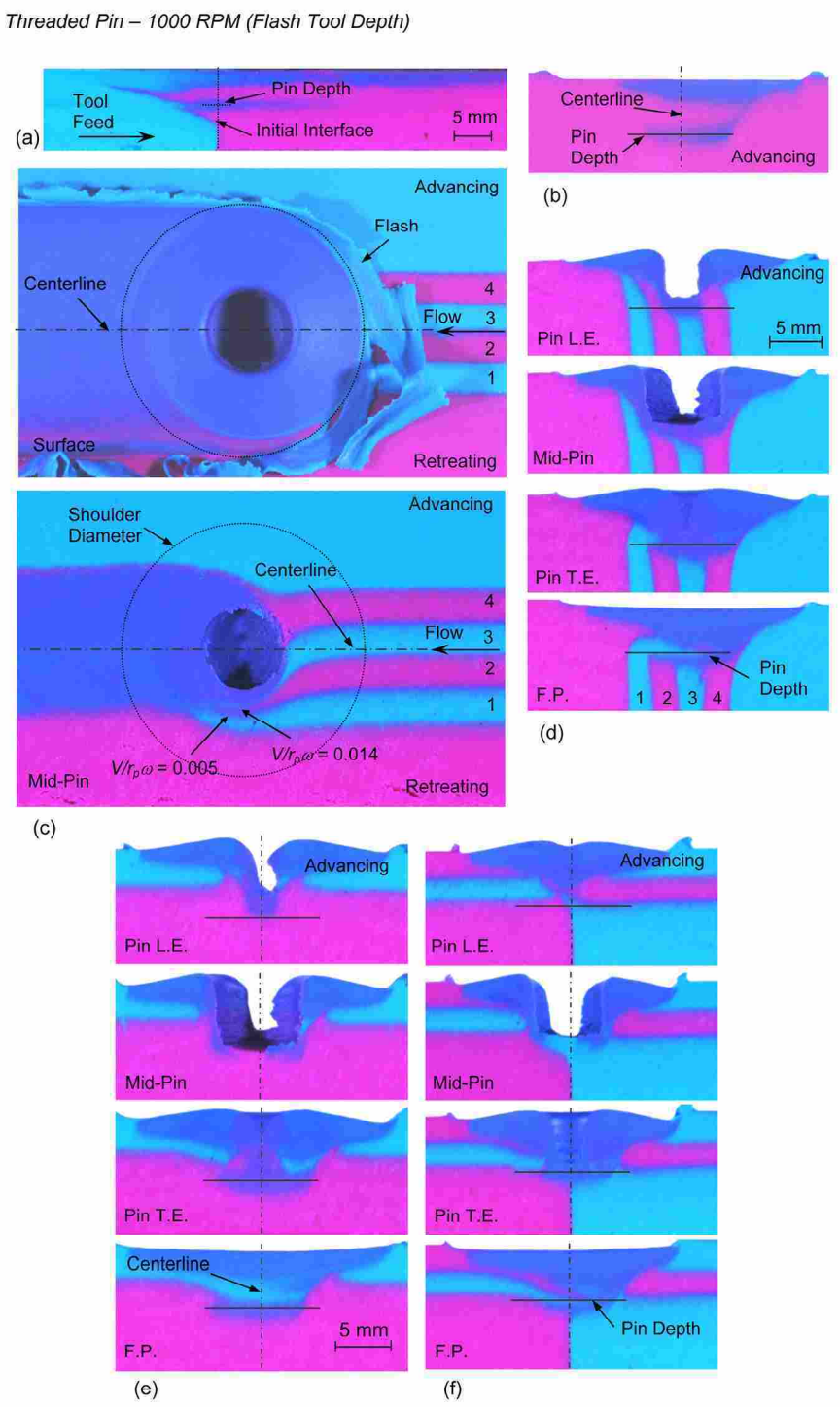

Figure 5-9: Processed plasticine using the threaded pin tool with a rotational speed of 1000 rpm (1.1 mm/s feed rate) with flash generation: a) Longitudinal Configuration cut along the centerline, b) Longitudinal Configuration cross-section 10 mm forward of cyan/magenta interface, c) Streamline Configuration at the surface and mid-pin depth, and cross-sections at several longitudinal locations for the d) Streamline Configuration, e) Lap Configuration, and f) Staggered Lap Configuration.

edge of the pin but grows around the retreating side. Behind the pin the rotating region is deposited well beyond the advancing edge of the pin. This wider deposit of material at the advancing side causes part of streamline 4 to deflect a distance approximately equal to the pin radius past the advancing edge of the pin. The mid-pin cross-section in Figure 5-9d also exhibits a thicker rotating region around the pin (at both sides of the pin) compared to Figure 5-7d and Figure 5-8d. In addition, with the deeper tool depth, material mixes more uniformly than Figure 5-7d and Figure 5-8d and a mixture of cyan and magenta material is present from the surface of the weld to the pin tip in each cross-section image. Similar to the smooth pin weld shown in Figure 5-8d, the increased tool depth and vertical force causes unmixed material at the retreating side of the rotation zone (*i.e.*, streamline 1) to deform toward the advancing side of the weld, separating the upper and lower mixed regions observed in the fully processed image.

The welded Lap and Staggered Lap Configurations are shown in Figure 5-9e and f. Compared to sections from the Lap Configurations in Figure 5-7e and Figure 5-8e, there is considerably more mixing of the two plasticine layers and uplift of material is extensive. The cyan/magenta rotation zone at the shoulder is obvious even downstream of the tool (F.P. section). The region of mixed material at the bottom of the pin, however, is thinner than the weld without flash generation with the threaded pin tool (Figure 5-7e). This effect is due to the deformation of unmixed material from the retreating to advancing side of the centerline lower in the weld as explained above. A similar mixture of cyan and magenta regions also appears in the fully processed section in Figure 5-9f. Unlike Figure 5-8f, however, the mixture of the two plasticine colors extends to the bottom of the pin.

In summary, increasing the tool depth with the threaded pin intensifies the rotating region directly under the tool shoulder, causing material at the upper weld zone to mix uniformly. Unlike the no-flash case, the upper rotating region is deposited uniformly behind the tool shoulder and is dominant in the fully processed weld. The thickness of the rotating region around the pin and the size of the FSW-affected area behind the tool are also larger than all other scenarios above. In addition, there is significantly more vertical recirculation in the rotating zone near the pin threads.

5.2.7 Butt Weld Joining

Although the discussion above provides a detailed assessment of material flow in FSW, it is beneficial to also investigate joining of two workpieces in a butt weld since such joining is typical in FSW. Butt welds with cyan-colored plasticine at the advancing side and magenta at the retreating side are shown in Figure 5-10. The figure shows welds for all six operating conditions discussed above, including rotational speeds of 250 and 1000 rpm for both the smooth and threaded pin tool, and at two tool depths for the 1000 rpm cases. For each weld a horizontal section at the surface of the weld is shown along with four transverse cross-sections at various locations around the extracted pin. These welds show many similarities to those discussed previously. For example, at increased tool depth (flash generation) and rotational rate (1000 rpm) mixing between the two sides of the weld is extensive, while mixing for the other cases is relatively minimal.

An interesting observation is evident in the horizontal image at the surface for the 250 rpm smooth pin weld. Notice that as the initial cyan and magenta interface rotates under the tool shoulder the two colors mix. The extent of mixing grows as the layers

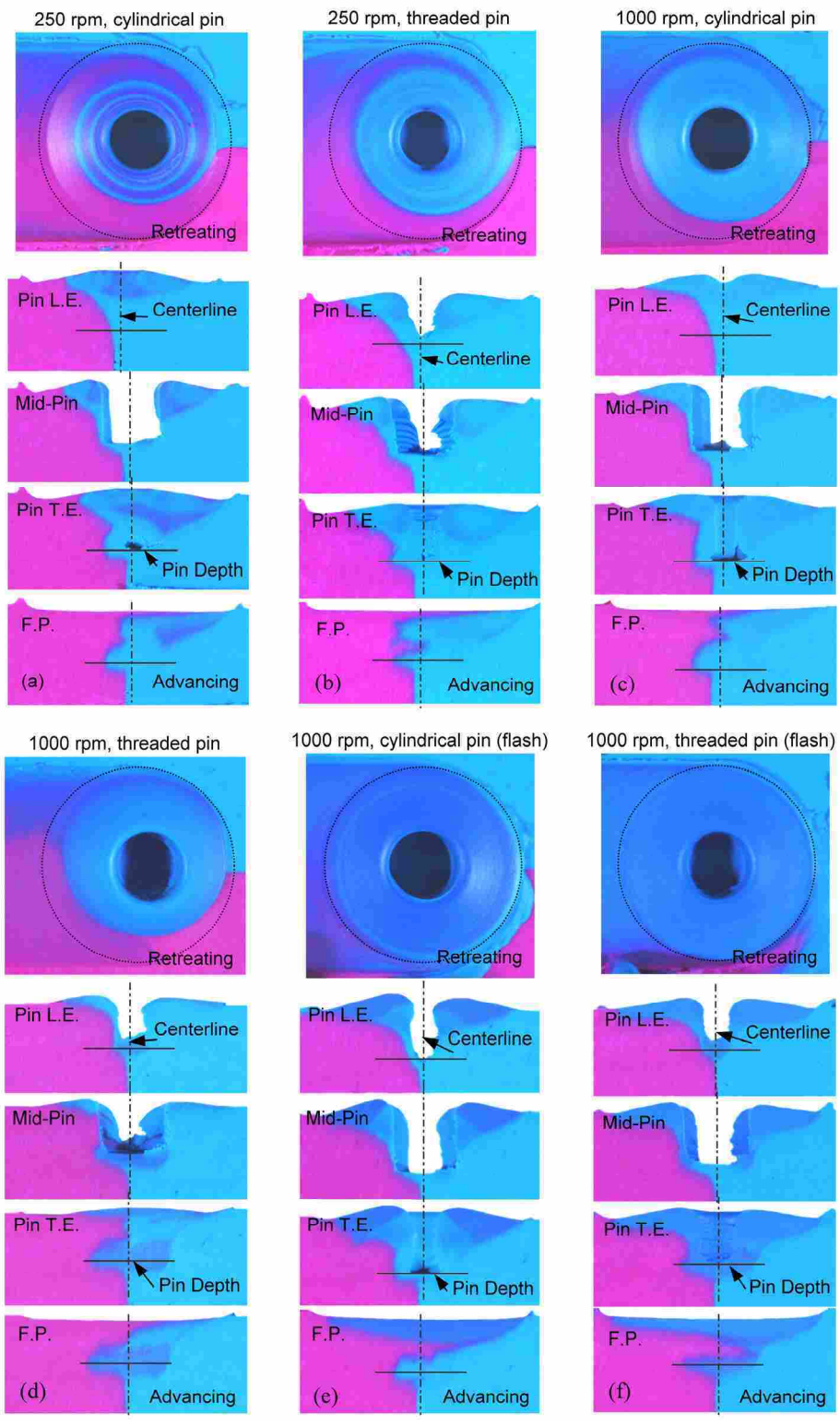

Figure 5-10: Butt welds at various operating conditions (1.1 mm/s feed-rate). For each operating condition a horizontal section is provided of the weld surface along with several transverse cross-sections around the extracted pin location.

spiral inward toward the pin. From this image it appears that mixing is occurring due to molecular diffusion. This result is unexpected and the mechanism for such diffusion is unclear. Placing the two colors on top of each other results in no diffusion of the two colors, even if left for several weeks. This mixing region concentrates at the pin and is pushed to the advancing side of the weld in the fully processed section. The 250 rpm weld with the threaded pin (Figure 5-10b) also shows this behavior. However, the interface spiral takes a wider path around the pin and mixed material is only minimal at the pin. For this welding scenario, a lower mixed region of cyan and magenta material was previously observed in a separate butt weld shown in Figure 2-8, which is absent in Figure 5-10b (F.P. section). However, notice that the weld in Figure 5-10b was conducted with the tool centered slightly to the advancing side of the centerline, and the retreating magenta material does not contact the pin at the pin tip. Thus, the mixing zone at the bottom of the pin cannot be seen in the image. For the no-flash welds at 1000 rpm (Figure 5-10c and d), the rotating region under the shoulder appears as primarily cyan material with only 5-10% magenta. The extent of the rotational region is also clearly evident in these two surface sections. In contrast to the smooth pin, the threaded pin weld also shows a substantial region of mixed material at the bottom half of the weld from the rotating region around the pin threads. By increasing the tool depth to the point of flash generation (Figure 5-10e and f), the entire surface of the weld (under the shoulder) for both tools rotates with the tool, and material mixes to nearly a uniform concentration of the two colors. For the threaded pin, the pin trailing edge section shows that the rotational region persists for the entire pin length. For both cases, a “flow arm” of magenta material is extruded from the retreating to advancing side of the weld in the fully

processed images. In Figure 5-10f this flow arm appears to split the rotating region into an upper and lower section. As the rotating region moves forward with the tool some of it is deposited at the upper portion of the weld and some at the bottom near the pin tip. At the middle of the weld, however, the retreating magenta material flows around the rotating region and is pulled to the advancing side of the weld. This behavior is also apparent in the cross-sections shown above in Figure 5-9.

In summary, with the smooth pin tool material generally deforms around the retreating side of the pin and extrudes upward to fill the concave shoulder. Additionally, a small void forms at the lower trailing edge of the non-threaded pin. This void is filled with material from the upper half of the workpiece as the material is forced out the concave shoulder at the back of the tool. With the threaded pin, material becomes entrained inside the pin threads and rotates many times with the tool. The threads force material down below the pin, causing material outside the rotating region to deflect upward around the pin. Most of the material inside the rotating region originates at the advancing side of the centerline and at the upper portion of the workpiece. Material that rotates with the pin is either cyclically deposited with material that extrudes around the outside of the rotating region, or is forced under the pin by the downwash from the threads. The rotating material in contact with the pin threads prohibits void formation behind the pin. At the mid-pin depth, material velocities adjacent to the smooth pin were only a fraction of the rotational pin speed. The velocity of material entrained inside the pin threads, however, may be significantly larger than the smooth pin case. Increasing the rotational rate had little effect on absolute material velocities a short distance from the tool at the mid-pin depth. Generally, however, a rotating region directly under the

shoulder was observed at higher rotational speeds for both the threaded and smooth pin tools, and velocities may increase considerably in this rotating region. A deeper tool depth (at high rotational rate) resulted in more material mixing in this upper rotating region, which is a prominent feature in fully welded cross-sections downstream of the tool. With the threaded pin, the increased tool depth resulted in a large mixing (or rotation) region extending the entire depth of the weld.

6 Computational Model

6.1 Continuum Mechanics Theory

Continuum mechanics includes the study of both solid and fluid mechanical behavior such as velocities, displacements, accelerations, forces, stresses, *etc*. Often (*i.e.*, in FSW), the mechanical behavior a continuum is also dependent on a thermal response as well. For example, general physical properties of a material may change with temperature. Additionally, at high strain-rates deformation (or viscous) heating cannot be neglected.

At every point in a fluid or solid continuum, there are fundamental equations of equilibrium that must exist, including conservation of mass, momentum, and energy (thermal transport). Conservation of mass states that mass can neither be created nor destroyed. This statement can be described mathematically as

$$\dot{\rho} + \rho\left(v_i\right)_{,i} = 0\,, \tag{6-1}$$

where ρ is density of the medium and v is the material velocity. In Eq. (6-1) the subscript i represents three mutually orthogonal directions (i = 1,2,3) and the comma denotes spatial differentiation. This equation states that the time rate of change of the materials density plus the net flow of material through the domain must be zero.

Newton's Second Law of Motion states that the sum of all forces is equal to the time-rate-of-change in linear momentum. Linear momentum is the product of mass and

velocity. For a unit volume, linear momentum is then the product of density and velocity. Forces on a control volume include internal or stress components (σ) and body forces such as gravity, magnetism, *etc*. (Z). Equating forces and the time-rate-of-change in linear momentum gives

$$\sigma_{ij,j} + Z_i = \rho \dot{v}_i + \rho v_{i,j} v_j . \tag{6-2}$$

The right-hand-side of Eq. (6-2) is the material time derivative of linear momentum after employing mass equilibrium. Differentiation of the stress tensor arises due to a resulting net force on the body. Also note that consideration of angular momentum results in the stipulation that the stress matrix is symmetric, that is $\sigma_{ij} = \sigma_{ji.}$

Finally, energy conservation (which is a generalization of the First Law of Thermodynamics) states that the sum of heat input and mechanical work per unit time on a control volume is equal to the time-rate-of-change of energy. Sources of work and energy in the control volume include kinetic energy, internal energy due to Brownian motion of particles, mechanical work of body forces, mechanical work of internal stresses, and volumetric sources such as electrical and/or chemical heating. Energy is transported through the control volume via conduction due to temperature gradients and advection. In its most general form, conservation of energy can be written as (after applying conservation of mass and linear momentum)

$$S - q_{i,i} = \rho \dot{e} + \rho e_{,i} v_i . \tag{6-3}$$

The two terms on the left-hand-side of Eq. (6-3) represent a volumetric source and thermal conduction, respectively. The right-hand-side is the material time derivative of the total energy, including kinetic and internal energy ($\frac{1}{2}\rho(v_i v_i)+\rho e$), where e is the internal energy due to Brownian motion (after imposing conservation of mass and linear

momentum to the balance equation). Thermal conduction is often modeled according to Fourier's Law, $q_i = -kT_{,i}$. where k is the material thermal conductivity, which may change with temperature T. To this point the only approximations made in Eqs. (6-1 through 6-3) is that the material can be treated as a continuum (and Fourier's Law is an adequate representation of thermal conduction). Therefore, these laws describe any continuum, including a liquid, solid, or gas.

For an incompressible solid the internal energy can be determined as

$$e = \int_{T_{ref}}^{T} c_p(T)dT\,, \tag{6-4}$$

where c_p is the constant pressure specific heat capacity. Since only gradients of the internal energy appear in Eq. (6-3), the reference temperature , T_{ref}, in Eq. (6-4) can be set to zero. Additionally, the only volumetric source for FSW is due to deformation heating, which can be modeled as $\sigma_{ij}v_{i,j}$. Thus, the governing equation for energy in steady-stae FSW becomes

$$\sigma_{ij}v_{i,j} + \left(kT_{,i}\right)_{,i} = \rho e_{,i}v_i\,. \tag{6-5}$$

Also, if the medium is incompressible, then Eq. (6-1) reduces to

$$v_{i,i} = 0\,. \tag{6-6}$$

Additionally, in FSW, body forces, along with inertial effects can be neglected without significant loss in accuracy [34], so that momentum equilibrium according to Eq. (6-2) reduces to

$$\sigma_{ij,j} = 0\,. \tag{6-7}$$

The above formulation is based on an Eulerian vantage point, *i.e.*, material flows through a fixed control volume. These equations must be transformed to a Lagrangian

frame, if instead, a material point is to be traced through the domain during application of loading.

The governing equations of momentum and energy contain four unknown quantities – velocities in each orthogonal direction and temperature. Mass equilibrium is a constraint to the solution of these equations. Recall from above that Eq. (6-1) was incorporated into both Eq. (6-2) and Eq. (6-3). The specific heat capacity (c_p) and thermal conductivity (k) must be experimentally determined. Additionally, an appropriate constitutive relation must be posed for the stress state. In general, the stress state is dependent on temperatures, strain, and strain-rate. The strain-rate is a function only of velocity,

$$\dot{\varepsilon}_{ij} = \frac{1}{2}\left(v_{i,j} + v_{j,i}\right). \tag{6-8}$$

However, the state of strain is dependent on the deformation history of the material. Using a Lagrangian approach the deformation of a material element is tracked directly. However, an Eulerian approach requires integration of Eq. (6-8) along a pathline as proposed by Cho *et al*. [30]. Despite this added complexity, the primary advantage in using the Eulerian approach for large deformation flow process is the capability for modeling the process as steady-state where the flow of material around the tool is constant in time (all time derivatives in the equations above vanish). Additionally, an Eulerian approach does not require remeshing since the grid is stationary. Both of these factors considerably reduce computation time.

It is only in modeling the stress state that the governing equations above diverge to the more traditional fluid and solid mechanics based models. Before the constitutive

stress model is established, some necessary fundamentals of stress and strain, particularly at yielding are first outlined.

6.2 Stress, Strain, and Yielding

In large deformation processes the plastic component of strain is much larger than the elastic response, and thus only plastic strains are modeled. Note that stress and strain are tensor quantities, each governed by 6 independent variables. Normally, the response of a material is measured during loading as in a compression or tension test, giving only one component of the stress tensor. This one-dimensional analysis must then be extrapolated to 6 dimensions to determine the full stress state. If a one-dimensional convex and positive viscoplastic potential function (φ) is defined, then the stress tensor can be determined as [64],

$$\sigma_{ij} = \frac{\partial \varphi}{\partial \dot{\varepsilon}_{ij}}. \tag{6-9}$$

The viscoplastic potential is dependent on the material response.

For many metals the effective (scalar) stress can be determined as

$$\overline{\sigma} = \sqrt{\frac{3}{2} s_{ij} s_{ij}}\ . \tag{6-10}$$

Equation (6-10) is commonly known as the von-Mises stress and is the second invariant of the deviatoric stress tensor. When a metal yields and undergoes plastic deformation the strain must be normal to the yield surface (normality condition). This requires that

$$\dot{\varepsilon}_{ij} = \dot{\lambda} \frac{\partial}{\partial \sigma_{ij}} \left(\overline{\sigma} - \sigma_f \right), \tag{6-11}$$

where λ is the plastic multiplier and σ_f is the material flow stress determined from uniaxial tension tests, as in Eq. (3-6). Substituting Eq. (6-10) into Eq. (6-11) results in [64]

$$\varepsilon_{ij} = \frac{3}{2}\frac{\dot{\bar{\varepsilon}}}{\sigma_f} s_{ij}, \tag{6-12}$$

where the associated effective strain is

$$\dot{\bar{\varepsilon}} = \sqrt{\frac{2}{3}\dot{\varepsilon}_{ij}\dot{\varepsilon}_{ij}} \ . \tag{6-13}$$

6.3 Rigid Viscoplasticity

If the plastic (non-reversible) response of a material is dependent on deformation velocity (or more precisely strain-rate) then it is said to be viscoplastic. A rigid viscoplastic material is dependent on plastic strain and strain-rate, but neglects any elastic response. Thus, there is no yield function and plastic deformation occurs even at very small strains and stresses. Additionally, since no yield surface exists, work hardening (or softening) is not modeled. Under even a small load, the material must deform continuously to an infinite strain, or until the load is removed.

One possibility for the viscoplastic potential of such a material is the Norton-Hoff law [64],

$$\varphi(\varepsilon) = \frac{K}{c+1}\left(\sqrt{3}\dot{\bar{\varepsilon}}\right)^{c+1}, \tag{6-14}$$

where K and c are material parameters. Differentiation of Eq. (6-14) according to Eq. (6-9) results in

$$s_{ij} = 2K\left(\sqrt{3}\dot{\bar{\varepsilon}}\right)^{(c-1)}\dot{\varepsilon}_{ij} = \sigma_{ij} - \frac{1}{3}\sigma_{kk}\delta_{ij}, \tag{6-15}$$

where the deviatoric stress, s_{ij}, in Eq. (6-15) represents the Cauchy stress (σ_{ij}) minus the hydrostatic pressure. It is widely accepted that plastic deformation is independent of hydrostatic pressure [65]. Note that Eq. (6-15) reduces to a Newtonian fluid for $c = 1$ (K is an effective viscosity). Comparison of Eq. (6-12) and (6-15) reveals that the von Misses law is recovered for $c = 0$ (and $K = \sigma_f/\sqrt{3}$). Thus, a viscoplastic material governed by a von Misses flow law can be represented as a non-Newtonian fluid with a strain-rate-dependent viscosity according to Eq. (6-16),

$$\eta = \frac{\sigma_f}{3\dot{\bar{\varepsilon}}}. \tag{6-16}$$

Unlike a fluid, a solid can withstand a finite shear stress without deformation. For example, in FSW only material very near the tool experiences viscoplastic flow, while material outside this region remains rigid and acts essentially as a die wall [9]. However, as the effective viscosity approaches infinity, the deformation rate approaches zero, even with a finite stress. By combining Eq. (3-6) and Eq. (6-16) it can be shown that as $\dot{\bar{\varepsilon}} \rightarrow 0$, the effective viscosity becomes infinite. Therefore, a large increase in viscosity, which occurs at low strain-rates, allows for "solid" regions in the domain. For example, in a fluid model, an increase in η of several orders of magnitude over adjacent material serves to mimic a solid region in the domain. That is, the flowing material, which has a relatively low viscosity, cannot produce the stress needed to deform the outer, relatively soft material. The ability of the effective viscosity in Eq. (6-16) allows for areas of increased viscosity outside the FSW deformation zone, thus simulating a more rigid wall of material.

6.4 Boundary Conditions

To complete the mechanical and thermal model, boundary conditions must be specified at all surfaces. An Eulerian reference frame is employed due to its relative simplicity, computation speed, and ability to model FSW under steady-state conditions. Under such a model the mesh is fixed and the workpiece material flows past a stationary tool. Figure 6-1 is a sketch of the FSW computational domain illustrating model boundaries.

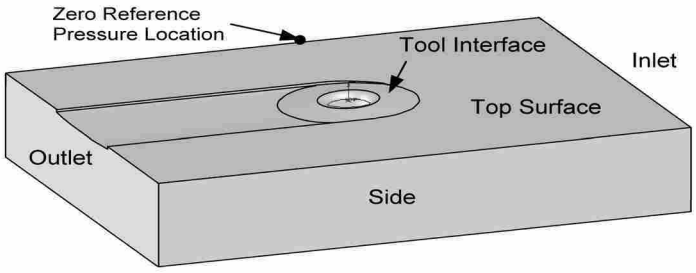

Figure 6-1: Computation Domain and Geometry.

6.4.1 Mechanical Boundary Condition

Aside from the outlet and tool, each of the outer edges of the workpiece can be set to a constant velocity equal to the feed-rate. An outflow boundary condition is specified at the outlet, which imposes a vanishing gradient of all field variables. In FSW, the momentum boundary condition at the tool is typically specified as a known velocity [24, 34, 37] or friction condition [29, 32]. There are many ways to model the momentum boundary condition at the tool interface. Two different boundary conditions are explored in this work:

i. *Constant Velocity.* Under this condition the material adjacent to the rotating tool is assumed to be equal to some fraction, α^*, of the tool's rotational speed (*i.e.*, $v = \alpha^* r\omega$). For this scenario, the flow is set tangent to the tool in the direction of rotation.

ii. *Variable Shear.* This condition allows for material slip at the tool. With the variable shear boundary condition, the shear stress imposed on the material adjacent to the tool is calculated as

$$\tau_v = m^* k_f \left(1 - e^{-\left(\mu\sigma_n / k_f \right)^b} \right)^{1/b}, \tag{6-17}$$

where the shear flow stress $k_f = \sigma_f / \sqrt{3}$, σ_n is the local normal stress, μ is the friction coefficient, and b is a sensitivity constant.

Note that Eq. (6-17) has been previously used successfully in modeling friction conditions in forming operations [66]. If normal forces are large, then Eq. (6-17) simplifies to $\tau_v = m^* k_f$, or a Tresca friction law. It can also be shown from Eq. (6-17) that under small normal forces $\partial\tau_v/\partial\sigma_n = \mu$, which is Coulomb friction. The benefit of the variable shear model is that it allows for regions of both high shear (with presumably substantial material flow) and vanishing shear stress in regions where material is not compressed against the tool.

The shear stress for each case acts in the same direction as the tangential velocity of the tool. Shear stresses acting in the direction of the tool axis are set to zero in this study (*i.e.*, no threads). The normal stress at the tool (σ_n) is determined by separating the deviatoric and hydrostatic stress components according to Eq. (6-15). As discussed

above, the last term on the right-hand-side of Eq. (6-15) is the hydrostatic pressure, which acts normal to the boundary. The remaining deviatoric part only imposes a shear stress at the tool and does not contribute to the normal force. Therefore, the normal stress at the tool in Eq. (6-17) is equivalent to the local hydrostatic pressure.

In solving the differential equations governing momentum and continuity using the fluid-based approach, pressure is relative and only pressure gradients arise in the computational procedure. Therefore, a reference pressure can be specified anywhere in the domain. However, calculation of the shear stress according to Eq. (6-17) for the variable shear model requires accurate prediction of the local pressure. The location of the reference pressure is determined by considering a distributed load on a horizontal surface (*i.e.*, the FSW tool shoulder in contact with the workpiece). The distributed load spreads radially outward under the surface, but stresses at the free surface adjacent to the applied load are zero [67]. Thus, a zero reference pressure could be defined at any point on the top free surface of the workpiece. However, due to the presence of the tool the model predicts a negative pressure gradient from the inlet to the outlet of the domain for any reference pressure location. Additionally, the tool tilt angle and pin will cause additional compressive pressures directly in front of the tool. The small tilt angle would also result in tension (*i.e.,* a negative pressure in the fluid model) directly behind the shoulder at the surface of the workpiece. At some physical location between the leading compression and trailing tension regions, the stress must transition from positive to negative values through a zero stress. Therefore, the ideal location for the zero reference pressure is concluded to be at the top surface along the tool lateral centerline at the far advancing edge of the domain, as indicated in Figure 6-1. The advancing side was

chosen over the retreating edge due to a significant region of compression as material deforms past the retreating side the pin. A simple check of the pressure field (and choice of the zero pressure location) can be made by a comparison of tool forces, since the predicted forces will vary with the reference pressure location specified in the model.

6.4.2 Thermal Boundary Condition

Frictional heating at the tool/material boundary is specified as a variable heat flux, dependent on the tool shear stress (τ) and material velocity as

$$q'' = \gamma\tau(r\omega - v) = \gamma\eta\frac{dv}{dn}(r\omega - v), \tag{6-18}$$

where r is the local tool radius, ω is the angular velocity of the tool, and v is the velocity magnitude of material in contact with the tool. The parameter γ is the fraction of the frictional thermal energy that enters the workpiece, as opposed to the tool. A first-order estimate for γ may be derived from consideration of two dissimilar materials in contact with a point heat source at the interface, as presented by Bastier *et al.* [31],

$$\gamma = \frac{\sqrt{k\rho c_p}_{material}}{\sqrt{k\rho c_p}_{tool}}, \tag{6-19}$$

where it is assumed that more heat enters the tool than the material (if the opposite is true then the ratio is inverted). Experimental studies by Lienert *et al.* [68] have found this relation to be reasonable for FSW.

Equation (6-18) is valid for both the constant velocity and all three shear boundary conditions. Boundary conditions at other locations in the domain are relatively

simplistic, and may include a specified temperature, zero heat flux, or combination of temperature and heat flux (*i.e.*, convection).

The governing energy equation and associated boundary condition at the tool contain velocity gradients and a strain-rate dependent viscosity, which must be determined from solution of the momentum equation. Additionally, temperature-dependent material properties (η, k, and c_p) are included in the momentum conservation equation. Furthermore, each of the shear stress boundary conditions given above are functions of material velocity (or velocity gradients) at the tool and due to the flow stress dependency, the Tresca and variable shear models are also dependent on temperature. The variable shear model is additionally a function of pressure. Therefore, momentum, energy, and both mechanical and thermal boundary conditions at the tool are fully coupled and must be solved simultaneously.

6.5 Model Validation and Specification

Fluent [69] was used to solve the governing equations of momentum and energy conservation in an iterative manner. Fluent is a commercial Eulerian CFD solver that uses the finite volume (rather than the traditional finite element) scheme for discretization. The solver can handle both solid and fluid regions and fully coupled thermomechanical problems. The software permits user definition of complex material viscosity models and boundary conditions. Beginning with guessed distributions for material velocities, temperatures, and dependent thermomechanical material properties, these distributions progress to converged solutions through the course of multiple iterations. The effective viscosity and tool boundary conditions were updated at each

iteration (for the variable shear model). The iteration process was repeated until the local imbalance in each conservation equation was reduced several orders of magnitude (from an initial guess), and the velocity and temperature fields near the tool remained approximately constant with iteration.

To thoroughly examine the different boundary condition models explained previously, detailed experimental data on temperatures and material flow (*i.e.*, velocities, strain-rates, flow paths, *etc*.) must be available. Generally, material velocities and flow patterns are largely unknown in FSW of metals. Material flow features, however, can be readily examined through the use of a plasticine analog where multiple contrasting plasticine colors in the weld piece as detailed in Chapter 5. Also, it was shown in Chapter 4 that embedded steel particles arranged in a grid pattern in the plasticine have allowed measurement of velocities and strain-rates through x-ray imaging. Trends from these material flow visualizations with the plasticine have been found to correspond remarkably well with limited flow studies of metal FSW. These findings provide qualitative flow visualization information as well as quantitative data on material flow velocities, strains, strain-rates, and temperatures during FSW. The extensive experimental data from plasticine FSW presented in the previous chapters is beneficial for validating a numerical model, and therefore, plasticine is used as the workpiece medium in the model presented below. Though not specific to any particular metal, the plasticine provides an idealized model of material flow in FSW.

Recall that properties for this material have been determined for temperatures up to 313 K (92% of melting temperature) and strain-rates up to 5 s^{-1} as noted in chapter 3. Values used for the numerical model are listed again in Table 6-1 along with other

Table 6-1: Constitutive parameters for Van Aken plasticine.

Parameter	Value
strength (k_o)[kPa]	1.82E11
strain sensitivity (n)	0
strain-rate sensitivity (m)	0.18
temperature sensitivity (β)	0.07
shear friction factor (R)	0.95
friction coefficient (μ)	0.57
shear sensitivity (p)	5.0
thermal conductivity (k) [W/mK]	0.65
Specific heat (c_p) [J/kgK]	$-0.216T^2 + 136T + 19{,}900$

constants for the variable shear boundary model (Eq. 6-16). Note that the Van Aken plasticine experiences only slight (if any) strain-hardening. This provides a significant simplification for the numerical model, since strain-hardening effects can be neglected without loss in accuracy. The coefficient of friction, μ, is the upper limit value (von Mises stress) for sticking friction. This value was used for the Coulomb friction due to the somewhat "sticky" nature of the plasticine, especially at higher temperatures. The value of b was arbitrarily selected such that a sharp transition from Coulomb to Tresca friction is modeled. From Chapter 4 it was observed that significant slip occurs between the plasticine and welding tool, and hence, a value of $\alpha^* = 0.1$ was used arbitrarily for the constant velocity model. Such significant material slip has also been estimated in FSW of Al 2024 [10]. Also, recall that Heurtier *et al*. [38] estimated a value of $\alpha^* = 0.01$ for Al 2024. The higher value used in this work is based on slightly higher velocities measured with plasticine [70]. Additionally, a fully sticking boundary condition is modeled (*i.e.*, $\alpha^* = 1$). A perfectly sticking boundary condition is questionable. However, it is investigated here solely for comparative purposes. Note that for the fully sticking scenario material rotates at the velocity of the tool, and according to Eq. (6-18), no direct frictional heating occurs (an unlikely scenario) and all thermal energy

generation is due to deformation heating. Rotational rates of 250 and 1000 rpm were investigated with a constant workpiece feed-rate of 1.1 mm/s. Finally, although the fraction of thermal energy that enters the workpiece (γ) may vary slightly with temperature, the relatively small temperature increases during FSW of plasticine limit the range from $0.1 < \gamma < 0.2$, according to Eq. (6-19). A constant value of $\gamma = 0.2$ was used for both the constant velocity and variable shear model. User defined functions (UDF) for boundary conditions as outlined previously as well as the effective viscosity of plasticine are provided in Appendix D. Additionally, use of the UDF's with Fluent is outlined in Appendix E.

The domain for the model consists of a 10 x 8 x 2 cm material slab containing 45,500 tetrahedral elements, which are clustered near the tool (see Figure 6-1). An investigation using both a coarser (~ 30,000 elements) and a finer (~ 60,000 elements) mesh produced nearly identical results. Approximately 500-1000 iterations were needed to reach a converged solution, which resulted in a computation time of 30-60 minutes on a PC with a 2.40 GHz processor and 512 MB of RAM. The tool has a shoulder diameter of 25.4 mm, a pin (no threads) diameter of 7.7 mm and a length of 7.5 mm. The tool was tilted 2.5 degrees and a concave shoulder (7^o) is modeled. For simplification, the tool itself was not modeled, but represented through appropriate mechanical and thermal boundary conditions. The model geometry was constructed such that the leading edge of the shoulder just contacts the workpiece and the back of the tool is slightly lower than the original surface of the workpiece due to the tool tilt angle. Note that the tool/workpiece arrangement was chosen arbitrarily, but represents a tool depth typical in FSW.

6.6 Model Results and Discussion

In addition to the constant velocity and variable shear models, a Tresca model was also investigated by artificially setting the normal force in Eq. (6-17) to an arbitrarily large value. However, convergence of the governing equations of continuity, momentum, and energy could usually not be achieved. Additionally, it was found that imposing a large constant shear stress value also resulted in divergence. The exact cause of the instability of the model at higher shear stress values (as with the Tresca model) is unclear. As a result only the variable shear stress and constant velocity models have been investigated in detail.

The following discussion on model results is separated into four sections: material flow behavior, which discusses material flow paths, velocities, tool stick/slip, *etc.*; prediction of void formation; material temperature response; and thermal energy sources including direct friction and deformation heating. Recall that the model is evaluated using two rotational speeds of 250 and 1000 rpm, and a single feed-rate (1 mm/s).

6.6.1 Material Flow Behavior

Figure 6-2 shows material flow pathlines for the variable shear stress and constant velocity boundary conditions ($\alpha^* = 0.1$) at the workpiece surface. In the figures, material is fed from right to left and the retreating side is at the lower portion of the figure (*i.e.*, the tool rotation is clockwise). Note that the pathlines are colored by velocity magnitude and the color scales are different for each boundary condition. The tool rotational rate for all

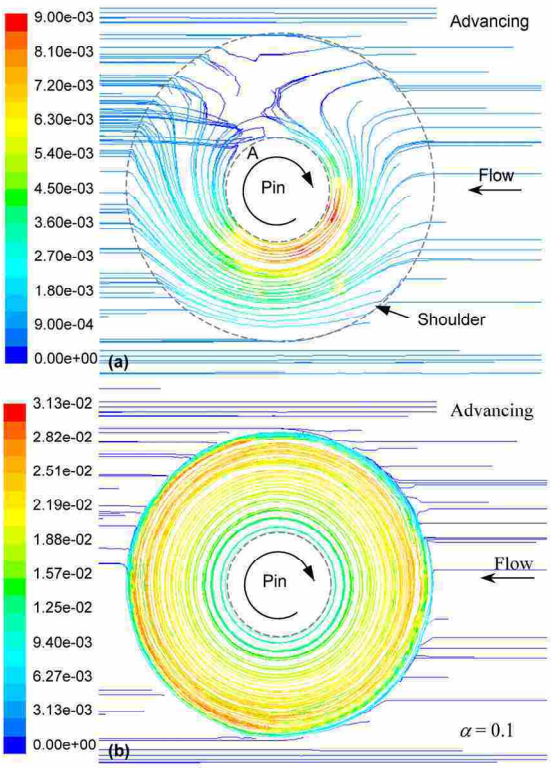

Figure 6-2: Predicted material flow path lines at the shoulder for (a) the variable shear stress boundary, and (b) constant velocity boundary models. Pathlines are colored by velocity magnitude (m/s).

figures is 250 rpm unless stated otherwise. Figure 6-2 shows that the predicted material flow behavior is dramatically different between the two boundary conditions. Of course, for the constant velocity model, the path lines at the shoulder are circular, indicating rotation of material with the tool. This rotating region is absent in the variable shear model, which predicts a more simplistic extrusion behavior. Rather than the dominant rotating region directly under the shoulder that is predicted with the constant velocity model, the variable shear model predicts that material enters the advancing side shoulder region at a velocity equaling the feed-rate, slows and reverses direction near the advancing edge of the pin. At the back of the shoulder, material near the pin diameter is pushed downward (at the location marked "A") and subsequently expelled from the weld

region. As explained previously, maximum velocities with the constant velocity boundary condition are specified at 10% of the tool's tangential speed. For the variable shear stress model, the predicted peak velocity of 9% of the tool's rotational velocity occurs near the pin at the retreating side weld surface. It is interesting that the highest velocity does not occur at the shoulder, indicating more slip at the outer shoulder diameter than at the root of the pin and shoulder. The low material velocity predicted by the variable shear stress model is comparative to predictions by Zhang and Zhang [26] (0 to 17%) as well as numerical results from Buffa *et al.* [71] (5 to 8%).

Figure 6-3 is a photograph (repeated from Chapter 5) of the surface of a stop-action plasticine weld conducted using parameters identical to the numerical model, including tool depth. Recall that this workpiece consists of alternating vertical layers (2 mm thick) of cyan and magenta plasticine, which prevail through the entire thickness of the workpiece (the layers can be observed undeformed at the right side of the image). Notice that the two magenta layers under the leading edge of the shoulder appear virtually undeformed until they approach the rotating region near the pin. Also, cyan material at the retreating side of the shoulder (indicated with a path line in the figure) does not rotate with the tool but simply extrudes past the tool. Material near the pin appears to rotate with the tool as noted by the dark circle of mixed material around the pin diameter. These features suggest that the constant velocity model grossly over-predicts the extent of material flow at the shoulder. Predictions from the variable shear model, however, compare well with the results of the experimental flow visualization study.

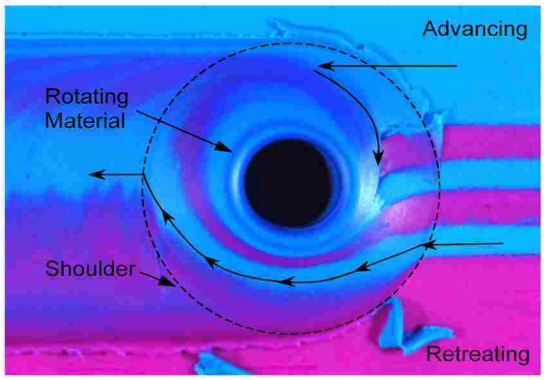

Figure 6-3: Plasticine stop-action weld features at weld surface.

Figure 6-4 shows predicted material flow pathlines at the mid-pin depth for each boundary condition investigated. Note that both plan and side views are provided, and for the side views the tool outline has been indicated to facilitate physical orientation. Each boundary model predicts that as particles deform around the retreating side of the pin they also extrude upward to fill the concave shoulder. This vertical motion is relatively small with $\alpha^* = 0.1$ in Figure 6-4b compared to the other two cases. For the fully sticking case ($\alpha^* = 1$) in Figure 6-4c, the upward flowing material also expands outward near the shoulder. In each case, at the back advancing side of the pin this material is forced downward below its initial vertical location. This downward motion is greatest for the variable shear condition, where material is forced to the bottom of the pin. This vertical flow has been verified in both plasticine in Chapter 4 and aluminum welds [9] under similar operating conditions. An x-ray image of one of the particle lines from Chapter 4 is shown in Figure 6-5 for the same conditions as those simulated, which illustrates the extent of upward deformation. The figure shows that the particles extrude upward at the leading edge of the pin, and are forced downward below the mid-pin depth at the back of the pin. The steel particles are expelled from the weld at the back of the

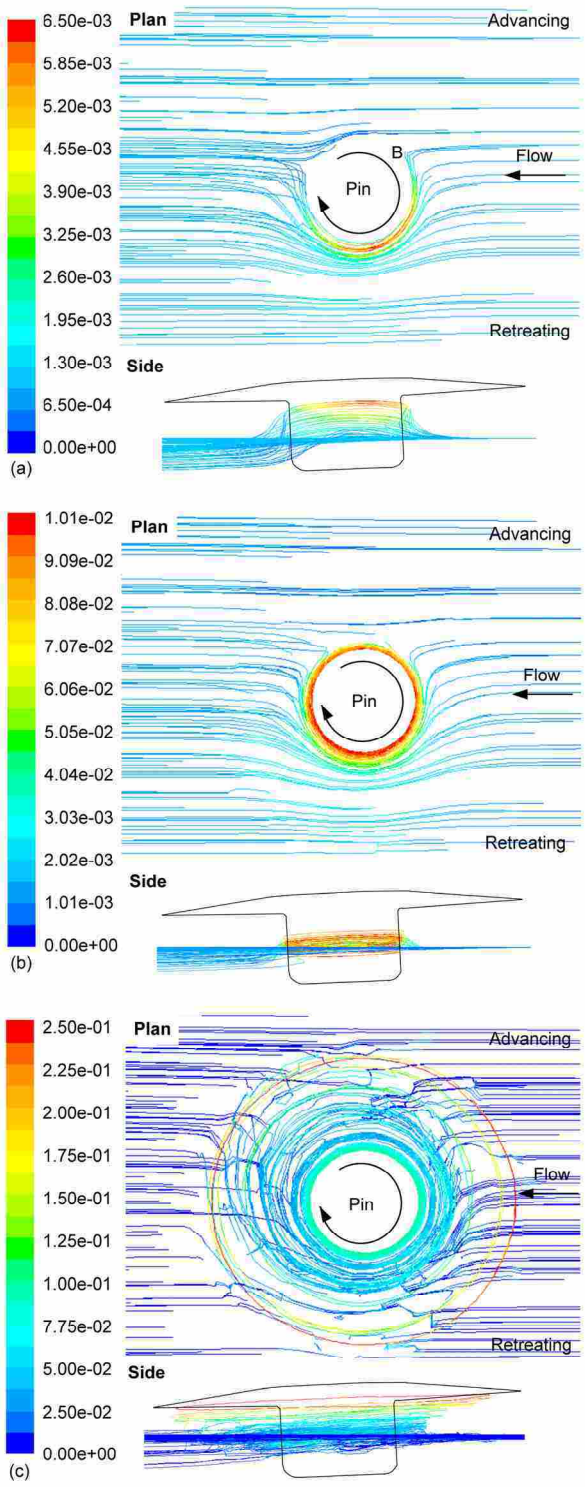

Figure 6-4: Predicted material flow path lines at the mid-pin depth for (a) the variable shear stress boundary, (b) constant velocity $\alpha^* = 0.1$, and (c) constant velocity $\alpha^* = 1.0$ models. Pathlines are colored by velocity magnitude (m/s).

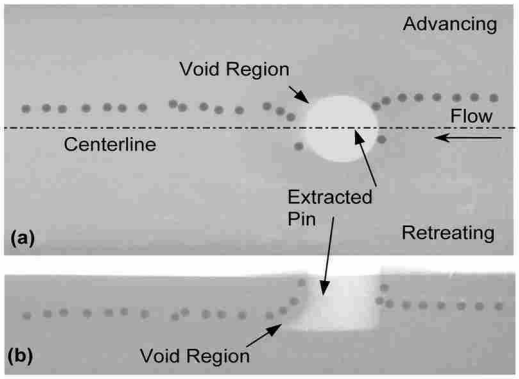

Figure 6-5: X-ray image of steel particle streamline in a stop action plasticine weld, (a) plan view and (b) side view.

pin at the edge of the void region, and similar to the variable shear stress model, no rotation region is observed. Similarities between the void region and the numerical model will be discussed later. Recall that from the spacing of the steel particles, the maximum velocity of this extruding material was estimated at 6% of the rotational pin speed, which is nearly identical to the prediction from the variable shear model of 6.5% at the retreating edge of the pin (Figure 6-4a). Note also in Figure 6-5b, a void region at the bottom trailing edge of the pin is clearly observed.

Returning to the variable shear boundary condition prediction shown in Figure 6-4a, the pathline matching the line of steel particles is identified with the letter "B" in the figure. With the variable shear model, material along this pathline approaches the pin at the advancing edge, contacts the tool, rotates around the retreating side of pin, and is expelled from the weld at approximately $\theta = 210^{o}$ (measured clockwise from the positive x-axis as described in Figure 1-1). As material along this pathline is extruded around the pin it reaches a maximum 6.5% of the pin speed at the retreating side of the pin. At the back advancing side of the pin material velocities decrease to nearly zero. For the constant velocity boundary condition with $\alpha^{*} = 0.1$ (Figure 6-4b), material that

approaches the pin at $y/r_p \approx 1.3$ is entrained in the rotation region adjacent to the pin. Material is expelled from the rotating region at the back of the pin from $\theta = 210 - 260^o$. In contrast to the other boundary conditions, with $\alpha^* = 1$ (Figure 6-4c) much of the material under the shoulder rotates with the tool, and material at a distance of approximately the pin radius ($y/r_p \approx 2.0$) enters this region at the advancing side. Material in the rotating region is expelled at the back advancing side of the pin in a region similar to the $\alpha^* = 0.1$ case.

The deflection of the path lines around the pin for each boundary condition shows that the width of the deformation zone varies around the pin circumference. For the variable shear model (Figure 6-4a) the pathlines at the advancing edge of the pin show relatively little deformation, and velocities remain at nearly the feed-rate. In front of the pin, significant deformation begins at a spacing of approximately 1.5 mm (1/5 of the pin diameter) from the pin. The deformation region is relatively large at the retreating side of the pin, where significant deformation is observed as much as half the pin diameter away from the pin. These predictions agree well with previous experimental findings from Chapter 5. With the constant velocity model in Figure 6-4b ($\alpha^* = 0.1$), the size of the deformation zone is nearly equal to the variable shear model at the leading and retreating sides of the pin. However, material is rotating with the pin in a region approximately 1 mm thick at the advancing edge. This rotating region also persists at the back of the pin, which is not the case for the variable shear model. In Figure 6-4c, the fully sticking constant velocity model ($\alpha^* = 1$) shows a deformation region significantly larger than the other two cases. The outward expansion of material (as discussed above) results in a very large deformation region. Similar pathline plots at greater depths (not shown) reveal that

this behavior persists over much of the pin length, suggesting that for $\alpha^* = 1$, the shoulder affects material deformation deep into the weld. It is only near the pin tip where the influence of the shoulder is no longer dominant for the fully sticking condition.

6.6.2 Void Formation

One of the more important predictions that a FSW model can make is the formation of a void during welding. As stated in the introduction section above, several papers have addressed this issue [27, 29, 32, 37]. A fluids-based model cannot directly predict void formation because fluid continuity is required everywhere in the domain. To circumvent this, He *et al.* [32] have incorporated an additional porosity equation, from which void formation can be inferred. Though such a model is not presented here, the variable shear stress model reveals several features that are suggestive of void formation. First, as discussed above in Figure 6-4a, velocities at the back advancing edge of the pin approach zero. A plot of the predicted pressure field at the mid-pin depth and pressure-dependent tool shear stress is provided in Figure 6-6. Only positive pressures are plotted in the figure in order to reveal the region where material is not pressed against the tool. Recall that only gradients of pressure are important in a fluids-based model. Based on a point source force contact assessment, however, the top surface far from the tool should be stress-free [67]. Thus a zero reference pressure was set at the far advancing side of the domain as shown in Figure 6-1. This implication can be verified by comparing the vertical force at the tool between experiment and model since this force is a function of material pressure under the tool. Under identical operating conditions as the model, experiments show that the tool vertical force during plasticine welding is typically 35 to

60 N, depending on tool depth. The variable shear model predicts a tool vertical force of 62 N, which is reasonable. Separate models were also evaluated with the reference pressure at the inlet and at the outlet (at the top surface centerline). The resulting vertical force for these conditions was 35 and 167 N, respectively.

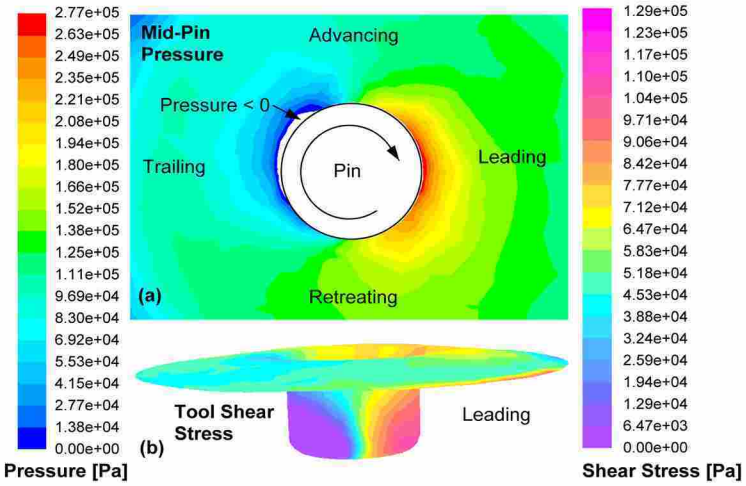

Figure 6-6: Predicted pressure (mid-pin depth) (a) and shear stress (tool) (b) from the variable shear stress model for 250 rpm rotational speed.

With the pressure field adequately defined, the shear stresses at the tool can be calculated. Figure 6-6b shows that the predicted shear stress at the lower rear portion of the pin is zero. The implication of the zero shear stress is that material in this region is mechanically "detached" from the pin where the tool imparts no force to the material. These three indicators (diminishing velocities, negative pressure region, and vanishing friction at the interface) provide evidence that a void may develop in the weld.

As discussed above, a void is observed behind the pin in Figure 6-5. The location of the void behind the extracted pin location corresponds well with the region of diminishing velocity, pressure, and shear stress predicted by the model for the variable

shear stress boundary condition. In the x-ray image, the void only exists directly behind the pin and closes completely at approximately one pin radius downstream. At this location the workpiece must be experiencing compression (since tension cannot close a void), and the pressure field in Figure 6-6a shows a corresponding increase in pressure.

Of course, for the constant velocity boundary condition, material flow around the entire periphery of the tool is significant (Figure 6-4b,c) and thus, formation of a void is not expected. Additionally, the pressure and shear stress plot for the constant velocity conditions in Figure 6-7 shows a positive pressure and shear stress around the entire tool.

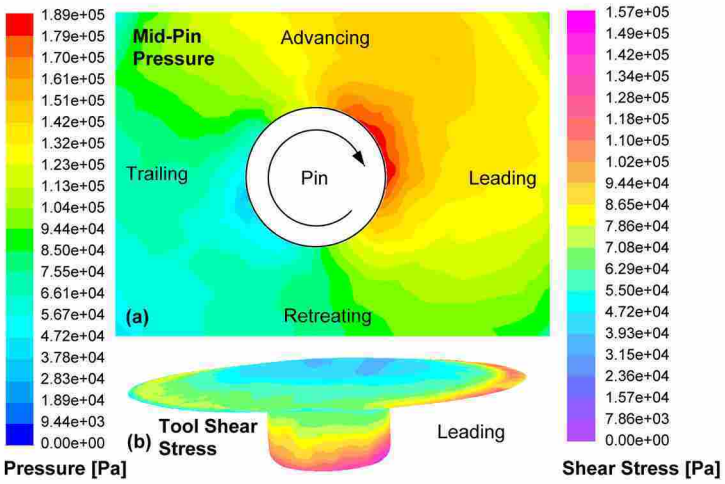

Figure 6-7: Predicted pressure (mid-pin depth) (a) and shear stress (tool) (b) from the variable shear stress model for 1000 rpm rotational speed.

In addition to 250 rpm, a tool rotational rate of 1000 rpm was simulated with the computational model. Experiments from Chapter 5 show significant deformation of the plasticine and a rotating region near the shoulder at high rotational rate, which is in contrast to the primary extrusion flow at 250 rpm. Of course, material velocities with the constant velocity model increase directly with an increase in tool rotational rate.

However, increasing the tool rotational rate to 1000 rpm with the variable shear model does not have a significant effect on material flow features. The increase in rotational rate does, however, result in large temperature increases (which are discussed below) in the weld region. The consequence of this temperature increase is a decrease in the material flow stress according to Eq. (3-6). This decrease in flow stress causes the shear stress to also decrease as specified by Eq. (3-7) and Eq. (6-17). Thus, for the variable shear stress model the flow field remains essentially unchanged with increasing rotational rate. It may be that in reality there is some direct adhesion of the plasticine to the tool, which is neglected in the variable shear model. This adhesion would serve to produce a sticking boundary condition at higher rotational speeds, and correspondingly higher material velocities. The adhesive force was estimated by lightly pressing a known weight of the plasticine to a flat steel surface of known surface area. Additional plasticine was added until the material fell off the steel surface under the force of gravity. The total weight of the plasticine was then measured and divided by the steel contact surface area to determine the adhesive stress. These preliminary experiments showed that the adhesive stress between the plasticine and steel is on the order of 10 kPa. At relatively low temperatures, the flow stress of the plasticine is 100 – 200 kPa depending on strain-rates (see Chapter 3). However, the flow stress decreases to values less than 50 kPa at temperatures above 320K. If the flow stress is on the order of the adhesive force then the tool/material interface would tend to a sticking condition. It therefore appears that the variable shear boundary model as currently constituted is only valid for materials and operating conditions where the flow is primarily one of simple extrusion.

6.6.3 Material Temperature Response

Predicted temperature contours are shown in Figure 6-8 for the variable shear stress and constant velocity boundary condition models (for both $\alpha^* = 0.1$ and $\alpha^* = 1$) at the surface and mid-pin depth. For the variable shear model, the highest temperature

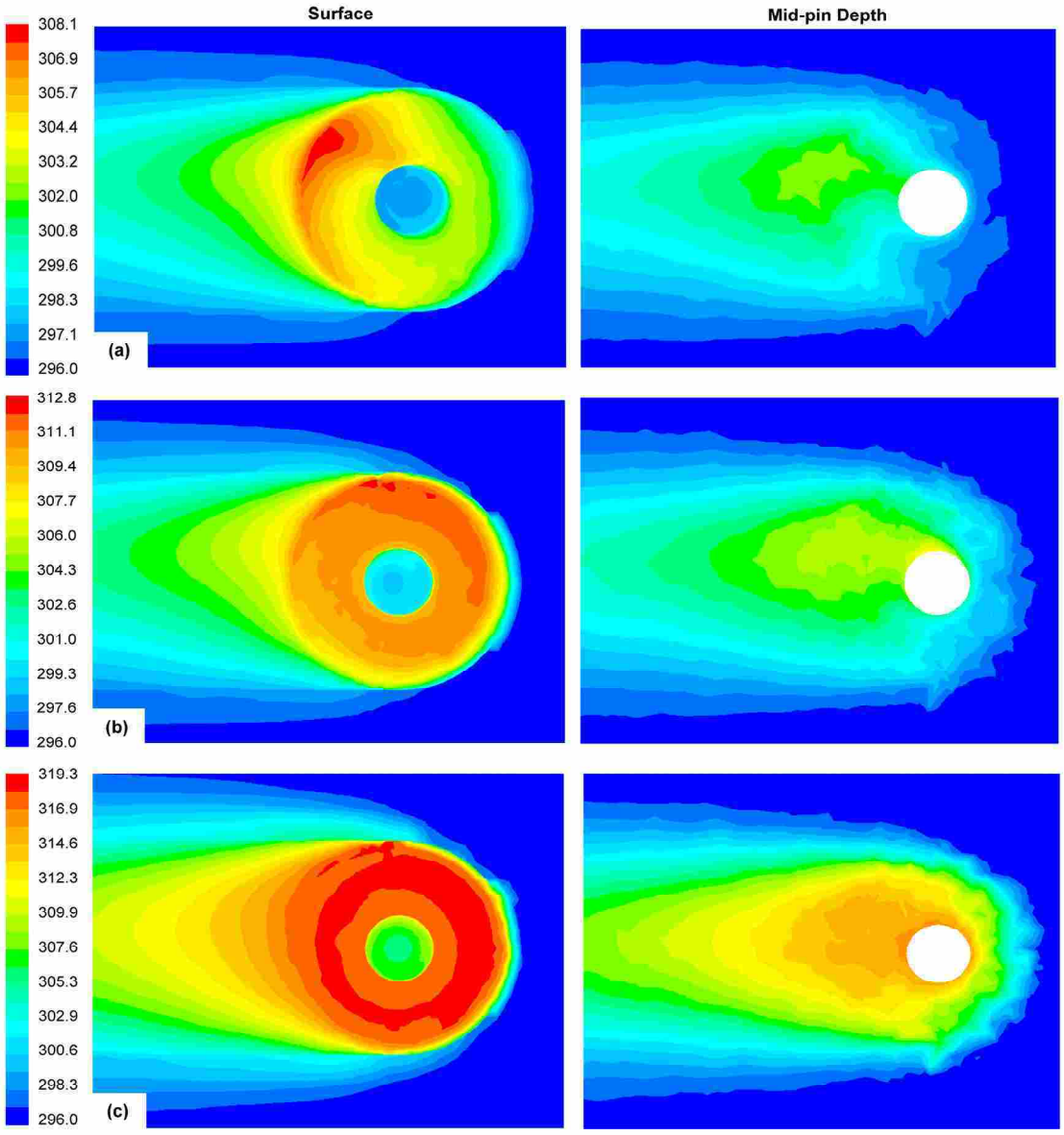

Figure 6-8: Predicted temperature (K) contours at the surface and mid-pin depth for the (a) variable shear stress model, (b) constant velocity model with $\alpha^* = 0.1$, and (c) constant velocity model with $\alpha^* = 1.0$.

occurs at the back advancing side of the shoulder. The highest temperature for the constant velocity model with $\alpha^* = 0.1$ is at the advancing side edge of the shoulder. The peak temperature is higher for the constant velocity model (313 K) compared to the variable shear model (308 K). For the case of $\alpha^* = 1$ where all thermal energy input is due to deformation heating, the peak temperature in the weld is 319 K, which occurs nearly uniformly over the entire shoulder region. This relatively high temperature indicates substantial deformation heating in the upper region of the weld. At the mid-pin depth, the constant velocity model with $\alpha^* = 0.1$ predicts a relatively high temperature at the advancing edge of the pin. However, the variable shear model shows a region slightly downstream of the pin with a temperature higher than at the pin surface (at the mid-pin depth).

Thermocouple data from plasticine weld experiments, along with predicted temperatures from each boundary condition are shown in Figure 6-9. In the experiment, four K-type thermocouples were placed at the advancing and retreating sides of the pin at the mid-pin depth at specified locations relative to the centerline. The transverse locations of each thermocouple are specified in the figure. The thermocouple measurements show the maximum temperature experienced by the thermocouple during the weld, which may occur slightly upstream or downstream of the pin. Generally, the thermocouple data and variable shear stress model are in good agreement. Both constant velocity models with $\alpha^* = 0.1$ and 1.0 are hotter than the measured values. For $\alpha^* = 0.01$, the predicted temperatures at the retreating side are nearly identical to the measured values. However, temperatures at the advancing side are underestimated and the variable shear stress model is more accurate.

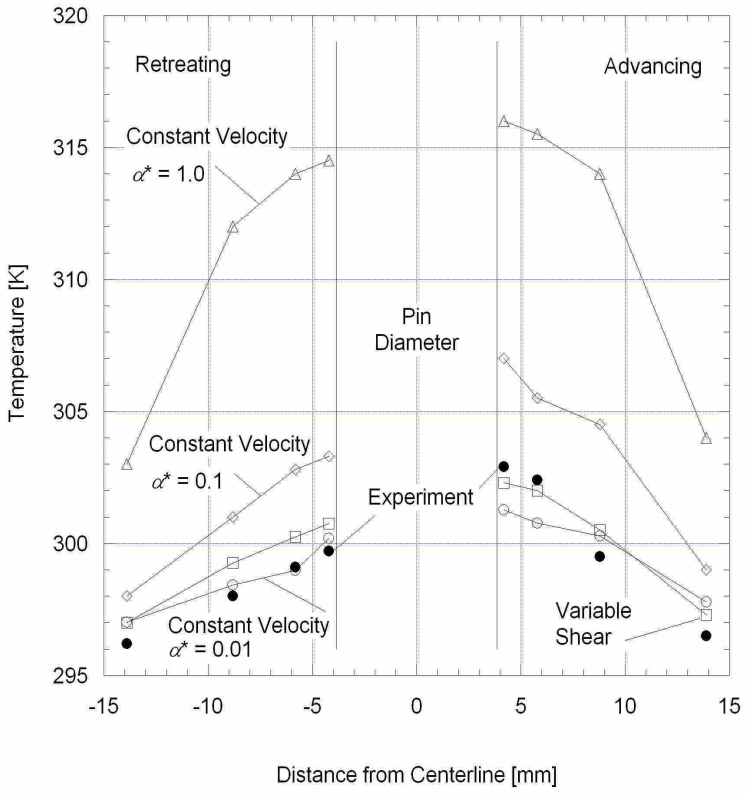

Figure 6-9: Peak temperatures near the pin during plasticine FSW for 250 rpm rotational speed.

It should be noted, however, that predicted temperatures and strain-rates (over 100 s^{-1}) for the α^* = 1.0 (tool speed of 250 rpm) conditions are higher than those measured for the material constitutive model (Chapter 3), and thus a considerable extrapolation must be employed to estimate the flow stress. With α^* = 0.1, the highest predicted temperature is within the measured range for the flow stress model, but predicted strain-rates can be as high as 30 s^{-1} at the shoulder diameter. Although the strain-rate is substantially higher than values investigated for the flow stress model, it is believed that extrapolation to higher strain-rates is not as severe as extrapolating to temperatures near the material's melting point. For the variable shear model, the maximum predicted temperature is within the measured flow stress range and the largest

strain-rate is 6 s^{-1}, which occurs at the shoulder where the velocity is maximum. Experimentally, the strain-rate during FSW of the plasticine has been previously measured at 1.3 s^{-1} [70]. Note that predictions by Buffa *et al*. [72] similarly show maximum strain-rates of only 4 s^{-1} for a smooth pin. Given that the experimental value is an average over a relatively large area, the prediction from the variable shear model appears reasonable.

Although it has been shown previously that the variable shear stress model may be inaccurate at high rotational rate, weld temperatures from the model at 1000 rpm are briefly discussed solely for comparative purposes with the constant velocity boundary condition. Figure 6-10 shows predicted temperatures at the mid-pin depth on either side of the pin for each model. Note that for the constant velocity case, temperatures are plotted for $\alpha^* = 0.01$ and 1.0. Even with the material velocity at only 1% of the tool speed, temperatures are slightly above those predicted by the variable shear model. As with the 250 rpm case, the highest temperature is at the advancing side of the pin. The peak mid-pin temperature for the variable shear model is 310 K. At the surface the highest temperature is 321 K (not shown in the figure). For the variable shear model, the temperature increase from the 250 rpm case is due to a larger velocity discontinuity between the tool and material as described above, which results in a greater heat flux at the tool according to Eq. (6-18). Temperatures also increase for the constant velocity model at 1000 rpm. For $\alpha^* = 0.01$, the maximum temperature at the shoulder is 327 K and at the mid-pin temperatures approach 315 K. For $\alpha^* = 1$, temperatures are as high as 342 K and 335 K at the shoulder and mid-pin, respectively. These temperatures are above the range in which the flow stress was measured, and are at or within a few percent

of the material's melting temperature. The extrapolation of material properties very near the melting point makes the numerical solution for the $\alpha^* = 1$ case questionable. However, the increasing temperature trend with increasing α^* is expected. Thermocouple measurements from Chapter 2 reveal that the maximum mid-pin temperature at 1500 rpm is 318 K. At 1000 rpm the peak mid-pin temperature should be less than this value. Therefore, it can be concluded that even at 1000 rpm there is some tool/material slip, though it is likely not as significant as what the variable shear model predicts. The extreme temperatures from the completely sticking boundary model ($\alpha^* = 1$), however, show that this assumption can lead to a significant error in FSW predictions.

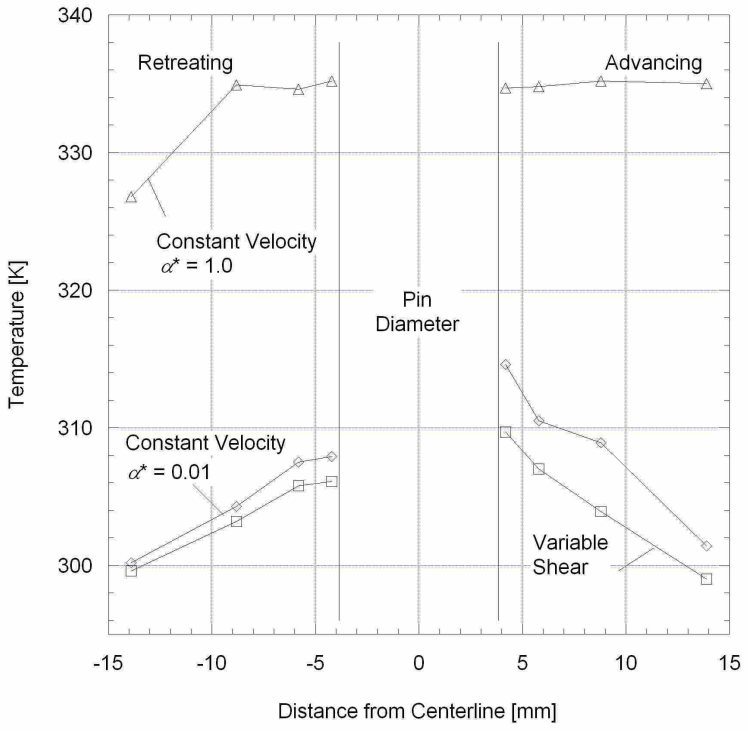

Figure 6-10: Peak temperatures near the pin during plasticine FSW for 1000 rpm rotational speed.

6.6.4 Thermal Energy Sources

One area of current discussion in FSW concerns the ratio of direct friction heating to deformation or viscous heating. Recall from Chapter 3 that deformation heating is dependent on the product of the Prandtl and Eckert numbers ($PrEc = \eta u^2/k\Delta T$). The Prandtl number is the ratio of momentum and thermal diffusivities, and the Eckert number is the ratio of the kinetic energy of the flow to the boundary layer and far field enthalpy difference. Deformation heating can be totally neglected without loss in accuracy if $PrEc << 1$. If a characteristic strain-rate is approximated from the speed of the deforming material at the tool (u) and the width of the deformation region (l), then the effective viscosity, η, can be determined where $\eta = \sigma l/3u$. Characteristic values and the resulting $PrEc$ for the constant velocity ($\alpha^* = 0.1$) and the variable shear boundary conditions are provided in Table 6-2 (250 rpm).

Table 6-2: Characteristic values and dimensionless Prandtl-Eckert number product for the constant velocity ($\alpha^* = 0.1$) and variable shear stress boundary conditions at 250 rpm. Deformation heating is negligible for PrEc <<1.

Parameter	Constant Velocity	Variable Shear
material velocity (u) [mm/s]	10	6.5
deformation zone width (l) [mm]	1.5	1.5
flow stress (σ) [kPa]	81	107
temperature difference (ΔT) [K]	10	5
$PrEc$	0.06	0.11

Each value is estimated from the corresponding numerical model (ΔT is the temperature difference between material in contact with the pin and material outside the weld region) at the mid-pin depth. The data illustrate that for both the variable shear and constant velocity ($\alpha^* = 0.1$) models, deformation heating could be neglected without

significantly affecting the model predictions. In fact, a solution without accounting for viscous heating simulated as part of this study was found to produce results identical to those discussed above. This is due to the substantial slip predicted by the model (or imposed in the constant velocity model with $\alpha^* = 0.1$). If the material completely sticks to the tool the maximum velocity at the outer edge of the shoulder (25.4 mm diameter) would be 33 mm/s at 250 rpm. Assuming all other characteristic values identical to the constant velocity case with $\alpha^* = 0.1$ results in $PrEc = 1.2$, and deformation heating cannot be neglected.

Figure 6-11 shows the trade-off between deformation and direct frictional heating at the tool for the 250 rpm rotational rate. Note that the volumetric deformation-heating source has been integrated over the entire domain, and the direct frictional heating is integrated over the entire tool surface area. Recall from Eq. (6-18) that the direct frictional heating is a function of tool/material slip and tool shear stress. Therefore, the area-weighted average tool shear stress is also plotted in Figure 6-11. As expected, deformation heating is greatest under a sticking scenario but vanishes as $\alpha^* \rightarrow 0$. Generally, direct frictional heating exhibits the opposite behavior. However, at $\alpha^* < 0.05$ the frictional heating decreases, likely due to a decreasing shear stress as noted in the figure. Another interesting observation is that the maximum value for deformation heating is much larger than the maximum heat input from direct frictional heating at the tool. Thus, even though there is no heat input from the tool with $\alpha^* = 1$, temperatures are much higher than the $\alpha^* = 0.1$ scenario as discussed above. At $\alpha^* = 0.1$, frictional heating is larger than deformation heating, but from the figure, both sources appear to be on the same order of magnitude. However, the deformation heat source is calculated by

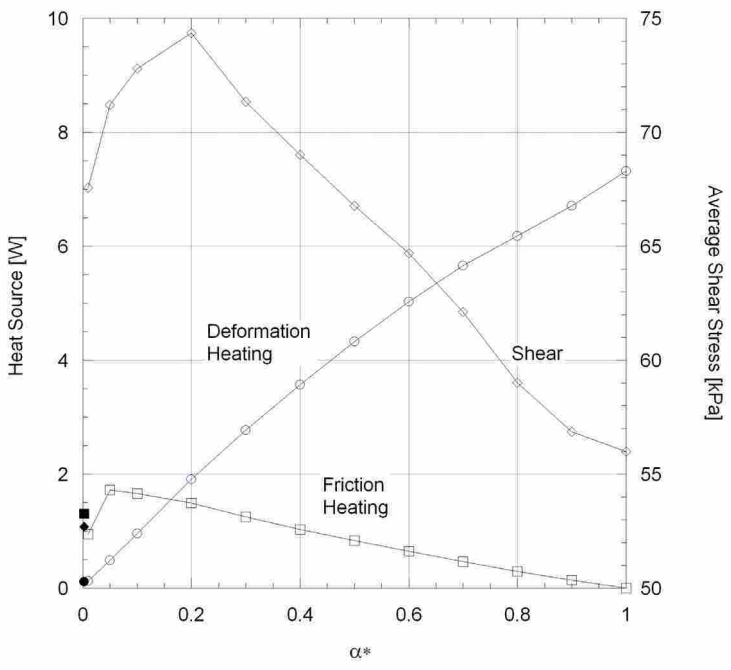

Figure 6-11: Heat source and average tool shear stress as a function of percentage tool/material stick for the 250 rpm rotational speed. Curves are predictions from the constant velocity model and solid points along the left axis are predictions from the variable shear model.

multiplying very small velocity gradients in the far field by the effective viscosity, a very large value in the far field. The multiplication of a very small value by a very large value results in a slight over-prediction of the deformation heat source since velocity gradients away from the tool are in reality identically zero. This error in the far field results in an additive increase in the total deformation source in the energy equation. However, since this source is spread over the entire domain, additional heating at the tool is negligible, as found by the simulation omitting the source term entirely as discussed above. From the figure, it appears that at 250 rpm, deformation heating only becomes important for $\alpha^* >$ 0.2. Results for the variable shear model are plotted at the left side of the figure as solid symbols. The shape of the symbol corresponds to the marker shape for the constant velocity model for the shear stress, frictional heating, and deformation heating,

respectively. The predicted heating source terms correspond relatively well with values from the constant velocity model with $\alpha^* \rightarrow 0$. However, the average shear stress is much lower than predicted by the constant velocity model since the shear stress at the back of the pin is zero as shown in Figure 6-6b.

A similar plot is shown in Figure 6-12 for the 1000 rpm rotational rate. Results for the 1000 rpm case are generally similar to the 250 rpm speed where deformation heating is minimal at very low α^*, but increase substantially as α^* increases. However, unlike the 250 rpm case, the velocity difference between the tool and material is such that even the small decrease in shear stress at low α^* is not enough to reduce the extent of frictional heating. Additionally, both the frictional and deformation heating sources are significantly larger than the low rotational speed, which accounts for the higher temperatures for the 1000 rpm speed, as discussed above. However, the average shear stress is lower at 1000 rpm than 250 rpm for the entire range of stick percent due to increased temperatures and a softer material near the tool. The higher heat sources suggest that generally deformation heating should not be neglected even at low α^* values, except perhaps for $\alpha^* < 0.05$. Corresponding values for the variable shear stress model are shown at the left side of the figure. Notice that deformation heating is essentially zero and frictional heating and average tool shear are both lower than the constant velocity model.

In summary, comparison with experimental data suggests that the variable shear model is superior to a sticking condition. While the constant velocity model predicts a region of material that rotates with the tool, material flow predicted by the variable shear

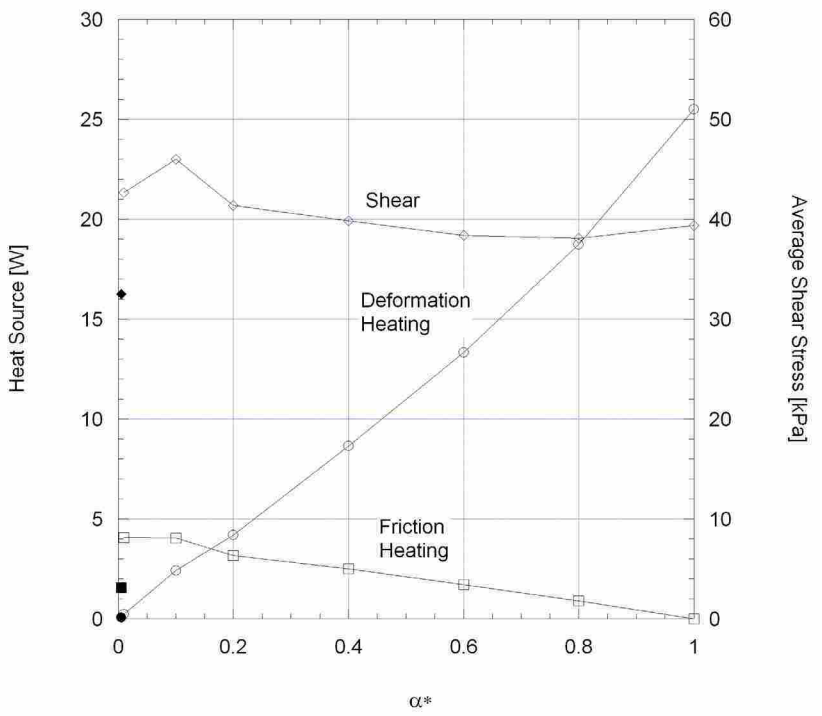

Figure 6-12: Heat source and average tool shear stress as a function of tool/material stick percent for the 1000 rpm rotational speed. Curves are predictions from the constant velocity model and solid points along the left axis are predictions from the variable shear model.

stress model is primarily one of simple extrusion with maximum velocities of only 9% of the tool speed. Additionally, the variable shear model implies formation of a void region at the back of the pin. These material flow trends from the variable shear model correspond well with experimental findings at 250 rpm. Predicted material temperatures for the variable shear stress model also compare well to experimentally measured values at 250 rpm. However, increasing the rotational rate to 1000 rpm substantially increases material temperatures but does not result in any significant difference in the material flow field for the variable shear model. This discrepancy is attributed to direct tool/material adhesion, which cannot be neglected at high temperatures where the flow stress is on the

order of the adhesive force. Inclusion of this adhesive force in the boundary condition may produce more accurate results.

7 Conclusions

The thermomechanical behavior of plasticine during FSW has been investigated and compared to welds conducted in metals. Many flow features that are thought to occur in FSW of metals are also observed in the plasticine. For example, depending on the welding tool and operational parameters the following material flow characteristics can be achieved: a simplistic extrusion type flow, rotational flow with macroscopic mixing, vertical deformation into the concave shoulder cavity, and downward flow due to pin threads. Also, typical defects that occur in metals can also occur (and be avoided) with the plasticine such as void formation and flash generation. In addition to general material flow patterns, the thermal response of the plasticine under relatively "hot" and "cold" processing conditions is qualitatively similar to metals.

Criteria for rigorous similarity between the plasticine and metals have also been expressed quantitatively. Five separate parameters were identified that must be matched between the plasticine model material and the actual metal. These parameters are:

i. *Material flow stress* – the ratio of the flow stress between the plasticine and any metal must be constant. This requires that the strain, strain-rate, and temperature (over the range of process temperatures) sensitivities of the plasticine and metal be identical.

ii. *Shear friction factor* – the shear friction factor for both the model and actual material must be identical.

iii. *Peclet number* – the dimensionless ratio of thermal convection to diffusion must be identical between the two materials.

v. *Prandtl-Eckert product* – this dimensionless parameter describes the magnitude of deformation heating and must be identical between each *material.*

vi. *Direct frictional heating* – the dimensionless heat input at the tool/material interface due to direct friction heating must be matched for both materials.

Similarity in each of these parameters can be achieved by adjusting the tool rotational speed and/or pin diameter except for the Peclet number. Since most metals are much more apt to conduct heat compared to the plasticine, exact similarity cannot be achieved. However, the ability to match all other parameters (at least approximately) and the visually observed mechanical and thermal similarities suggest that similarity can be achieved at least qualitatively, and general FSW trends in plasticine can be extrapolated to FSW of metals.

Material flow visualization and measurement studies with the plasticine were conducted by using a stop-action technique where the forward motion of the tool is suddenly suspended and raised from the workpiece. After stop-action, the plasticine workpiece, which typically consisted of several contrasting layers of clay, was cut in sections around the extracted tool location to visually inspect material flow patterns. Detailed studies were conducted at tool rotational speeds of 250 and 1000 rpm, a feed rate of 1.1 mm/s, varying tool depth, and both a smooth and threaded pin tool (concave tool shoulder with 2.5^{o} tilt).

The following summarizing conclusions can be made concerning material flow in FSW. Note that these observations are general and might also be extrapolated to FSW of metals due to plasticine/metal similarity:

Smooth Pin

i. Significant tool slip and a simplified extrusion type flow with no material rotation region can occur during FSW with a smooth pin. At the mid-pin depth, material velocities during FSW are only a few percent of the tool speed. (This result, however, is dependent on workpiece material and welding tool.) Generally, the mechanical stick/slip tool boundary condition is independent of tool rotational rate. Any void defect provides evidence that slip occurs at the tool interface. This observation, however, is not commutative. That is, it is possible for some slip to occur without void formation.

ii. Material extrudes upward at the retreating side of the pin to fill the concave shoulder region. This upward motion is essentially independent of rotational rate, and can be as much as half the pin length. At the advancing side of the pin, material remains at nearly its initial vertical location in the workpiece as it extrudes past the pin. As the weld finishes, material that extruded upward is forced back to or even below its initial vertical position. Material at the upper half of the advancing side of the weld is forced to the bottom of the pin at the trailing edge of the shoulder to fill any low pressure (*i.e.*, void) region.

iii. Material rotation with the tool directly under the shoulder is highly sensitive to tool depth. If the depth is too shallow a channel forms in the workpiece downstream of the tool. This channel can be closed completely

by increasing the tool plunge depth. Under this scenario no rotating occurs at the shoulder. Further increasing the tool depth results in rotating and macroscopic mixing of advancing and retreating workpiece sides at the shoulder. If the depth is further increased, flash appears at the surface and extensive material mixing can occur over half the pin depth at high rotational rates. At low rotational speeds, however, increasing the tool depth to the point of flash generation only has a minimal effect on mixing and material rotation in the welded region.

Threaded Pin

i. At all rotational rates investigated, material becomes entrained inside the pin threads and rotates with the tool. Except near the shoulder, rotating material is generally comprised only of material from the advancing side of the weld centerline. Entrained material inside the threads is either deposited cyclically with non-rotating material from the retreating side of the pin (this periodicity is equal to the weld pitch), or is forced under the pin.

ii. The downwash of the threads causes material just outside the threads to deform upward on both the advancing and retreating sides of the pin. Similar to the smooth pin, this material is forced downward to its initial vertical location at the trailing edge of the shoulder.

iii. As with the smooth pin, material rotation with the tool shoulder at the surface of the weld is highly dependent on tool depth. However, at the point of flash generation with a high rotational rate, the influence of pin threads causes material to rotate with the tool over the entire depth of the weld and even in a small region below the pin. Increasing the tool depth

with the threaded pin also results in a substantial increase in vertical motion and mixing in the weld. With a low tool rotational rate, material rotating and mixing is much less apparent, even at an increased tool depth, except very near the surface.

Experimental findings for the smooth pin tool were further investigated and validated in a three-dimensional numerical model. Both a sticking constant velocity and slipping variable shear stress boundary model were employed. The variable shear stress model includes both Coulomb and limiting Tresca friction. Comparison with experimental data suggests that the variable shear model is superior to a sticking condition. While the constant velocity model predicts a region of material rotation with the tool, material flow predicted by the variable shear stress model is primarily one of simple extrusion. The variable shear model estimates that the maximum velocity of the weld material is only 9% of the tool's rotational speed. The variable shear model also suggests formation of a void region behind the pin. This void is attributed to insufficient contact and vanishing frictional force between the material and tool. These material flow trends from the variable shear model correspond well with experimental findings at 250 rpm. Predicted material temperatures from the variable shear stress model match well with experimentally measured values. Assuming a constant material velocity at the tool of 10% and 100% of the tool rotational speed, however, results in temperatures higher than experimental data. Increasing the rotational rate to 1000 rpm substantially increases material temperatures but does not result in any significant difference in the material flow field for the variable shear model. This discrepancy is attributed to direct tool/material adhesion, which cannot be neglected at high temperatures where the flow stress is on the

order of the tool/material adhesive force. Inclusion of this adhesive force in the boundary condition is an area for future investigation.

8 References

1. Mahoney, M.W., Rhodes, C.G., Flintoff, J.G., Spurling, R.A., Bingel, W.H., Properties of friction-stir-welded 7075 T651 aluminum, *Metall. Mater. Trans. A* 29 (1998) 1955-1964.

2. Cantin, G.M.D., David, S.A., Thomas, W.M., Lara-Curzio, E., Babu, S.S., Friction Skew-stir welding of lap joints in 5083-0 aluminum, *Sci. Technol. Weld. Joining* 10 (2005) 268-280.

3. Li, Y., Murr, L.E., McClure, J.C., Flow visualization and residual microstructures associated with the friction-stir welding of 2024 aluminum to 6061 aluminum, *Mater. Sci. Eng. A* 271 (1999) 213-223.

4. Murr, L.E., Li, Y., Flores, R.D., Trillo, E.A., McClure, J.C., Intercalation vortices and related microstructural features in the friction-stir welding of dissimilar metals, *Mater. Res. Innov.* 2 (1998) 150-163.

5. Ouyang, J.H. and Kovacevic, R., Material flow and microstructure in the friction stir butt welds of the same and dissimilar aluminum alloys, *J. Mater. Eng. Perform.* 11 (2002) 51-63.

6. Reynolds, A.P., Visualization of material flow in autogenous friction stir welds, *Sci. Technol. Weld. Joining* 5 (2000) 120-124.

7. Seidel, T.U. and Reynolds, A.P., Visualization of the material flow in AA2195 friction-stir welds using a marker insert technique, *Metall. Mater. Trans. A* 32 (2001) 2879-2884.

8. Guerra, A., Schmidt, C., McClure, J.C., Murr, L.E., Nunes, A.C., Flow patterns during friction stir welding, *Mater. Charact.* 49 (2002) 95-101.

9. Colligan, K., Material flow behavior during friction stir welding of aluminum, *Weld. J.* 78 (1999) 229s-237s.

10. Schmidt, H.N.B., Dickerson, T.L., Hattel, J.H., Material flow in butt friction stir welds in AA2024-T3, *Acta Mater.* 54 (2006) 1199-1209.

11. White, F.M., Viscous Fluid Flow, 2nd ed., McGraw-Hill, New York, 1991.

12. Gerlich, A., Avramovic-Cingara, G., North, T.H., Stir zone microstructure and strain rate during Al 7075-T6 friction stir spot welding, *Met. Mater. Trans. A* 37A (2006) 2773-2786.

13. Gerlich, A., Yamamoto, M., North, T.H., Strain rates and grain growth in Al 5754 and Al 6061 friction stir spot welds, *Met. Mater. Trans. A* 38 (2007) 1291-1302.

14. Frigaard, O., Grong, O., Hjelen, J., Gulbrandsen-Dahl, S., Midling, O.T., Characterisation of the subgrain structure in firction stir welded aluminium alloys using the SEM-EBSD technique, Proc. 1st Inter. Symp. Friction Stir Welding, The Welding Institute, Thousand Oaks, CA, 1999.

15. Kim, Y.G., Fujii, H., Tsumura, T., Komazaki, T., Nakata, K., Three defect types in friction stir welding of aluminum die casting alloy, *Mater. Sci. Eng. A* 415 (2006) 250-254.

16. Schey, J.A., Introduction to Manufacturing Processes, 2nd ed., McGraw-Hill, New York, 1987.

17. Kazi, S.H. and Murr, L.E., Complex flow phenomena associated with friction-stir-welding of aluminum alloys, in: K.V. Jata, et al. (Eds), Friction stir welding and processing, TMS, Warrendale, PA, 2001, pp. 139-150.

18. Nowak, B.M., Hall, A.C., Knorovsky, G.A., High-speed video flow visualization in friction stir welds of polycarbonate, 6th International trends in welding research, (Eds) ASM International, Pine Mountain, GA, 2002, 224-228.

19. Wanheim, T., Schreiber, M.P., Gronbaek, J., Danckert, J., Physical modelling of metal forming processes, *J. App. Metal Working* 1 (1980) 5-14.

20. Aydin, I., Biglari, F.R., Briscoe, B.J., Lawrence, C.J., Adams, M.J., Physical and numerical modelling of ram extrusion of paste materials: conical die entry case, *Comp. Mater. Sci.* 18 (2000) 141-155.

21. Green, A.P., The use of plasticine models to simulate the plastic flow of metals, *Phil. Mag.* 42 (1951) 365-373.

22. Kawai, M. and Kamishohara, K., The use of plastalina models to simulate the stress in metals under plastic deformation, International Forging Conference, (Eds), Paris, France, 1975, 571-595.

23. Sofuoglu, H. and Gedikli, H., Physical and numerical analysis of three dimensional extrusion process, *Comp. Mater. Sci.* 31 (2004) 113-124.

24. Colegrove, P.A. and Shercliff, H.R., 3-Dimensional CFD modelling of flow round a threaded friction stir welding tool profile, *J. Mater. Process. Technol.* 169 (2005) 320-327.

25. Seidel, T.U. and Reynolds, A.P., Two-dimensional friction stir welding process model based on fluid mechanics, *Sci. Technol. Weld. Joining* 8 (2003) 175-183.

26. Zhang, H. and Zhang, Z., Numerical modeling of friction stir welding processes by using rate-dependent constitutive model, *J. Mater. Sci. Technol.* 23 (2007) 73-80.

27. Chen, C.M. and Kovacevic, R., Finite element modeling of firction stir welding - thermal and thermomechanical analysis, *Int. J. Mach. Tools Manuf.* 43 (2003) 1319-1326.

28. Buffa, G., Hua, J., Shivpuri, R., Fratini, L., A continuum based FEM model for friction stir welding - model development, *Mat. Sci. Eng. A* 419 (2006) 389-396.

29. Schmidt, H. and Hattel, J., A local model for the thermomechanical conditions in friction stir welding, *Model. Simul. Mater. Sci. Eng.* 13 (2005) 77-93.

30. Cho, J.H., Boyce, D.E., Dawson, P.R., Modeling strain hardening and texture evolution in friction stir welding of stainless steel, *Mat. Sci. Eng. A* 398 (2005) 146-163.

31. Bastier, A., Maitournam, M.H., Van, K.D., Roger, F., Steady state thermomechanical modelling of friction stir welding, *Sci. Technol. Weld. Joining* 11 (2006) 278-288.

32. He, Y., Boyce, D.E., Dawson, P.R., Three-dimensional modeling of void growth in friction stir welding of stainless steel, Proceed. 9th Internat. Conf. Numer. Meth. Indust. Form. Process., (Eds) J.M.A.C.d. Sa and A.D. Santos, 2007, 25-34.

33. De Vuyst, T. and D' Alvise, L., Material flow around a friction stir welding tool: development of a thermo-fluid code, *Weld. World* 51 (2007) 37-43.

34. Ulysse, P., Three-dimensional modeling of the friction stir-welding process, *Int. J. Mach. Tools Manuf.* 42 (2002) 1549-1557.

35. Langerman, M. and Kvalvik, E., Modeling plasticized aluminum flow and temperature fields during friction stir welding, 6th ASME-JSME Thermal Engin. Joint Conf., JSME, 2003.

36. Nandan, R., Roy, G.G., Lienert, T.J., Debroy, T., Three-dimensional heat and material flow during friction stir welding of mild steel, *Acta Mater.* 55 (2007) 883-895.

37. Askari, A., Silling, S., London, B., Mahoney, M., Modeling and analysis of friction stir welding processes, Friction Stir Welding and Processing, (Eds) K.V. Jata, M.W. Mahoney, R.S. Mishra, S.L. Semiatin, and D.P. Field, TMS, Warrendale, PA, 2001, 43-54.

38. Heurtier, P., Jones, M.J., Desrayaud, C., Driver, J.H., Montheillet, F., Allehaux, D., Mechanical and thermal modelling of friction stir welding, *J. Mater. Process. Technol.* 171 (2006) 348-357.

39. Murr, L.E., Trillo, E.A., Li, Y., Flores, R.D., Nowak, B.M., McClure, J.C., Solid-state flow associated with the friction-stir welding of dissimilar metals, in: N. El-Kaddah, et al. (Eds), Fluid flow phenomena in metals processing, TMS, Warrendale, PA, 1999, pp. 31-40.

40. Altan, T., Henning, H.J., Sabroff, A.M., The use of model materials in prediction forming loads in metalworking, *J. Eng. Ind. Trans. ASME* 92B (1970) 444-452.

41. Boer, C.R., Rebelo, N., Rydstad, H., Schroder, G., Process Modelling of Metal Forming and Thermomechanical Treatment. Springer-Verlag, New York, 1986.

42. Sofuoglu, H. and Rasty, J., Flow behavior of plasticine used in physical modeling of metal forming processes, *Tribol. Int.* 33 (2000) 523-529.

43. Schopfer, M.P.J. and Zulauf, G., Strain-dependent rheology and the memory of plastalina, *Tectonophysics* 354 (2002) 85-99.

44. Altan, T. and Boulger, F.W., Flow stress of metals and its application in metal forming analyses, *J. Eng. Ind. Trans.* 95 (1973) 1009-1019.

45. Adams, M.J., Aydin, I., Briscoe, B.J., Sinha, S.K., A finite element analysis of the squeeze flow of an elasto-viscoplastic paste material, *J. Non-Newtonian Fluid Mech.* 71 (1997) 41-57.

46. Chatraei, S., Macosko, C.W., Winter, H.H., Lubricated squeezing flow: a new biaxial extensional rheometer, *J. Rheol.* 25 (1981) 433-444.

47. Duan, X. and Sheppard, T., The influence of the constitutive equation on the simulation of a hot rolling process, *J. Mater. Process. Technol.* 150 (2004) 100-106.

48. Fereshteh-Saniee, F., Pillinger, I., Hartley, P., Friction modelling for the physical simulation of the bulk metal forming processes, *J. Mater. Process. Technol.* 153-154 (2004) 151-156.

49. Hawkyard, J.B. and Johnson, W., An analysis of the changes in geometry of a short hollow cylinder during axial compression, *Int. J. Mech. Sci.* 9 (1967) 163-182.

50. Incropera, F.P. and DeWitt, D.P., Fundamentals of Heat and Mass Transfer, 4th ed., Wiley, New York, 1996.

51. Huang, Z., Lucas, M., Adams, M.J., A numerical and experimental study of the indentation mechanics of plasticine, *J. Strain Analysis* 37 (2002) 141-150.

52. ASM Handbook, Metalworking: Bulk Forming, Constitutive equations, Ghosh, A. (Ed), S.L. Semiatin (Ed), Vol. 14A, ASM International, Materials Park, OH, 2005.

53. Mir Zahedul, H., Khandkar, H., Khan, J.A., Thermal modeling of overlap friction stir welding for Al-alloys, *J. Mater. Process. Manuf. Sci.* 10 (2001) 91-105.

54. ASM Handbook, Metalworking: Bulk Forming, Lubricants and their applications in forging, Shivpuri, R. and Kini, S. (Ed), S.L. Semiatin (Ed), Vol. 14A, ASM International, Materials Park, OH, 2005.

55. Metwalli, S.M., Ragab, A.R., Kamel, A.H., Abdul Saheb, A., Determination of plastic stress-strain behavior by digital-image-processing techniques, *Exper. Mech.* 27 (1987) 414-422.

56. Bochniak, W. and Korbel, A., Plastic flow of aluminium extruded under complex conditions, *Mat. Sci. Technol.* 16 (2000) 664-669.

57. Xu, S., Deng, X., Reynolds, A.P., Seidel, T.U., Finite element simulation of material flow in friction stir welding, *Sci. Technol. Weld. Joining* 6 (2001) 191-193.

58. Zettler, R., Lomolino, S., Santos, J.F., Donath, T., Beckmann, F., Lippman, T., Lohwasser, D., Effect of tool geometry and process parameters on material flow in FSW of an AA 2024-T351 alloy, *Weld. World* 49 (2005) 41-46.

59. Zhao, Y.H., Lin, S.B., Qu, F.X., Wu, L., Influence of pin geometry on material flow in friction stir welding process, *Mater. Sci. Technol.* 22 (2006) 45-50.

60. Schneider, J.A. and A.C. Nunes, J., Characterization of plastic flow and resulting microtextures in a friction stir weld, *Metall. Mater. Trans. B* 35 (2004) 777-783.

61. Arbegast, W., Modeling friction stir joining as a metalworking process, Proc. Hot Deformation of Al Alloys III, (Eds) Z. Jin, A. Beaudoin, T.A. Biesler, and B. Rakhakrishnan, San Diego, CA, 2003, 313-327.

62. McClure, J.C., Coronado, E., Aloor, S., Nowak, B.M., Murr, L.E., Nunes, A.C., Effect of pin tool shape on metal flow during friction stir welding, Proceedings of the 6th International Conference on Trends in Welding Research, (Eds) ASM International, Pine Mountain, GA, 2003, 257-261.

63. Nishihara, T. and Nagasaka, Y., Measurement of tool temperature during friction stir welding, 4th International Symposium on Friction Stir Welding, The Welding Institute, Park City, UT, 2003.

64. Wagoner, R.H. and Chenot, J.-L., Metal Forming Analysis. Cambridge University Press, New York, 2001.

65. Wagoner, R.H. and Chenot, J.-L., Fundamentals of Metal Forming. John Wiley & Sons, New York, 1997.

66. Maekawa, K., Kubo, A., Childs, T.H.C., A friction model for free-machining steels and its applicability to machinability analysis, *Key Engin. Mat.* 196 (2001) 79-90.

67. Timoshenko, S.P. and Goodier, J.N., Theory of Elasticity, 3rd ed., McGraw-Hill, New York, 1970.

68. Lienert, T.J., Stellwag, J., W.L., Grimmett, B.B., Warke, R.W., Friction Stir Welding Studies on Mild Steel, *Weld. J.* 82 (2003) 1s-9s.

69. FLUENT, Release 6.2.16, Fluent Incorporated, Lebanon, NH, 2004.

70. Liechty, B.C. and Webb, B.W., Flow field characterization of friction stir processing using a particle-grid method, *J. Mater. Process. Technol., doi:10.1016/j.jmatprotec.2008.01.008* (2008.

71. Buffa, G., Donati, L., Fratini, L., Tomesani, L., Solid stae bonding in extrusion and FSW: process mechanics and analogies, *J. Mater. Process. Technol.* 177 (2006) 344-347.

72. Buffa, G., Hua, J., Shivpuri, R., Fratini, L., Design of the friction stir welding tool using the continuum based FEM model, *Mat. Sci. Eng. A* 419 (2006) 381-388.

Appendix A: Cyan/Magenta Plasticine Color Analysis

All functions in this appendix were written using Visual Basic with Microsoft Excel's Macro Editor. Reference calibration and user input are provided in workbook sheets titled "Calib" and "Input," respectively.

RGB_Fraction

Function RGB_Fraction reads red, green, and blue values (RGB) for the parent cyan and magenta plasticine colors and RGB values for a single sample region. The initial calibration data is adjusted based on the parent cyan and magenta material values. Linear interpolation is then used to determine the fraction of magenta in the sample region.

```
Sub RGB_Fraction()

        n = 9
        ReDim x(n), rcal(n), gcal(n), bcal(n)
        ReDim rwld(n), gwld(n), bwld(n)

    'Read Calibration Clay Values
        Sheets("Calib").Select
        For i = 1 to n
        x(i) = Cells(i + 2, 2)        'known magenta fractions
        rcal(i) = Cells(i + 2, 3)     'red calibration values
        gcal(i) = Cells(i + 2, 4)     'green calibration values
        bcal(i) = Cells(i + 2, 5)     'blue calibration values
        Next

    'Read Measured Clay Values from weld
        Sheets("Input").Select
        r = 3  'beginning row
```

```
        'cyan clay
        rcy = Cells(r, 5)           'red level of parent cyan
        gcy = Cells(r + 1, 5)       'green level of parent cyan
        bcy = Cells(r + 2, 5)       'blue level of parent cyan
        'magenta clay
        rma = Cells(r + 3, 5)       'red level of parent magenta
        gma = Cells(r + 4, 5)       'green level of parent magenta
        bma = Cells(r + 5, 5)       'blue level of parent magenta
        'mixed region
        rmix = Cells(r + 6, 5)      'red level of mixed region
        gmix = Cells(r + 7, 5)      'green level of mixed region
        bmix = Cells(r + 8, 5)      'blue level of mixed region

    'Linear Shift Curve To Match Welded Clay Parent RGB levels
        dr0 = rcy - rcal(1)
        dg0 = gcy - gcal(1)
        db0 = bcy - bcal(1)
        dr1 = rma - rcal(n)
        dg1 = gma - gcal(n)
        db1 = bma - bcal(n)
        For i = 1 to n
          rshift = (dr1 - dr0) * x(i) + dr0
          gshift = (dg1 - dg0) * x(i) + dg0
          bshift = (db1 - db0) * x(i) + db0
          rwld(i) = rcal(i) + rshift
          gwld(i) = gcal(i) + gshift
          bwld(i) = bcal(i) + bshift
        Next

'Output Calibration Shift
        Sheets("Calib").Select
        For i = 1 to n
          Cells(i + 15, 2) = x(i)
          Cells(i + 15, 3) = rwld(i)
          Cells(i + 15, 4) = gwld(i)
          Cells(i + 15, 5) = bwld(i)
        Next

        Sheets(“Input”).Select

'Sample Region RGB Range Check
        If rmix < rwld(1) Or rmix > rwld(n) Then
          MsgBox ("Sample Region Red Out of Range!")
        End If
        If gmix > gwld(1) Or gmix < gwld(n) Then
          MsgBox ("Sample Region Green Out of Range!")
        End If
        If bmix > bwld(1) Or bmix < bwld(n) Then
          MsgBox ("Sample Region Blue Out of Range!")
        End If


'Linear Interpolation on Each Channel (RGB) and Print Value
          For i = 2 to n
            If rwld(i) > rmix Then  'red level interpolation
              xx1 = rwld(i - 1)
```

```
        yy1 = x(i - 1)
        xx2 = rwld(i)
        yy2 = x(i)
        Cells(16, 5) = (yy2 - yy1) * ((rmix - xx1) / (xx2 - xx1)) + yy1
        Goto 100
      End If
    Next
  100


  For i = 2 to n
     If gwld(i) < gmix Then  'greel level interpolation
        xx1 = gwld(i - 1)
        yy1 = x(i - 1)
        xx2 = gwld(i)
         yy2 = x(i)
        Cells(17, 5) = (yy2 - yy1) * ((gmix - xx1) / (xx2 - xx1)) + yy1
        Goto 200
     End If
    Next
  200

    For i = 2 to n
       If bwld(i) < bmix Then  'blue level interpolation
        xx1 = bwld(i - 1)
        yy1 = x(i - 1)
        xx2 = bwld(i)
        yy2 = x(i)
        Cells(18, 5) = (yy2 - yy1) * ((bmix - xx1) / (xx2 - xx1)) + yy1
        Goto 300
     End If
    Next
  300

End Sub
```

RGB_Surface

Function RGB_Surface reads red, green, and blue values (RGB) for an entire array of values output by ImageJ (*i.e.*, RGB matrix for entire image). Estimation of magenta and cyan fraction is then output. The process for determining the cyan/magenta fraction is identical to RGB_Fraction. The output file is formatted for ease of plotting with Igor.

```
Sub RGB_Surface()

        b = ActiveWorkbook.FullName
        Set fs = CreateObject("Scripting.FileSystemObject")
        b = fs.GetParentFolderName(b)

        ChDir b
        infile = b & "\" & Cells(22, 2)    'RGB file from ImageJ
        outfile = b & "\" & Cells(24, 2)  'Output for Igor

        oc = Cells(27, 2)
        tol = 0.5 'tolerance for RGB calibration agreement
        n = 10000 'estimated number of pixels (will adjust below)
        ReDim mlvl(9), rcal(9), gcal(9), bcal(9) 'calibration data
        ReDim cwld(3), mwld(3) 'cyan and magenta RGB values
        ReDim wavg(3) 'weighted averages
        ReDim lvl(n)  'calculated sample level

    'Read Calibration Data
        Sheets("Calib").Select
        For i = 1 to 9
        mlvl(i) = Cells(i + 2, 1)    'known magenta fractions
        rcal(i) = Cells(i + 2, 2)    'red calibration value
        gcal(i) = Cells(i + 2, 3)    'green calibration value
        bcal(i) = Cells(i + 2, 4)    'blue calibration value
        Next

    'Read User Input RGB Values for Parent Cyan and Magenta
        Sheets("Input").Select
        For i = 1 to 3
          cwld(i) = Cells(i + 2, 4)          'RGB parent cyan material values
          mwld(i) = Cells(i + 5, 4)          'RGB parent magenta material values
        Next

  'Read Weighted Averages
        For i = 1 to 3
          wavg(i) = Cells(i + 12, 3)         'calculated averages can be biased to a channel
        Next
```

```
'Linear Shift Calibration Curve to Match Welded Clay
        dr0 = cwld(1) - rcal(1)
        dg0 = cwld(2) - gcal(1)
        db0 = cwld(3) - bcal(1)
        dr1 = mwld(1) - rcal(9)
        dg1 = mwld(2) - gcal(9)
        db1 = mwld(3) - bcal(9)
        For i = 1 to 9
          rshift = (dr1 - dr0) * mlvl(i) + dr0
          gshift = (dg1 - dg0) * mlvl(i) + dg0
          bshift = (db1 - db0) * mlvl(i) + db0
          rcal(i) = rcal(i) + rshift
          gcal(i) = gcal(i) + gshift
          bcal(i) = bcal(i) + bshift
        Next

'Output Adjusted Calibration
        Sheets("Calib").Select
        For i = 1 to 9 'Adjusted curve
          Cells(i + 2, 6) = mlvl(i)
          Cells(i + 2, 7) = rcal(i)
          Cells(i + 2, 8) = gcal(i)
          Cells(i + 2, 9) = bcal(i)
        Next

'Read ImageJ Data and Convert to Cyan/Magenta Fraction

        Sheets("Input").Select
        Open infile For Input As #1
         i = 1
        flag = 0
        fltr = 0

        Do While Not EOF(1)    ' Loop until end of file.
           Input #1, x, y, r, g, b  'read pixel position (x,y) and RGB value
           If i = 1 Then yo = y
           If flag = 0 Then
            If y <> yo Then
             clmns = i – 1           'determine size of RGB array
             flag = 1
            End If
           End If

            ‘linear interpolation of pixel RGB
           Call interp(r, g, b, mlvl, rcal, gcal, bcal)  ‘returns magenta lvl for each channel

           'Redimension cyan/magenta fraction vector
           If i > n Then
             ReDim Preserve lvl(i)
           End If
```

```
        'Magenta Level Tolerance Check (level predicted on all channels must be within
        'tolerance, tol)
           drg = Abs(r - g)        'difference btwn magenta lvls on red & green channels
           drb = Abs(r - b)        'difference btwn magenta lvls on red & blue channels
           dgb = Abs(g - b)        'difference btwn magenta lvls on green & blue channels

           If drg > tol Or drb > tol Or dgb > tol Then 'tolerance exceeded for pixel
             lvl(i) = lvl(i - 1)  'filter pixel from output
             fltr = fltr + 1
             Goto 100
           End If

        'Compute Magenta Level Using Weighted Averages
           lvl(i) = wavg(1) * r + wavg(2) * g + wavg(3) * b
        'Limit Noise From Unfiltered 'Bad' Pixels (i.e., white regions around weld image)
           If lvl(i) > 1.5 Then lvl(i) = 1.5
           If lvl(i) < -0.5 Then lvl(i) = -0.5

        100

           i = i + 1         'increment pixel count

        Loop

        Close #1          'close ImageJ input file

        Cells(19, 4) = fltr          'print number of filtered pixels

'Write Igor Plot File
        k = 1
        n = i - 1
        ck = n / clmns
        rws = Int(n / clmns)

        If ck <> rws Then
          MsgBox ("Dimension Error!")
          Stop
        End If

        Cells(17, 4) = rws
        Cells(18, 4) = clmns

        Open outfile For Output As #2

        For i = 0 to clmns
          Print #2, i; ",";
        Next
          Print #2,
        For j = 1 to rws
          Print #2, j; ",";
          For i = k * clmns to (k - 1) * clmns + 1 Step -1
           If oc = 1 Then
              Print #2, 1 - lvl(i); ","; '1-lvl to print level of cyan
           Else
```

```
            Print #2, lvl(i); ","; 'lvl to print level of magenta
          End If
        Next
        k = k + 1
        Print #2,
      Next
      Close #2

End Sub


Sub interp(r, g, b, mlvl, rcal, gcal, bcal)
      'input RGB
      'input adjusted calibration curves (rcal, gcal, bcal)
      'output %magenta for each r,g,b channels (overwrite r,g,b with % magenta value)

    'linear interpolation
      flag = 0

       If r <= rcal(1) Then
        r = 0
        flag = 1
       End If

       If r >= rcal(9) Then
        r = 1
        flag = 1
       End If

      If flag = 0 Then
         For i = 2 to 9
            If rcal(i) > r Then
               xx1 = rcal(i - 1)
               yy1 = mlvl(i - 1)
               xx2 = rcal(i)
               yy2 = mlvl(i)
               r = (yy2 - yy1) * ((r - xx1) / (xx2 - xx1)) + yy1
              Goto 100
            End If
         Next
      End If
      100

      flag = 0

       If g >= gcal(1) Then
          g = 0
          flag = 1
       End If

       If g <= gcal(9) Then
         g = 1
         flag = 1
       End If

      If flag = 0 Then
```

```
   For i = 2 to 9
    If gcal(i) < g Then
       xx1 = gcal(i - 1)
       yy1 = mlvl(i - 1)
       xx2 = gcal(i)
       yy2 = mlvl(i)
      g = (yy2 - yy1) * ((g - xx1) / (xx2 - xx1)) + yy1
      Goto 200
    End If
   Next
 End If
200

flag = 0

If b >= bcal(1) Then
   b = 0
   flag = 1
End If

If b <= bcal(9) Then
   b = 1
   flag = 1
End If

If flag = 0 Then
   For i = 2 to 9
    If bcal(i) < b Then
       xx1 = bcal(i - 1)
       yy1 = mlvl(i - 1)
       xx2 = bcal(i)
       yy2 = mlvl(i)
       b = (yy2 - yy1) * ((b - xx1) / (xx2 - xx1)) + yy1
       Goto 300
      End If
   Next
End If
300

End Sub
```

Table A-1: Cyan/Magenta RGB Fraction Error Analysis.

Magenta Fraction	Weights			Magenta Block	Cyan Block	Prediction	Error
	Mag. [oz]	Cyan [oz]	Total [oz]				
0.11	0.5	4.0	4.5	1	2	0.12	-1%
0.22	1.0	3.5	4.5	2	2	0.21	2%
0.25	1.0	3.0	4	2	2	0.24	1%
0.29	1.0	2.5	3.5	1	1	0.26	2%
0.33	1.0	2.0	3	2	2	0.34	0%
0.50	1.0	1.0	2	1	1	0.50	0%
0.57	2.0	1.5	3.5	2	1	0.59	-2%
0.67	2.0	1.0	3	2	1	0.61	5%
0.80	2.0	0.5	2.5	2	1	0.73	7%
0.86	3.0	0.5	3.5	1	2	0.86	0%

Table A-2: Cyan/Magenta RGB Calibration Values.

Magenta	Red	Green	Blue
0	4.59	106.3	183.2
0.10	9.53	90.1	175.1
0.25	18.0	64.2	154.8
0.40	25.9	54.5	144.6
0.50	28.3	50.1	139.7
0.60	33.5	38.1	125.7
0.75	45.62	32.6	115.1
0.90	62.1	29.1	100.5
1.0	126.3	21.1	93.0

Appendix B: Physical Properties Uncertainty Analysis

Flow Stress

The true stress is determined as $\sigma = F/A = hF/V$, where F, A, and h are the instantaneous force, area, and height, respectively, and $V = h_o \pi r_o^2$ is volume (constant) of the compression sample. Uncertainty in the true stress is determined by partial differentiation according to Eq. (B-1),

$$U_\sigma^2 = \left(U_h \frac{\partial \sigma}{\partial h} \right)^2 + \left(U_F \frac{\partial \sigma}{\partial F} \right)^2 + \left(U_{h_o} \frac{\partial \sigma}{\partial h_o} \right)^2 + \left(U_{r_o} \frac{\partial \sigma}{\partial r_o} \right)^2 . \quad \text{(B-1)}$$

In Eq. (B-1), U_h and U_F are the uncertainties in the instantaneous sample height and measured force during compression and U_{h_o} and U_{r_o} are uncertainties in the initial sample dimensions. Carrying out the differentiation gives,

$$\left(\frac{U_\sigma}{\sigma} \right)^2 = \left(\frac{U_h}{h} \right)^2 + \left(\frac{U_F}{F} \right)^2 + \left(\frac{U_{h_o}}{h_o} \right)^2 + \left(\frac{2U_{r_o}}{r_o} \right)^2 . \quad \text{(B-2)}$$

The initial height of the plasticine samples used for the compression tests was 5.1 ± 0.2 cm. Since the position of the compression ram was input according to Eq. (3-5), the uncertainty in the instantaneous sample height is approximately constant throughout the test and equal to U_{h_o} (*i.e.*, negligible error in ram position). By pressing the clay samples from a steel cylinder, the initial radius of the samples can be controlled to within 3.0 ± 0.05 cm. Including system noise, the uncertainty of the load cell is $U_F \approx \pm 5$ N.

Substituting these values for the uncertainties in Eq. (B-2), the uncertainty in flow stress can be determined at any value of stress and strain using Eq. (3-5) and the definition of true stress given above. Figure B-1 shows the uncertainty in flow stress values as a function of flow stress and true strain. The error is less than 15% at stress levels above approximately 50 kPa and true strains less than unity.

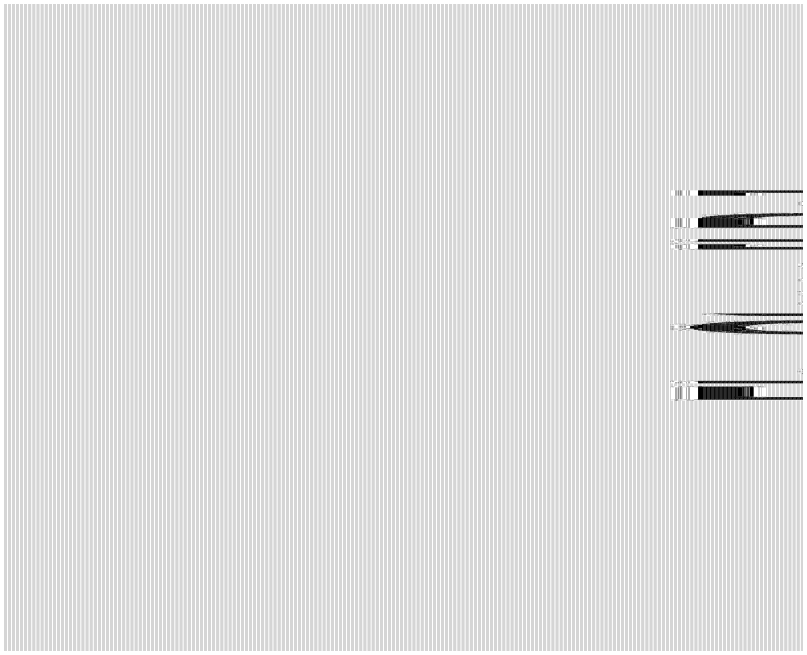

Figure B-1: Percent error in flow stress values as a function of true strain and true stress.

Shear Friction Factor

Error in the ring compression tests is introduced primarily from measurement of the inner diameter during compression. Therefore, uncertainty in the shear friction coefficient is approximated as the error in the inner diameter measurement. This error is only one or two percent.

Thermal Conductivity

The thermal conductivity of the plasticine is determined according to Eq. (3-9). The most significant source of uncertainty in the thermal conductivity is the measured temperature difference ($T_1 - T_2$) across the plasticine slab. Error in the temperature difference measurement can be minimized by accounting for the temperature difference between the two thermocouples at room temperature. After adjusting for the error in individual thermocouple measurements, the largest source of uncertainty is system noise, which is estimated at 5 to 10%. All other measured variables in Eq. (3-9) produce only approximately 2% uncertainty in k. Error in the thermal conductivity measurement is therefore approximately equivalent to the temperature difference measurement error (*i.e.*, $U_k \lesssim 10\%$).

Specific Heat Capacity

The specific heat capacity is calculated from the definition of the Fourier number ($Fo = kt/\rho c_p r^2$). Uncertainties in the density of the plasticine and time measurement are negligible compared to the other variables. Therefore, the error in the specific heat is

$$\left(\frac{U_{c_p}}{c_p}\right)^2 = \left(\frac{U_k}{k}\right)^2 + \left(2\frac{U_r}{r}\right)^2 + \left(\frac{U_{Fo}}{Fo}\right)^2 . \qquad \text{(B-3)}$$

It is difficult to maintain the shape of the heated plasticine sphere exactly because a slight force can deform the sphere. Additionally, there is some uncertainty in placing the thermocouple at the exact center of the sphere. These two uncertainties are lumped into an uncertainty in the sphere radius (U_r), which therefore can approach ±1 mm ($2U_r/r$ =

15%). The error in Fo (U_{Fo}) is determined numerically by introducing a small perturbation to the dimensionless temperature difference (θ_o) in Eq. (3-10) and calculating the resulting Fo. The size of the perturbation in θ_o is $U_{\theta_o} = U_T/(T_i - T_\infty) = 0.01$. Using this perturbation, between the range of $0.1 < \theta_o < 0.9$, the uncertainty in Fo is $U_{Fo}/Fo < 3\%$. The error in Fo outside this range rises rapidly to extreme values (error > 40%) at $\theta_o = 0$ and 1. Note that this higher error in Fo can be completely avoided by adjusting T_i and T_∞ to values slightly beyond the desired upper and lower limit temperature values. Substituting the appropriate values into Eq. (B-3) gives $U_{c_p}/c_p \approx 18\%$ over the range of desired temperatures.

Appendix C: X-Ray Particle Image Uncertainty Analysis

Velocity Uncertainty

The average local velocity is determined from the distance between two particles along a streamline before and after processing according to Eq. (C-1),

$$V = \frac{\Delta s}{\Delta t} = \frac{f \Delta s}{\Delta s_o}, \tag{C-1}$$

where $\Delta t = \Delta s_o / f$, f is the feed-rate, and Δs_o and Δs are the initial and final spacing of two particles, respectively.

Neglecting any error in the tool feed rate, the uncertainty in the velocity, U_V, is estimated as

$$U_V^2 \approx \left(\frac{\partial V}{\partial \Delta s_o} U_{\Delta s_o} \right)^2 + \left(\frac{\partial V}{\partial \Delta s} U_{\Delta s} \right)^2 . \tag{C-2}$$

Uncertainty in the initial particle spacing, $U_{\Delta s_o}$, consists of error in locating the intersections of grid lines or steel particle centers, U_x. It can be shown that the uncertainty in the straight-line distance between any two points is $U_{\Delta s_o} = \sqrt{2} U_x$. The particle centers can be determined accurately by enlarging sections of the digital images. A conservative estimate for U_x is ±0.1 mm. As particles move around the pin, the path of the particle is approximated as $r_m \theta$, where r_m is the mean distance (measured from the pin center) of two particles and θ is the angle between the particles. It is assumed that the

error in the arc approximation pathline is negligible. This assumption is valid as long as the distance from the pin center of both particles is nearly equal. In other words, if both particles are in contact with the pin, then the assumed pathline is correct. Assuming that the uncertainty in the particle spacing before ($U_{\Delta s}$) and after FSW ($U_{\Delta s_o}$) are equal, the error in the velocity becomes,

$$\frac{U_V}{V} = U_{\Delta s_o}\left[\left(\frac{f\Delta s}{\Delta s_o^2}\right)^2 + \left(\frac{f}{\Delta s_o}\right)^2\right]^{1/2}\left[\frac{\Delta s_o}{f\Delta s}\right]. \tag{C-3}$$

Strain/Strain-Rate Uncertainty

Strain and strain-rates are estimated based on stretching of the streamline around the pin. The effective strain is

$$\varepsilon = \frac{\Delta s - \Delta s_o}{\Delta s_o}. \tag{C-4}$$

Note that the effective streamwise strain is only a function of the before and after FSW spacing of two particles. The effective strain-rate, however, also depends on the spacing of a neighboring particle pair immediately upstream according to Eq. (C-5),

$$\dot{\varepsilon} = \frac{1}{\Delta t}\frac{\Delta s - \Delta s_u}{\Delta s_u} = \frac{f\left(\Delta s - \Delta s_u\right)}{\Delta s_o \Delta s_u}, \tag{C-5}$$

where Δs_u refers to the upstream particle spacing.

Uncertainty in the streamwise strain value is determined by differentiation of Eq. (C-4). Carrying out the differentiation yields

$$\frac{U_\varepsilon}{\varepsilon} = U_{\Delta s_o}\left[\left(\frac{\Delta s}{\Delta s_o^2}\right)^2 + \left(\frac{1}{\Delta s_o}\right)^2\right]^{1/2}\left[\frac{\Delta s_o}{\Delta s - \Delta s_o}\right]. \tag{C-6}$$

Similarly, the strain-rate error (with the approximation $U_{\Delta s} \approx U_{\Delta s_u} \approx U_{\Delta s_o}$) is

$$\frac{U_{\dot{\varepsilon}}}{\dot{\varepsilon}} = U_{\Delta s_o}\left[\left(\frac{f}{\Delta s_u^2 \Delta s_o}\right)^2 + \left(\frac{f\left(\Delta s_u - \Delta s\right)}{\Delta s_u \Delta s_o^2}\right)^2 + \left(\frac{f\left(\Delta s_u - \Delta s\right)}{\Delta s_u^2 \Delta s_o^2}\right)^2\right]^{1/2}\left[\frac{\Delta s_u \Delta s_o}{f\left(\Delta s_u - \Delta s\right)}\right]. \quad \text{(C-7)}$$

Appendix D: Fluent User Defined Functions

```
#include "udf.h"
#define RPMTORADPS 0.104719755
#define DEGTORAD 0.01745329252
#define ZERO 0.0001

void WriteParameters()
{
/* ----------------------------------------------------------------------------
This function writes all stored parameters as defined in the file
“UserParameters.txt” to the Fluent console.
----------------------------------------------------------------------------*/

  Message("\n");
  Message("frict/mode = %d\n", RP_Get_Integer("frict/mode"));
  Message("frict/coeff = %f\n", RP_Get_Real("frict/coeff"));
  Message("frict/sens = %f\n", RP_Get_Real("frict/sens"));
  Message("frict/mu = %f\n", RP_Get_Real("frict/mu"));
  Message("frict/value = %f\n", RP_Get_Real("frict/value"));
  Message("frict/heateff = %f\n", RP_Get_Real("frict/heateff"));
  Message("tool/rpm = %f\n", RP_Get_Real("tool/rpm"));
  Message("tool/tiltdeg = %f\n", RP_Get_Real("tool/tiltdeg"));
  Message("tauwrite = %d\n", RP_Get_Integer("tauwrite"));
  Message("tau/relax = %f\n", RP_Get_Real("tau/relax"));
  Message("visc/relax = %f\n", RP_Get_Real("visc/relax"));
  Message("fstress/ko = %f\n", RP_Get_Real("fstress/ko"));
  Message("fstress/m = %f\n", RP_Get_Real("fstress/m"));
  Message("fstress/beta = %f\n", RP_Get_Real("fstress/beta"));
  Message("\n");

}
```

```
double EffStrainRate(cell_t c, Thread *t)
{
/* ----------------------------------------------------------------------------
Calculate the associated Von-Mises effective strain-rate
    Input – cell, thread
    Output – effective strain-rate
----------------------------------------------------------------------------*/

  real dd[9],ee[3][3];
  real stnrt;
  int i,j;
  real ef;

    dd[0]=C_DUDX(c,t);
    dd[1]=C_DUDY(c,t);
    dd[2]=C_DUDZ(c,t);

    dd[3]=C_DVDX(c,t);
    dd[4]=C_DVDY(c,t);
    dd[5]=C_DVDZ(c,t);

    dd[6]=C_DWDX(c,t);
    dd[7]=C_DWDY(c,t);
    dd[8]=C_DWDZ(c,t);

    ee[0][0]=dd[0];
    ee[0][1]=0.5*(dd[1]+dd[3]);
    ee[0][2]=0.5*(dd[2]+dd[6]);
    ee[1][0]=0.5*(dd[3]+dd[1]);
    ee[1][1]=dd[4];
    ee[1][2]=0.5*(dd[5]+dd[7]);
    ee[2][0]=0.5*(dd[6]+dd[2]);
    ee[2][1]=0.5*(dd[7]+dd[5]);
    ee[2][2]=dd[8];

    ef=0;
    for (i=0;i<3;i++){
       for (j=0;j<3;j++){
           ef=ef+(ee[i][j]*ee[i][j]);
     }
    }

    ef=sqrt(2.*ef/3.);
    C_UDMI(c,t,1)=ef;   /* store effective strain-rate */
    return ef;
 }
```

```
void FlowDir(face_t f, Thread *t,real *Dxp,real *Dzp, real *rr)
{
/* ----------------------------------------------------------------------------
Determine the direction of the shear stress or velocity vector
    Input – tool cell face, face thread
    Return
        Dxp – x component of direction vector expressed in tool-tilted system
        Dzp – z component of direction vector expressed in tool-tilted system (y is vertical)

        rr – radial distance of local tool point from axis of tool rotation
----------------------------------------------------------------------------*/
  real x[3],xp,tt,Dmag,dt=.01,dx,dz,r,theta;

        theta = RP_Get_Real("tool/tiltdeg")*DEGTORAD; /* tilt is about z – axis */
        F_CENTROID(x,f,t); /*get cell face centroid (y or x[1] – is vertical) */
        xp = x[0]*cos(theta)+x[1]*sin(theta); /* transform x coord to tilted axis */
        r = sqrt(xp*xp+x[2]*x[2]);
        tt = atan2(x[2],xp);
        dx = r*cos(tt+dt)-xp;
        dz = r*sin(tt+dt)-x[2];
        Dmag = sqrt(dx*dx+dz*dz);
        *Dxp = dx/Dmag;
        *Dzp = dz/Dmag;
        *rr=r;
}
```

```
double WallShear(face_t f, Thread *t)
{
/* ----------------------------------------------------------------------------
Calculate the magnitude of the local tool shear stress
    Input – tool cell face, face thread
    Output – wall shear stress
----------------------------------------------------------------------------*/
            real A[3],wallshear[3],area;
            real stnrt,tau,kf,mu,eta,effsig,signml,beta,n;
            real omega,v,xp,r,theta,val;
            real pressoffset;
            real m,alpha,tau_old;
            real x[3];
            real press,sigma[6];
            real a[3],amag;
            cell_t c;
            Thread *c_thread;
            int i,shearmode;

             c_thread = THREAD_T0(t); /* cell thread adjacent to boundary */
             c = F_C0(f,t);  /* get cell number */
             stnrt = EffStrainRate(c,c_thread)+ZERO;
             eta = C_MU_L(c,c_thread); /* cell viscosity */
             kf = (3.*stnrt*eta)/sqrt(3.); /* shear flow stress of material in cell */

      shearmode = RP_Get_Integer("frict/mode");

     if (shearmode==0){
      /* set constant velocity, calculate shear stress for frictheat function */
       tau = RP_Get_Real("frict/value");
       if (tau==0){
            NV_V(wallshear,=,C_STORAGE_R_NV(f,t,SV_WALL_SHEAR));
             F_AREA(A,f,t);
             area=NV_MAG(A);
             tau=fabs(NV_MAG(wallshear)/area);
            }
      }

     if (shearmode==1){
      /* set constant shear stress */
            tau = RP_Get_Real("frict/value");
     }

      if (shearmode==2){
         /* Tresca friction model*/
            m=RP_Get_Real("frict/coeff");
            tau=m*kf;
     }



if (shearmode==3){
       /* viscoplastic friction model*/
            m=RP_Get_Real("frict/coeff");
            n=RP_Get_Real("frict/sens");
            omega = RP_Get_Real("tool/rpm")*RPMTORADPS;
```

```
            theta = RP_Get_Real("tool/tiltdeg")*DEGTORAD;
            v = sqrt(F_U(f,t)*F_U(f,t)+F_V(f,t)*F_V(f,t)+F_W(f,t)*F_W(f,t));
            F_CENTROID(x,f,t);
            xp = x[0]*cos(theta)+x[1]*sin(theta);
            r = sqrt(xp*xp+x[2]*x[2]);
            tau = m*kf*sqrt(3.)*pow((r*omega-v),n);
}

if (shearmode==4){
 /* variable shear stress model*/
            beta = RP_Get_Real("frict/coeff");
            n = RP_Get_Real("frict/sens");
            mu = RP_Get_Real("frict/mu");
            signml=RP_Get_Real("frict/value");

            if (signml==0.){
              signml=-1.*F_P(f,t); /* negative pressure is tension */
              if (signml>0.){ /* if stress >0 then tension */
                 signml = 0.;}
            }

            val=-1.*pow(mu*fabs(signml)/(fabs(beta)*kf),n);
            tau = beta*kf*pow(1.-exp(val),(1./n));
}

/* Shear Stress Relaxation */
    alpha = RP_Get_Real("tau/relax");
    tau_old=F_UDMI(f,t,0);
    tau=alpha*tau+(1.-alpha)*tau_old;

    F_UDMI(f,t,0)=tau;

return tau;

}
```

```
DEFINE_PROFILE(frictheat,t,i)
{
/* ----------------------------------------------------------------------------
Set the local heat flux at the tool due to friction
(Refer to Fluent UDF Manual for details on input arguments for Profile functions)
----------------------------------------------------------------------------*/
real omega,alpha,theta,xp,r,v,tau;
real x[3];
face_t f;

Message("Setting UDF Heat Flux.\n");

omega = RP_Get_Real("tool/rpm")*RPMTORADPS;
theta = RP_Get_Real("tool/tiltdeg")*DEGTORAD;
alpha = RP_Get_Real("frict/heateff");

  begin_f_loop(f,t)
  {
          tau=WallShear(f,t);
          v = sqrt(F_U(f,t)*F_U(f,t)+F_V(f,t)*F_V(f,t)+F_W(f,t)*F_W(f,t));
          F_CENTROID(x,f,t);
          xp = x[0]*cos(theta)+x[1]*sin(theta);
          r = sqrt(xp*xp+x[2]*x[2]);
          F_PROFILE(f,t,i) = alpha*fabs(tau)*(r*omega-v);
  }
  end_f_loop(f,t)

}
```

```
/* ---------------------------------------------------------------------------
The 3 functions below set the shear (or velocity) components for
the feed, transverse, and vertical directions.
---------------------------------------------------------------------------*/

DEFINE_PROFILE(FeedDir,t,i)
{
  face_t f;
  real Dxp,Dzp,rr,tau,theta;
  int mode;
  Message("Calling Profiles xvel ");

  theta = RP_Get_Real("tool/tiltdeg")*DEGTORAD;
  mode = RP_Get_Integer("frict/mode");

  begin_f_loop(f,t)
  {
          tau=WallShear(f,t);
          FlowDir(f,t,&Dxp,&Dzp,&rr);
          if (mode!=0){
            rr=1.0;}
          F_PROFILE(f,t,i) = rr*tau*Dxp*cos(theta);
  }
  end_f_loop(f,t)
}

DEFINE_PROFILE(VertDir,t,i)
{
face_t f;
real Dxp,Dzp,rr,tau,theta;
int mode;
Message("yvel ");

theta = RP_Get_Real("tool/tiltdeg")*DEGTORAD;
mode = RP_Get_Integer("frict/mode");

 begin_f_loop(f,t)
 {
          tau=WallShear(f,t);
          FlowDir(f,t,&Dxp,&Dzp,&rr);
          if (mode!=0){
            rr=1.0;}
          F_PROFILE(f,t,i) = rr*tau*Dxp*sin(theta);
  }
   end_f_loop(f,t)
}
DEFINE_PROFILE(TransDir,t,i)
{
face_t f;
real Dxp,Dzp,rr,tau,theta;
int ii, mode;

theta = RP_Get_Real("tool/tiltdeg")*DEGTORAD;
mode = RP_Get_Integer("frict/mode");

Message("zvel\n");
```

```
  if (mode==0){
          Message("Using Constant Velocity B.C.\n");}
  if (mode==1){
          tau = RP_Get_Real("frict/value");
          Message("Wall Shear Set to %f\n",tau);}
  if (mode==2){
          Message("Using Tresca Friction\n");}
  if (mode==3){
          Message("Using Viscoplastic Friction\n");}
  if (mode==4){
          Message("Using Variable Shear Stress\n");}

  ii=RP_Get_Integer("tauwrite");

  begin_f_loop(f,t)
  {
       tau=WallShear(f,t);
          if (ii==1){
            Message("tau = %f\n",-1.*tau);}
          FlowDir(f,t,&Dxp,&Dzp,&rr);
          if (mode!=0){
            rr=1.0;}
          F_PROFILE(f,t,i) = rr*tau*Dzp;

  }
   end_f_loop(f,t)
}
```

```
DEFINE_PROPERTY(flow_stress_vis,c,t)
{
/* ----------------------------------------------------------------------------
Calculate the local effective viscosity
(Refer to Fluent UDF Manual for details on input arguments for Property functions)
----------------------------------------------------------------------------*/
real eta,sig;
real temp=C_T(c,t);
real stnrt;
real ko,m,beta;
real alpha= RP_Get_Real("visc/relax");
real etaold=C_MU_L(c,t);

stnrt=EffStrainRate(c,t)+ZERO;

ko=RP_Get_Real("fstress/ko");
m=RP_Get_Real("fstress/m");
beta=RP_Get_Real("fstress/beta");

sig=ko*exp(-1.*beta*temp)*pow(stnrt,m);
eta=sig/(3.*stnrt); /* units are Pa s  */

C_UDMI(c,t,0) = sig;  /*store local viscosity */

eta = alpha*eta+(1-alpha)*etaold;

if (eta<100.0){
    Message("Low Limit Viscosity Reached\n");
    eta=100.0;
}

return eta;
}


DEFINE_ON_DEMAND(DisplayUserParameters)
{
/* ----------------------------------------------------------------------------
Write user defined parameters to Fluent consol
----------------------------------------------------------------------------*/
WriteParameters();
}
```

```
DEFINE_ON_DEMAND(ReadUserParameters)
{
/* ----------------------------------------------------------------------------
Read and set parameters as defined in “UserParameters.txt”
----------------------------------------------------------------------------*/
  real a;
  int i;
  FILE *fp;
  fp=fopen("UserParameters.txt","r");

  Message("\nReading UserParameters File ... \n");

  fscanf(fp, "%d", &i);
    RP_Set_Integer("frict/mode",i);
  fscanf(fp, "%f", &a);
    RP_Set_Real("frict/coeff",a);
  fscanf(fp, "%f", &a);
    RP_Set_Real("frict/sens",a);
  fscanf(fp, "%f", &a);
    RP_Set_Real("frict/mu",a);
  fscanf(fp, "%f", &a);
    RP_Set_Real("frict/value",a);
  fscanf(fp, "%f", &a);
    RP_Set_Real("frict/heateff",a);
  fscanf(fp, "%f", &a);
    RP_Set_Real("tool/rpm",a);
  fscanf(fp, "%f", &a);
    RP_Set_Real("tool/tiltdeg",a);
  fscanf(fp, "%d", &i);
    RP_Set_Integer("tauwrite",i);
  fscanf(fp, "%f", &a);
    RP_Set_Real("tau/relax",a);
  fscanf(fp, "%f", &a);
    RP_Set_Real("visc/relax",a);
  fscanf(fp, "%f", &a);
    RP_Set_Real("fstress/ko",a);
  fscanf(fp, "%f", &a);
    RP_Set_Real("fstress/m",a);
  fscanf(fp, "%f", &a);
    RP_Set_Real("fstress/beta",a);

  WriteParameters();

  fclose(fp);

}
```

Appendix E: Fluent FSW User Defined Function Manual

To use the FSW user defined functions with Fluent, the working folder must contain the following three files:

Parameters.scm
UserParameters.txt
ShearBoundary.c

Details and contents for each file are explained in the sections below.

Parameters.scm

This file contains all user input variables, which must be initialized in Fluent before the UDF's can be executed. The file can be loaded into Fluent by selecting File – Read – Scheme. The file contains the following initialization code:

```
(rp-var-define 'frict/mode 1 'integer #f)
(rp-var-define 'frict/coeff 1 'real #f)
(rp-var-define 'frict/sens 1 'real #f)
(rp-var-define 'frict/mu 1 'real #f)
(rp-var-define 'frict/value 1 'real #f)
(rp-var-define 'frict/heateff 1 'real #f)
(rp-var-define 'tool/rpm 1 'real #f)
(rp-var-define 'tool/tiltdeg 1 'real #f)
(rp-var-define 'tauwrite 1 'integer #f)
(rp-var-define 'tau/relax 1 'real #f)
(rp-var-define 'visc/relax 1 'real #f)
(rp-var-define 'fstress/ko 1 'real #f)
(rp-var-define 'fstress/m 1 'real #f)
(rp-var-define 'fstress/beta 1 'real #f)
```

UserParameters.txt

UserParameters.txt provides a text user interface to define several model variables as noted below in the sample file below.

Example UserParameters.txt file:

```
2
-0.95
5.0
0.57
0
0.2
250
2.5
0
1.0
1.0
1.82e14
0.175
0.0701
```

An associated description for each line above is:

shear stress mode (0-velocity, 1-constant, 2-Tresca, 3-viscoplastic, 4-variable)
shear friction factor (m,alpha,or R) (- cw tool rotation, + ccw tool rotation)
friction sensitivity for variable shear and viscoplastic models only (n)
friction coefficient for variable shear model only (mu)
constant friction value, normal stress (if 0 then calculated), or velocity
friction heating efficiency for all models (gamma)
tool rpm
tool tilt in degrees (must be consistent with imported geometry)
write shear stress values (0 - no, 1 - yes)
shear stress relaxation (range 0 to 1)
effective viscosity relaxation (range 0 to 1)
flow stress model constant strength (ko)
flow stress model strain-rate sensitivity (m)
flow stress model temperature sensitivity (beta)

ShearBoundary.c

Complete source code is listed in Appendix E. The code must be compiled using Fluent's UDF complier (Define – User Defined – Functions – Compiled). Additionally, the source code requires two reserved memory locations (Define – User Defined – Memory). Each of the UDF boundary conditions and effective viscosity models must be linked to Fluent in the normal method (see Fluent UDF Manual). Additionally, the functions "ReadUserParameters" and "DisplayUserParameters" can be executed "on demand" by the user (Define – User Define – Execute On Demand). Recall that "ReadUserParameters" reads the "UserParameters.txt" file and sets values in Fluent, while "DisplayUserParameters" simply displays the currently loaded values. Note that "Parameters.scm" must be loaded before these functions can execute.

Boundary Conditions

The Boundary Conditions interface in Fluent allows a user to set both velocity and shear stress conditions simultaneously. However, it appears that during computation, any velocity condition is overwritten by shear conditions. Therefore, if shear components are specified in Fluent then any specified velocity components are ignored. A constant velocity boundary condition at the tool can be specified with either Fluent's built in features for a rotating wall or through the UDF. Regardless, the shear mode in "UserParameters.txt" must be set to zero and the correct rotation rate should be specified in the user file. This is because these values are also used for the frictional heat flux boundary condition.

Initialization and Convergence

Convergence with the plasticine can be very difficult depending on initialization and relaxation factors. Generally, best convergence with plasticine occurs if the model is first run with an alternate medium such as water for 10 – 20 iterations to initialize the flow around the tool. A non-rotating tool is initially used for this alternate medium and the heat flux was set to an arbitrarily constant value of 20 W/m^2K. This solution is then used as the initial guess for the non-Newtonian flow, where the material in contact with the tool is given a constant velocity (depending on it distance from the axis of rotation) and the UDF heat flux is imposed. Typically, relaxation factors that result in good convergence are 0.1, 0.4, and 0.6 for continuity, momentum, and energy, respectively. For plasticine, it was found that relaxation factors for the effective viscosity and tool shear stress (defined in "UserParametes.txt") can be set at 1.0. The pressure-velocity coupling used was SIMPLE, and a second-order upwind scheme was used for momentum and energy (a second order scheme was also used for pressure). Approximately 500 iterations must then be executed to achieve a converged solution, where temperature and velocity values cease to change significantly between iterations. Note, however, that these values may vary with mesh size and workpiece material. Once the constant rotational velocity model is converged, various tool shear stress boundary conditions were imposed and run 500 – 1000 iterations to convergence.

Generally, iterations can be restarted in Fluent from the last saved iteration. However, cases using the imposed wall shear stress conditions generally show a sudden jump and subsequent rapid convergence back to the initial residual values when a case is closed and Fluent is restarted. The cause for this is unclear, but may be due to some part

of the solution not being saved in the case and data files. Regardless of the cause, the sudden jump in residuals does not appear to alter solution values.